Probing the mechanics of cellulose and nucleus associated machinery using optical tweezers

By

Sonia Karoline Brady

Dissertation

Submitted to the Faculty of the

Graduate School of Vanderbilt University

in partial fulfillment of the requirements

for the degree of

DOCTOR OF PHILOSOPHY

in

Chemical Engineering

May, 2017

Nashville, Tennessee

Approved:

Matthew J. Lang, Ph.D.

Clare McCabe, Ph.D.

John T. Wilson, Ph.D.

Ryoma Ohi, Ph.D.

To my parents for their unwavering support and encouragement.

ACKNOWLEDGMENTS

They say it takes a village to raise a child and I don't think getting a Ph.D. is much different. While this document represents the culmination of my academic experience, graduate school has been so much more than the hours I've spent in the lab. It has been a new chapter of my life and has encompassed classes, TA'ing, a move to a new city, friendships with people who have become like family, the creation of a community I am humbled and blessed to be a part of, the fostering of a passion for teaching, and growth academically, personally, and spiritually. There have been good times, hard times, stressful and fun times, set backs and breakthroughs and I've gotten through all of it with "a little help from my friends." There are so many people to recognize and thank for making the last 5 1/2 years all that they have been. My life is richer because of all of them.

First, I need to recognize my advisor, Matt Lang, for being the best PI I could have ever hoped to work with. Thank you for your expertise, guidance, mentorship, infinite patience, and constant encouragement. You are the reason I am the scientist I am today. You have been an example of what it means to have integrity, work hard, and to put people (and family) first. You have been a constant source of support in the research world but also of my passion for teaching. Without your support, I wouldn't have been able to be as involved as I have been and my future would certainly look a little different. Thank you for your example and everything you have done for me.

To my labmates past and present - thank you for brainstorming with me, sharing ideas and expertise, birthday cakes, lab lunches, encouragement, laughter, and support. You have been more than labmates, you have been my friends. Thank you for adding so much joy to the days in lab. Yongdae, thank you for your wisdom and expertise as the senior lab member. JC, thank you for being the best desk buddy, labmate, and friend I could have asked for. Nikki, thank you for the friendship and for being another female presence in the lab. Harris, thank you for your quiet and calm nature even/especially in the times when I

was not. Andy, thank you for the example of hard work, problem solving, and perseverance. And Dev, thank you for your scientific passion and for keeping me on my toes.

To the undergraduates I've have the opportunity to work with (Kelsea Best, Andrew Vancura, Gilda Naka, Catey Dodson, and Allie Smith) - thank you for your energy, help, and willingness to learn, especially when science didn't work as we would have liked.

To the rest of my committee, Professors Clare McCabe, John Wilson, and Ryoma (Puck) Ohi - thank you for your guidance and support over the last several years. Thank you also to all of my collaborators and the other scientific minds along the way who have made the work I have done possible: Shishir Chundawat, Jochen Zimmer, Sreelatha Sarangapani, Marija Zanic, and Daniel Balikov.

To the ChBE staff - I would be remiss if I did not acknowledge and thank all of you who have put in countless orders for me, made sure I got paid, responded to and fixed things around the lab, offered encouragement, and have brightened every day of my time at Vanderbilt with your smiles and love of life. Mary Gilleran, Rae Uson, Julie James, Angie Pernell, and Mark Holmes: THANK YOU! You are so appreciated.

To the ChBE girls: Lara, Ali, Holly, Nikki, Anne, and May - Graduate school would not have been the same without you. You have been some of my best friends. You have seen me at my best and at my worst, encouraged me, and kept me sane. Thank you for the laughs, girls nights, venting sessions, coffee talks, celebrations of big life events, and everything in between.

To the rest of the office and all my other ChBE friends who have been there for the ride and offered their friendship, encouragement, support, humor, and grilling skills (Tim) - thank you.

I tell recruits that our department is different because we really are a community. We might not always see eye to eye but we know each other and we are there for each other, especially when it matters. That is not something I have taken for granted. Thank you to everyone in the department for being a part of that community.

This department has not been the only special part of Nashville to me though. I was privileged to get to live with my roommate, Lora, for her three years in Nashville and step away from science for a little while when I wasn't on campus. Lora, thank you for being the best roomie, for the laughs, loving Pogo, sharing a home with me, and coming back to visit!

In my time here, I have also found a family in my church. My church family has helped me grow, encouraged me, given me opportunities to serve and lead, trusted me with their students, and has been another community for me. Their support of me, especially in the weeks leading up to the completion of this dissertation has been overwhelming and so much more than I deserve.

To the youth group - thank you for making my time with you a highlight of each week and for letting me invest in you. I am so proud of all of you.

To the ministers, parents, youth leaders (you know who you are), and other members who I am lucky enough to call friends - thank you for your leadership, for being there, for your wisdom, friendship, and accountability. You have been instrumental in the growth of my faith, you have encouraged me on the good and the bad days, and you have kept me sane by helping me keep in perspective what is really important. You have let me be real, been excited for and with me, and walked with me when I've struggled. I am so thankful. A special thank you to Becca and Natalie for not only being such great co-leaders but also for your friendship and for being examples of love and grace. To Jason - thank you for being the best co-leader I could have asked for, for teaching me so much about myself and about life, and for being an unshakable example of integrity, but most importantly for being my friend. And finally, to the Kennons who provided me with the connection that opened the door and paved the way into my next chapter.

As I look forward, I am excited to start a career in teaching. Matt gave me the opportunity to pursue my passions and the department paved the way for extra TA experience and a Certificate of College Teaching but there have been so many others who have helped

along the way. So, to everyone who has afforded me the opportunities I've had to volunteer, teach, and find myself in my passion for teaching, THANK YOU!

To Pat and VSVS - thank you for the semesters of experience and all you do for Nashville's K-12 science education.

To Jennifer - thank you for connecting accepting me into the Scientist in the Classroom Program, for funding my pursuit of a professional teaching certification, and for your guidance and encouragement.

A huge thank you to Rose Park Middle School. Specifically, to Mr. B, for welcoming me into your school and the Rose Park family, for your support, and for your love of education and to CC for being an invaluable mentor, friend, and innovator and for embodying the best of what being a teacher means.

Finally, to my family - a simple thank you will never be enough. I would not have even made it to graduate school without your unwavering love and support. Thank you, Mom and Dad, for the encouragement, phone calls, just listening when I needed to vent, surprising me with a clean house and mowed lawn when you came to visit, and for loving me unconditionally the last 27 years to make me who I am today (even during the rough pre-teen period). Rachel (and Matt), Erik, and Elise thank you for the phone calls, inside jokes, awkward stories, and for being my longest best friends. We've had a lot to celebrate in the last six years and we've had some hard times, but I've gotten to go through them all with you (albeit from afar sometimes) and it has been the biggest blessing.

To all my other friends who I have not mentioned personally or may have forgotten here who have ever offered an encouraging word or supported me, regardless of whether or not you understood what I was doing; THANK YOU!

TABLE OF CONTENTS

LIST OF TABLES

Table Page

LIST OF FIGURES

Chapter 1

INTRODUCTION

1.1 Background and Motivation

Standard experiments tend to investigate ”bulk” behavior of chemical, physical, and/or biological processes. This has proven to be incredibly helpful in advancing our understanding of all processes. However, advancements in the field of nanoscience and a more complex understanding of biological systems have required the development of new technologies that can probe systems on a single molecule level. Biological systems are unfathomably complex and crowded. The ability to separate components of biological systems is useful in gaining new insights into their behavior.

Single molecule techniques such as fluorescence, optical and magnetic trapping, and atomic force microscopy (AFM) allow for the observation of behavior of individual molecules and interactions, including rare or off-path events, that are otherwise lost in ensemble experiments. Sometimes this hidden behavior can radically shift our understanding of a system or have a dramatic effect, for example, in the development of drug targets, delivery systems, etc. This has been the case in the study of kinesins and spindle formation during mitosis as a target for cancer therapies [1, 2, 3]. Additionally, these techniques, particularly optical and magnetic trapping, allow for improved mechanical understanding of biological systems through precise, well controlled force application, which can lend itself to a more targeted approach to biological engineering applications (including protein and/or substrate mutations and modifications) and more informed endeavors in biomimetic projects.

Single molecule techniques are often used in the field of biophysics with a focus on the kinetic and mechanical behavior of biological systems. Single molecule biophysics has provided insight into systems and mechanism such as substrate mechanics and structure of DNA (reviewed in [4]), amyloid fibers [5, 6], and polysaccharides [7, 8, 9], motility

mechanisms of motor proteins like Kinesin [10, 11, 12, 13, 14, 15, 16], ClpXP [17, 18], and RNAP [19, 20, 21, 22], the physics of antigen recognition in T cells [23, 24], interaction and binding kinetics [25, 26], and structural changes using Förster (or fluorescence) resonance energy transfer (FRET) and fluorescence polarization anisotropy (FPA) techniques [27, 28, 29].

Ultimately, single molecule biophysics allows for the research of systems at a molecular level using techniques that, while offering the necessary resolution, are often too slow/time consuming for industrial R&D settings. Our work in the SM field provides the foundational and intricate understanding of systems of interest across a wide array of industries that can then be used to inform the work and progress of product and process development. Here, our work focuses on three systems of high relevance: cellulose degradation and the associated degradation enzymes (biofuels, absorption, the paper industry, etc), cellulose synthesis and the associated bacterial synthesis system (biofilm remediation and prevention), and mechanotransduction at the nucleus (medical advancement, stem cell differentiation, etc). We believe a single molecule approach to understanding each of these systems is of great value to the scientific community at large and could also lead to a greater understanding of related or parallel systems. We have chosen to explore these systems primarily using optical trapping, with a focus on the mechanical characterization, behavior, and limitations of these systems.

1.2 Biological Systems

An introduction to cellulose, the three systems introduced above (cellulose degradation, cellulose synthesis, and mechanotransduction at the nucleus), and optical trapping is provided in the following sections.

1.2.1 Cellulose structure, properties, and applications

Cellulose is the most abundant polymer on earth [30, 31], estimated to be produced at several trillion kilograms per year [32, 33, 34]. Cellulose is typically produced within the cell and transported across the cell membrane as part of the synthesis process. In plants and algae, it is most often found in the form of micro- and macro-fibirils as structural components within the cell wall. The structure of the cell wall is further supported and stabilized by close interactions with other polysaccharide polymers such as lignin, hemi-cellulose, and xylan [35, 36, 37]. Cellulose is natively found in crystalline form as cellulose I_α (algal and bacterial cellulose) and I_β (higher order plants)[38]. Bacteria, protists, and other lower order organisms can also produce cellulose. These organisms, however, often produce cellulose as disordered small amorphous bundles or single strand polymers which play an important role in the formation and stability of biofilms [39, 40, 41].

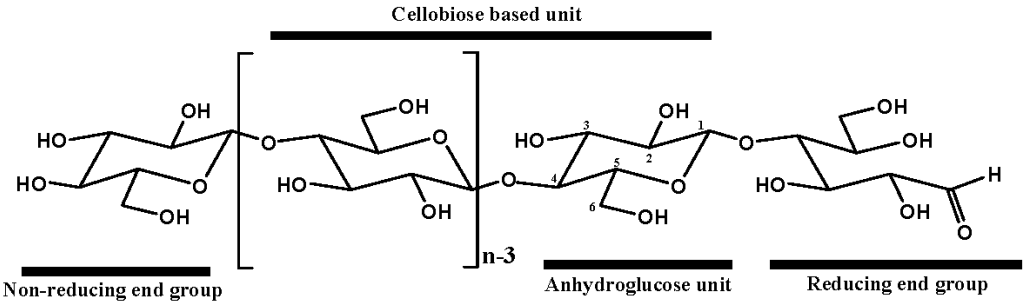

Figure 1.1: **Cellulose polymer structure.** Cellulose is a glucose polymer with cellobiose repeatable units. The polymer has both a non-reducing and reducing end as indicated in the figure. An internal glucose unit is denoted n-3 as it is the third glucose unit from the reducing end. This image is reprinted from [42] with permission under the CC BY 3.0 license.

Cellulose is a linear organic polymer consisting of glucose molecules bound by β-1,4-glycosidic bonds in which each glucose unit is rotated 180 degrees around the axis, resulting in cellobiose as the smallest repeatable unit [43] (Fig. 1.1). Cellulose is highly stable, becoming insoluble in water with as few as 6-8 glucose units [44], and exhibiting a half-life of millions of years [45]. Its stability comes from the high coordination of both

inter and intra-strand hydrogen bonding, particularly evident in the formation of crystalline cellulose fibrils [43].

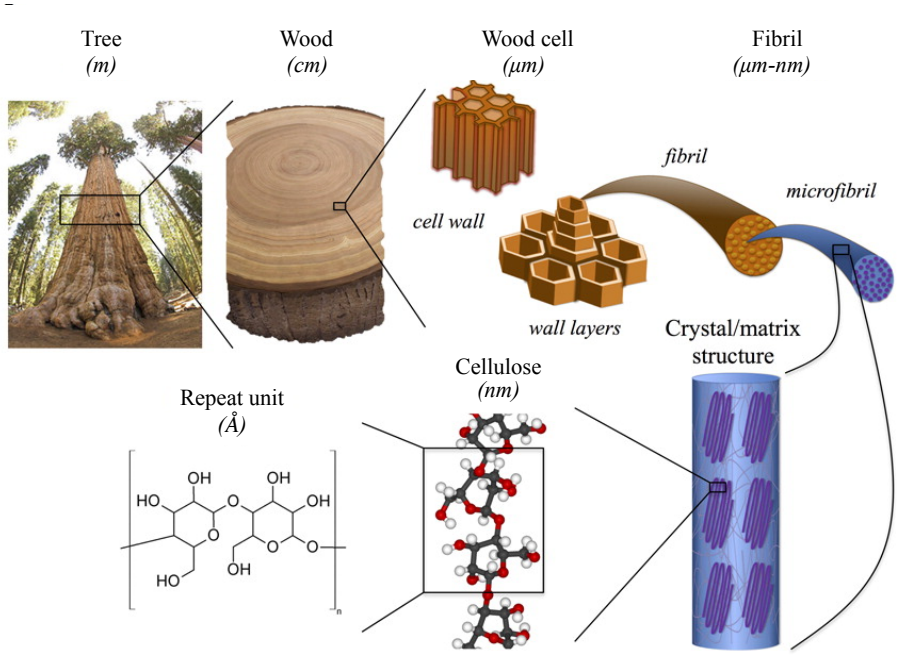

Figure 1.2: **Hierarchical structure of cellulose.** Cellulose exhibits a hierarchical structure in which individual cellulose polymers associate via hydrogen bonding to for micro- and macrofibrils. These fibrils interact with other polysaccharides such a lignin, xylan, and hemicellulose (not shown) to form the cell wall. This image is reprinted with permission from [46]. Copyright 2014 American Chemical Society.

Cellulose is structured hierarchically (Fig. 1.2), formed at the basic level by bundles of individual strands of cellulose polymer, called cellulose microfibrils, that have a diameter of 3-6 nm [47, 35]. Microfibril associations are stabilized by strong inter and intra-strand hydrogen bonding to form macrofibrils, with diameters of 10-100 nm and larger fibril groupings spanning 0.1-1μm [47]. The source of the cellulose and the exact synthesis process dictates the crystallinity of the fibril structure but can approach 95% in some cases, such as in cellulose I_α from *Cladophora* sp. (*Cladophora glomerata*) [48].

Cellulose is of great interest in many industries. Its crystalline, plant derived, form is essential to the paper and textile industries but is also of interest in pharmaceuticals, membrane/absorption processes, and biofuels. Cellulose's role in biofilms has garnered

the particular interest of the healthcare, food, and water processing industries due to the antibacterial resistant environments, and therefore health concerns, biofilms can create.

In biofuels production, decomposed cellulose, or glucose, is fermented into ethanol for fuel. However, the stable and structured nature of cellulose fibrils causes cellulosic biofuel production to be expensive. Biomass preparation prior to fermentation can be separated into three main steps. First, the material is mechanically broken down into small millimeter scale particles. Then, the material is pre-treated, often with acid at high temperature, to remove or degrade other components of the cell wall such as lignin and xylan. This step produces simple sugars, which can sometimes be collected for fermentation later. Finally, cellulose is hydrolyzed, typically using cellulolytic enzymes [35, 37]. Unfortunately, while effective, cellulases are slow, hard to recover due to strong binding to the substrate, and inherently expensive [35, 36, 37]. In fact, cellulases account for \$0.10-\$0.50 per gallon (about \$30.50 - \$152 per ton) of ethanol produced, on the order of ten times higher than enzyme costs in starch hydrolysis for corn ethanol production [35, 37, 49, 50]. If costs can be reduced, cellulosic biofuels could be a competitive fuel source as gasoline has an energy content less than three times greater than ethanol (approximately 4.66 versus 1.74 kJ/g) [51].

One approach to improving degradation rates is to improve the efficiency of the biomass preparation process. Researchers have already increased cellulase production efficiency up to 10 fold in certain fungi through mutation and directed evolution to bring enzyme costs down to that reported above [35, 52]. Genetically modified cellulosic feed stocks such as alfalfa, poplar, and others yield both reduced lignin content and co-production of cellulolytic enzymes, while pre-processing of cellulose substrates can result in a more readily hydrolyzed substrate [53]. Other researchers are pushing to develop a consolidated bioprocessing (CBP) organism that can both hydrolyze and ferment cellulose in the same reactor (progress on CBPs can be found in [54]). A third approach is focused on cellulase enzymes themselves including 1) the discovery of previously unresearched enzymes, 2) synergy

opportunities between cellulase mixtures, and 3) optimization through a more thorough understanding of model enzymes such as those from *Trichoderma reesei*.

1.2.2 Cellulose degradation

Three main types of enzymes contribute to the process of cellulose degradation: endocellulases, glucosidases, and exocellulases. Endocellulases are cutters that attack cellulose and cleave single glycosidic bonds in amorphous regions. This produces oligosaccharides, generates new chain ends, and eliminates portions of cellulose that cannot be degraded by exocellulases. Glucosidases simply work to degrade cellobiose units and other soluble oligosaccharides into glucose. Exocellulases, also called cellobiohydrolases, processively translocate along fibers and degrade crystalline cellulose into cellobiose.

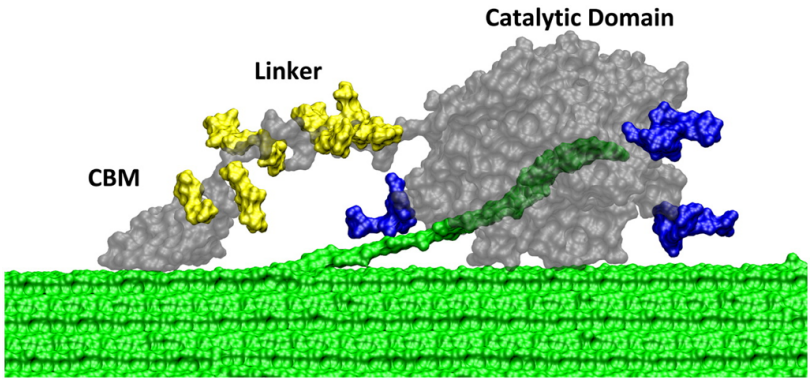

Figure 1.3: **Cellobiohydrolase structure.** Cellobiohydrolases (grey) typically consist of three main parts; the large catalytic domain (CD) which is responsible for hydrolysis, a small carbohydrate binding module (CBM) that promotes interaction with the cellulose substrate, and a short disordered peptide linker connecting the two. A single cellulose polymer (green) can be seen being pulled away from the cellulose crystal and threaded through the active tunnel of the CD from *Trichoderma reesei*. The blue and yellow portions of the enzyme represent glycosylation of the protein. This image is reprinted from [55] with permission from Elsevier.

It is thought that exocellulase activity is initiated at either the reducing or non-reducing ends (Fig. 1.1) in a process that lifts a single cellulose strand into the active site of its catalytic domain (CD). The enzyme subsequently moves along the substrate, continually hydrolyzing cellulose to single cellobiose units that are then released into solution. Exocel-

lulases typically consist of two domains connected by a flexible peptide linker (Fig. 1.3). The carbohydrate binding module (CBM) primarily works to adsorb the enzyme to the cellulose substrate, increasing the local concentration and reducing the probability that the motor will dissociate from the substrate. The CD is responsible for the hydrolysis of the cellulose strand. While it is known that the CBM does not partake in hydrolysis, it has been suggested that the CBM may disrupt hydrogen bonds in the cellulose fibril, creating a competing surface area and allowing the CD to more easily capture and hydrolyze the cellulose [36, 56, 57].

Cellulases are produced by a number of organisms but the cellobiohydrolase of interest in Chapters 2 and 3, originates from *Trichoderma reesei*, a filamentous fungus that secretes cellulases and is one of the most commonly used industrial sources of cellulases [58]. While several cellulases are present, four account for at least 90% of the secreted cellulase mixture. Cellobiohydrolase 1 (*Tr*Cel7A) and II (*Tr*Cel6A) are processive enzymes and account for 60-70% and 10-20% of the mixture, respectively. Endoglucanase I (*Tr*Cel7B) and II (*Tr*Cel5A) are cutters and account for 10-15% and 5-10% of the mixture, respectively [59]. The rest of the mixture is comprised of additional endoglucanases and glucosidases. We are specifically interested in *Tr*Cel7A. The exocellulase *Tr*Cel7A has received the most attention due to its high abundance, ability to degrade highly crystalline cellulose, and processive nature.

It has been seen that Trp40 (Fig. 1.4a), an aromatic amino acid at the opening of the active site (Fig. 1.4a), plays an essential role in the recognition of cellulose strands by *Tr*Cel7A. Simulations show that a loaded cellulose strand will be degraded as normal in a Trp40 negative mutant, but both experimental and *in silico* work have shown that an unloaded cellulose strand will not be recognized [60]. The active site of the CD is a tunnel approximately 50 Å long that includes 10 binding sites, numbered from -7 at the entrance to +3 and the exit. An aromatic amino acid is located at each binding site which can align with the sugars in a cellulose strand and create hydrogen bonds with the cellulose [61, 62].

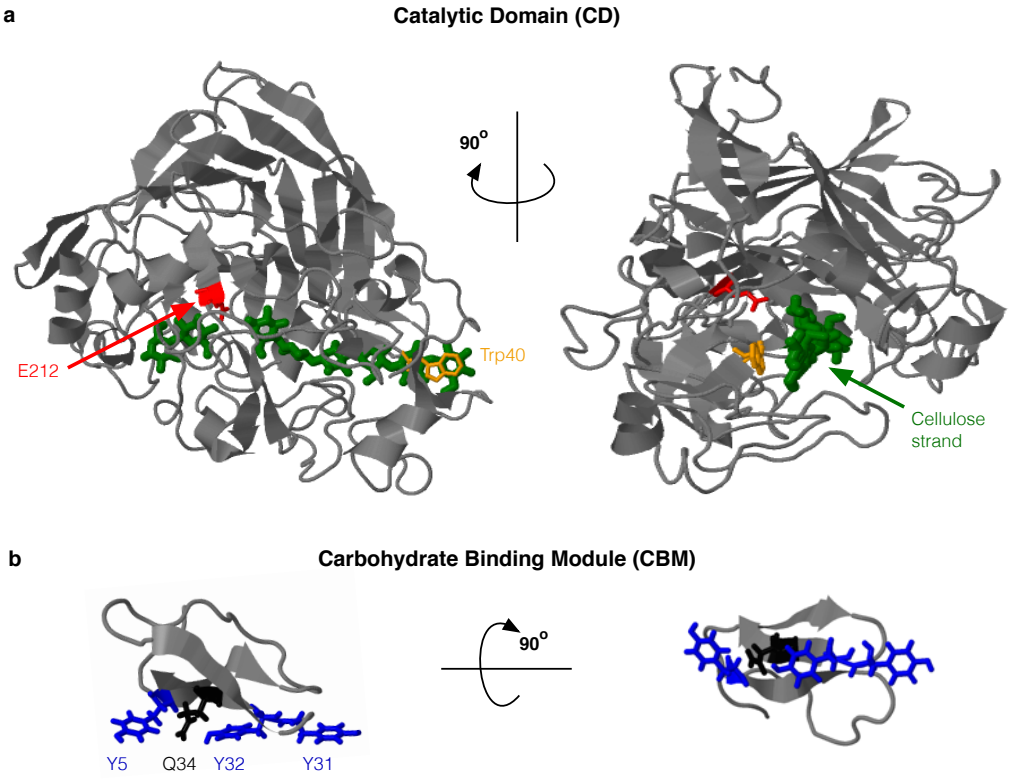

Figure 1.4: **Key residues of cellobiohydrolase from *Trichoderma reesei*** are found on both the CD and CBM. On the CD (a), the Trp40 residue (orange) is located at the entrance to the active tunnel and regulates the initial interaction of cellulose with the active tunnel (PDB - 7CEL). E212 (red) is located approximately three quarters of the way down the active tunnel and acts as the proton donor for hydrolysis. The key residues in the CBM (b) create the interacting surface of the CBM and include the aromatic residues Y5, Y31, and Y32 (blue) as well as glutamine Q34 (PDB - 2CBH).

Hydrolysis occurs between sites -1 and +1 with the cellobiose product bound to the +1 and +2 sites. A glutamic acid at residue 212 acts as the proton donor for hydrolysis (Fig. 1.4a) [61, 63]. The CBM interacts with cellulose through three aromatic tyrosine residues (Y5, Y31, and Y32) as well as a glutamine residue (Q34) on it its binding surface (Fig. 1.4b) [64].

1.2.3 Cellulose synthesis

Despite the focus on cellulose degradation, relatively little is known about the mechanism of cellulose synthesis. Cellulose is produced by a wide array of organisms, for a variety of functions, but is always, according to current research in the field, secreted extracellularly to the surrounding matrix or incorporated into the cell wall. Comprehensive reviews of cellulose, the cell wall, and biofuel production can be found in [65, 35, 32]. While the exact architecture and combination of enzymes necessary for optimum synthesis, translocation, and larger structural assembly vary based on the organism and the ultimate cellulose structure produced, there are several conserved components of the system. The enzymes involved in synthesizing cellulose belong to an enzyme family called glycosyl transferases (GT) and are referred to as cellulose synthases (CeS).

All CeS systems must function to both synthesize cellulose and translocate the synthesized polymer across the membrane to the outside of the cell [45, 66]. Every system studied to this point has a conserved catalytic protein called the "A" subunit which extends from the cytosol and through the inner membrane. This catalytic subunit polymerizes cellulose by adding an individual glucose unit to the chain and translocating the polymer through a transmembrane tunnel by one unit in order to reset the process and allow for the addition of the next subunit [45]. Other subunits in the system have varying functions (some yet unknown), but must somehow work to successfully guide the polymer across the periplasm and into another membrane integrated protein that ultimately exports the polymer to the surrounding environment.

Bacterial cellulose synthases (Bcs) have been of particular interest due to their role in the formation of biofilms and the resulting interest in understanding these systems for the development of biofilm remediation processes and biofilm resistant materials, particularly for use in healthcare related fields. Bcs, specifically the BcsAB complex from *Rhodobacter sphaeroides*, is the system of interest in Chapter 4. Bcs consists of at least five subunits: A,B,C,D, and Z (Fig. 1.5a). However, only subunit A and the C-terminal transmembrane

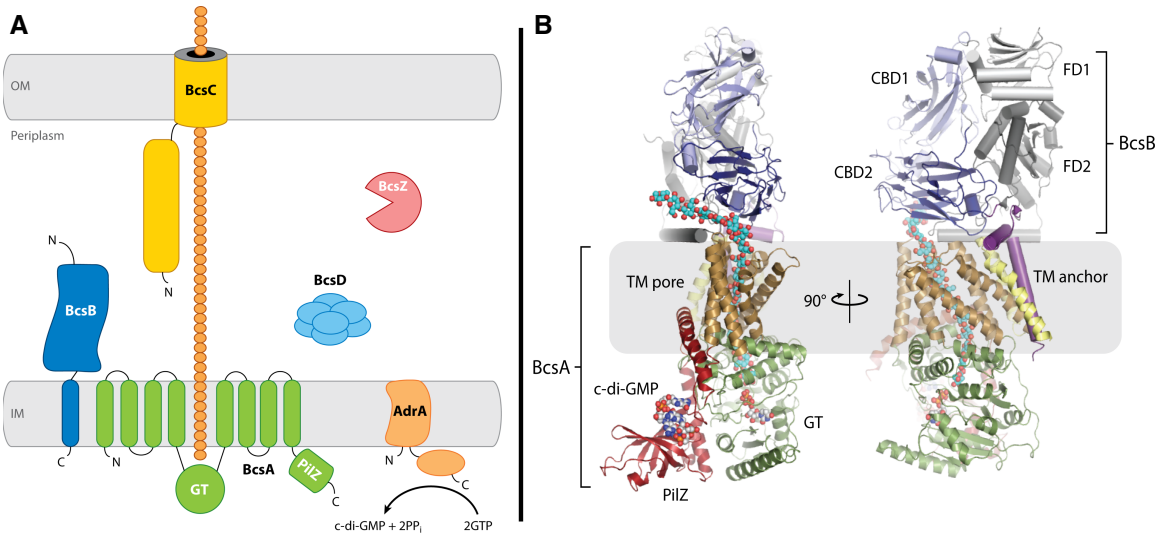

Figure 1.5: **Bacterial cellulose synthases.** The Bcs system (A) consists of several components including BcsA, the catalytic protein located at the inner membrane, BcsB, which intimately interacts with BcsA, BcsC which transports synthesized cellulose across the outer membrane, and BcsD and BcsZ periplasmic proteins. (B) BcsA is the catalytically active protein, however, the transmembrane (TM) region of BcsB (purple) is also necessary for synthesis *in vivo*. BcsA contains the active site in the glycosyltransferase (GT) domain (green) which extends into a pore through the rest of the BcsA and houses 10 units of synthesized cellulose before depositing the cellulose in the periplasmic space. Access to the active site is dictated by the small molecule c-di-GMP which binds in the PilZ domain (red). Both panels of this figure are reprinted from [45] with permission.

anchor of BcsB are necessary for cellulose synthesis *in vitro* [67]. As already described, BcsA is a transmembrane protein. Its active site is located within the glycosyl transferase domain in the cytosol where UDP activated glucose (UDP-glucose) substrate binds before addition to the cellulose polymer [66, 68]. The cytosolic portion also includes a PilZ domain that binds cyclic-di-GMP (c-di-GMP), a small molecule that regulates the accessibility of the active site by opening a 'gating loop' upon binding [69, 70]. The rest of BcsA extends through membrane to create a transmembrane (TM) pore. This pore houses the ten newest glucose units of the synthesized cellulose polymer [66]. Upon leaving BcsA and entering the periplasm, cellulose comes into contact with BcsB, which is anchored to the inner membrane via its C terminus. A detailed representation of BcsAB is provided in Fig. 1.5b. It is unclear the exact role of BcsB, beyond that it is essential for cellulose

synthesis.

BcsC is responsible for transmembrane translocation across the outer membrane [71]. The mechanism of BcsC is unknown, but it is possible it contacts BcsB in the periplasm, guiding cellulose into the pore it creates through the outer membrane to transports cellulose out of the cell. The function of the other subunits, BcsD and BcsZ are unknown, but they are both required for optimum cellulose synthesis *in vivo* [72]. BscD is thought to be a periplasmic protein but even that is unclear [73, 74]. BcsZ is known to be periplasmic and to exhibit hydrolytic activity on oligosaccarides [75, 76]. Thus, it could be suggested that perhaps BcsZ provides a form of quality control, cleaving cellulose that is misformed, misguided through the periplasm, or too long, or in an effort to prevent unsustainable or damaging forces from a build-up of polymer in the perplasmic space as it exits the minimal BcsAB catalytic complex.

1.2.4 The Nuclear Membrane

Force plays a large role in cell motility [77, 78, 79, 80], differentiation [81, 82], signal transduction [83, 84, 85], and environmental recognition [86]. A significant amount of research has been done to investigate how forces are recognized and transferred across the cell membrane. Force inputs can open ion channels in the membrane [87], cause assembly of focal adhesions [88, 80], control the behavior of binding sites [23], etc. The membrane is also physically linked to the nucleus via cytoskeletal elements such as actin, microtubules, and intermediate filaments. Without a direct connection, it would be difficult to imagine how external forces cause genetic changes, but how exactly are external force inputs transduced across the cell to DNA in the nucleus? The answer may lie, in part, in the nuclear membrane. Unfortunately, the nucleus and nuclear membrane are harder to study than the cellular membrane, leaving much to be discovered.

The nuclear membrane is a highly complex environment acting to protect the cell's genetic information and allowing for communication between the nucleus, the cell, and

the extracellular environment. The membrane acts much like the cellular membrane in that it controls what enters and leaves the nucleus, contains transmembrane proteins, pore complexes, and provides anchoring points that allow for the maintenance of the structural integrity of the cell and nucleus.

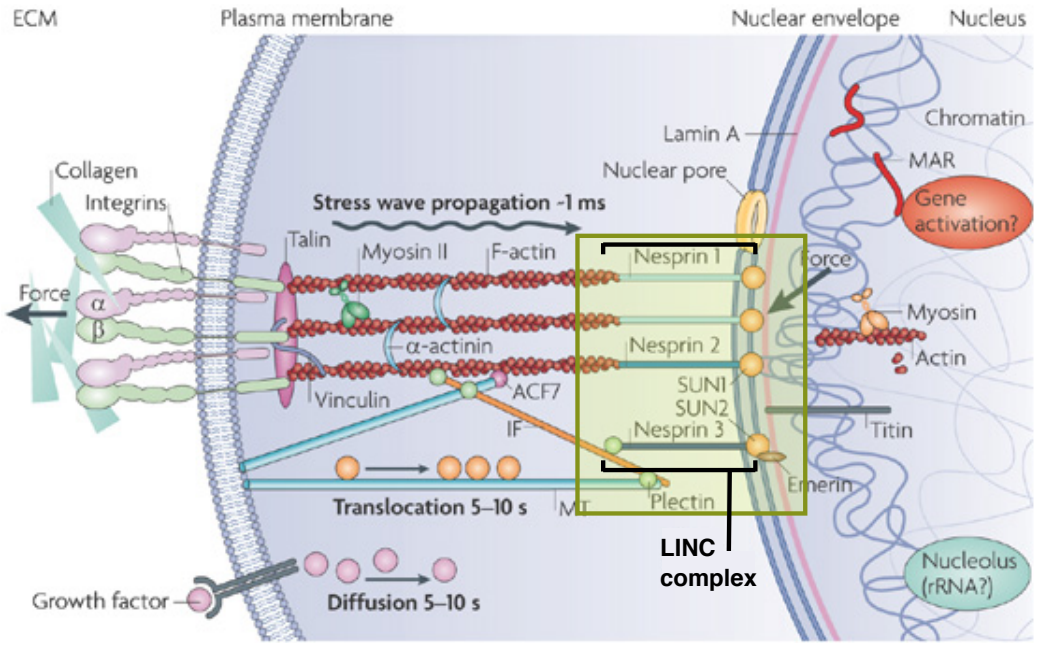

Figure 1.6: **Physical linkages from the ECM to the nucleus.** Cells often experience forces originating in the extracellular matrix (ECM). These forces are communicated to the nucleus by mechanicaltransduction through the physical linkage of collagen and integrins in the ECM to cytoskeletal elements and then to the nuclear membrane. The complexes connecting the cytoskeletal elements (F-actin, microtubules, and intermediate filaments) to the nuclear membrane are called LINC (linker of the nucleoskeleton and cytoskeleton) complexes. In these complexes, the cytoskeletal elements are bound to large transmembrane proteins called nesprins. The transmembrane domain of these proteins, the KASH domain, then interacts with SUN proteins in the perinuclear space which are anchored in the inner nuclear membrane and provide a link to the lamina and other nuclear components. This figure has been adapted by permission from Macmillan Publishers Ltd: Nature Reviews Molecular Cell Biology [89], copyright 2009.

In Chapter 5, we explore interactions at the nuclear membrane and are primarily interested in the interactions between cytoskeletal components, actin and plectin, and the nuclear membrane, likely through the LINC (linker of nucleoskeleton and cytoskeleton) complex, a transmembrane complex that anchors cytoskeletal elements at the outer nuclear membrane and the lamina (Fig. 1.6). The lamina is a structural layer comprised mostly of

lamin intermediate filaments, at the inner membrane of the nucleus. The LINC complex consists of several components. The SUN protein exists as a trimer and extends from its C-terminus in the inner nuclear membrane, where it interacts with the lamina, to the perinuclear space in which the N-terminus interacts with the KASH domains of nesprins 1-4 (nuclear envelope spectrin repeat proteins) [89, 90]. Nesprins are huge proteins (MDa), with nesprin 3 being considerably smaller than the others [91, 92], that extend from their KASH domains in the perinuclear space, through the outer nuclear membrane and into the cytoplasm where they bind specific cytoskeletal elements. Nesprins 1 and 2 primarily bind filamentous actin, nesprin 3 binds intermediate filaments via the actin binding domain (ABD) of plectin, and nesprin 4 binds microtubules via kinesins [91, 93, 94, 95, 96]. There are also a number of other LINC associated proteins that likely reside within the proximity of the LINC complex and may affect its behavior, but are not primary players in the LINC interactions.

1.3 Single Molecule Methods - Optical Trapping

There are a number of techniques that may be used in single molecule investigations, each with its own unique advantages and disadvantages. Techniques include fluorescence and force microscopy in which force microscopy can be further broken down to include atomic force microscopy (AFM), magnetic tweezers, and optical tweezers. Fluorescence is largely used in no force environments to probe kinetics, affinities, and angstrom size conformational changes using techniques such as Förster (or fluorescence) resonance energy transfer (FRET) [97, 98]. The development of new fluorescence based techniques have also allowed for super resolution imaging that eliminates the diffraction limit as a barrier to improved spatial resolution (ie. SHREC - Single-Molecule High-Resolution Colocalization [99], FIONA - Fluorescence Imaging with One Nanometer Accuracy [100], STORM - Stochastic Optical Reconstruction Microscopy [101], LLSM - Lattice Light-Sheet Microscopy [102, 103]). Alternatively, force spectroscopy methods allow for the physical

manipulation of the system of interest. AFM allows for the application of high forces (nanoNewtons) coupled with nanometer resolution. Magnetic tweezers allow for quantitative rotational force and the possibility of higher throughput assays. Optical tweezers provide a combination of picoNewton force and nanometer spatial resolution in real time (millisecond up to microsecond resolution, depending on the assay). These three methods are reviewed in [104]. Advancements in technology and single molecule techniques have also lead to methods which allow for the combination of these techniques (reviewed in [105]).

In this work, the primary method of investigation is optical trapping. This method was chosen for its combination of high spatial (nm), force (pN), and time resolution (ms). The systems of interest do not reside in zero force environments, so the ability to probe the effects of mechanical inputs on these systems is crucial to a complete understanding of their behavior.

The phenomenon of optical trapping was first demonstrated in the 1970's and 80's by Arthur Ashkin [107, 108, 109] and involves the use of a highly focused laser beam to hold and manipulate a small (μm scale) dielectric particle (Fig. 1.7). Light has momentum and when it comes into contact with a dielectric particle a scattering force is generated along the propagation axis as the light refracts through the particle. When the light is tightly focused with a Gaussian intensity distribution, a gradient force is also produced as a result of the steep change in intensity which works to pull the particle towards the center of the light source. To maximize trapping strength and quality, the laser is expanded to fill the back of a high numerical aperture (NA) objective before being focused to a point. This increases the gradient of laser power, thus increasing the gradient force and maximizing trap stiffness. Conveniently, within a radius of approximately 150 nm from the laser axis, an optical trap behavior as a Hookian spring with force being proportional to the product of trap stiffness and displacement from the trap center, allowing for high position and force resolution and easy calculation of the force [106].

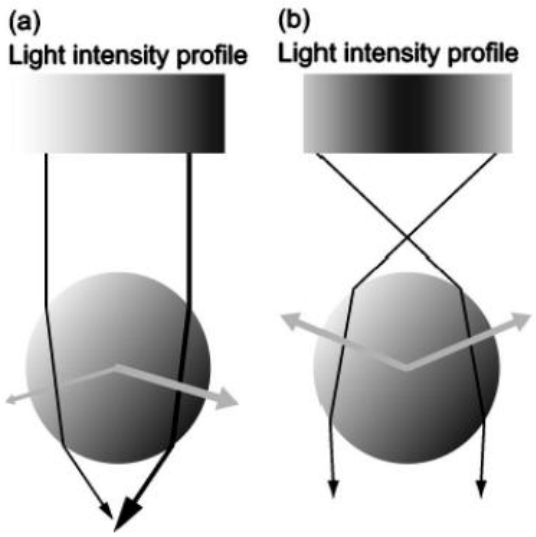

Figure 1.7: **Optical trapping** An optical trap is formed when a laser with a gaussian intensity distribution is tightly focused to a point by means of a high numerical aperature objective. In (a), a linear, unfocused, intensity profile is depicted with black indicating highest intensity. Two representative rays are shown (black lines) to refract through the spherical particle (also representative of the change in momentum experience by the light). The result is a scattering force in the direction of light propagation (down the page) and resulting gradient forces in the direction of high light intensity (gray vectors). This yields a net force towards the high intensity region of the light. Without the light being focused, the scattering force overpowers the gradient force and the bead is pushed forward rather than pulled toward the high intensity at a beam waste. Alternatively, if the light has a gaussian intensity profile, is tightly focus, and the bead is centered in the intensity profile (b), the bead becomes trapped in the center of the beam, just past the beam waste. In this case, the gradient force is greater than scattering force. Since the object is centered around the light intensity, the net lateral force is zero. This image is reprinted from [106], with permission from AIP Publishing.

An optical trapping phenomena exists when the species of interest has an index of refraction larger than that of the medium in which it resides and when the size of the species being trapped is close to the wavelength of the trapping laser (0.1-10λ), however, particles smaller than 100-200 nm become less practical as the force that can be applied is limited and they are hard to observe visually, even with a 100x microscope. This range includes many biological species of interest. For species that are too small to trap or observe by themselves, such as molecular motors, dielectric microspheres are functionalized and used as handles to indirectly apply force and visualize motor behavior, as seen in the following

chapters.

Theoretically, a laser of any wavelength can be used to generate an optical trap, but lasers in the near infrared are typically used as light at these wavelengths cause the least absorption in biological samples (we use 1064 nm trapping lasers) and thus the least biological disruption [110, 111, 112]. This design decision also allows for the coupling of optical trapping and fluorescence techniques as the wavelengths of visible light are left available.

Additionally, an optical trapping system can be modified to include a second laser, referred to as a detection laser, to track position with high time and spatial resolution [113, 106, 114]. Typical spatial resolution is on the nanometer scale, however, systems with resolutions up to 3 $\AA$ have been developed [21, 115]. This detection laser is used at low power ($\sim$ 1/10 the power of the trapping laser) to limit interference with the trap by creating a secondary trap. The detection laser is also often in the near IR region with a wavelength slightly lower than that of the trapping laser (975 nm in our case) to allow for differentiation of the signals.

There are a number of methods for the calibration of both position and trap stiffness. There are advantages and disadvantages to each. Details on these methods can be found in the review of optical trapping by Neuman et al. [106]. Here, we use a detection laser for position detection and allow for the control of trap position using acousto-optic deflectors (AODs). To calibrate position, the trap is moved in steps of a fixed distance throughout the detection zone using the AODs. After position is calibrated, we find the trap stiffness using the equipartition method which tracks the variance of a trapped object and does not require knowledge of the viscosity of the sample media or the size/shape of the object. From trap stiffness, force can easily be calculated by multiplying the stiffness by the magnitude of the object displacement from the center of the trap.

1.4 Bibliography

[1] David Vanneste, Masatoshi Takagi, Naoko Imamoto, and Isabelle Vernos. The role of Hklp2 in the stabilization and maintenance of spindle bipolarity. *Curr Biol*, 19(20):1712–7, Nov 2009.

[2] Marvin E Tanenbaum, Libor Macůrek, Aniek Janssen, Erica F Geers, Mónica Alvarez-Fernández, and René H Medema. Kif15 cooperates with eg5 to promote bipolar spindle assembly. *Curr Biol*, 19(20):1703–11, Nov 2009.

[3] Emma G Sturgill and Ryoma Ohi. Kinesin-12 differentially affects spindle assembly depending on its microtubule substrate. *Curr Biol*, 23(14):1280–90, Jul 2013.

[4] C Bustamante, S B Smith, J Liphardt, and D Smith. Single-molecule studies of DNA mechanics. *Curr Opin Struct Biol*, 10(3):279–85, Jun 2000.

[5] Carlos E Castro, Jijun Dong, Mary C Boyce, Susan Lindquist, and Matthew J Lang. Physical properties of polymorphic yeast prion amyloid fibers. *Biophys J*, 101(2):439–48, Jul 2011.

[6] Angel Orte, Neil R Birkett, Richard W Clarke, Glyn L Devlin, Christopher M Dobson, and David Klenerman. Direct characterization of amyloidogenic oligomers by single-molecule fluorescence. *Proc Natl Acad Sci U S A*, 105(38):14424–9, Sep 2008.

[7] P E Marszalek, A F Oberhauser, Y P Pang, and J M Fernandez. Polysaccharide elasticity governed by chair-boat transitions of the glucopyranose ring. *Nature*, 396(6712):661–4, Dec 1998.

[8] Rief, Oesterhelt, Heymann, and Gaub. Single molecule force spectroscopy on polysaccharides by atomic force microscopy. *Science*, 275(5304):1295–7, Feb 1997.

[9] P E Marszalek, H Li, and J M Fernandez. Fingerprinting polysaccharides with single-molecule atomic force microscopy. *Nat Biotechnol*, 19(3):258–62, Mar 2001.

[10] D S Friedman and R D Vale. Single-molecule analysis of kinesin motility reveals regulation by the cargo-binding tail domain. *Nat Cell Biol*, 1(5):293–7, Sep 1999.

[11] Ahmet Yildiz, Michio Tomishige, Ronald D Vale, and Paul R Selvin. Kinesin walks hand-over-hand. *Science*, 303(5658):676–8, Jan 2004.

[12] Steven M Block, Charles L Asbury, Joshua W Shaevitz, and Matthew J Lang. Probing the kinesin reaction cycle with a 2D optical force clamp. *Proc Natl Acad Sci U S A*, 100(5):2351–6, Mar 2003.

[13] Wonmuk Hwang, Matthew J Lang, and Martin Karplus. Force generation in kinesin hinges on cover-neck bundle formation. *Structure*, 16(1):62–71, Jan 2008.

[14] Ahmad S Khalil, David C Appleyard, Anna K Labno, Adrien Georges, Martin Karplus, Angela M Belcher, Wonmuk Hwang, and Matthew J Lang. Kinesin's cover-neck bundle folds forward to generate force. *Proc Natl Acad Sci U S A*, 105(49):19247–52, Dec 2008.

[15] William R Hesse, Miriam Steiner, Matthew L Wohlever, Roger D Kamm, Wonmuk Hwang, and Matthew J Lang. Modular aspects of kinesin force generation machinery. *Biophys J*, 104(9):1969–78, May 2013.

[16] Yongdae Shin, Yaqing Du, Scott E Collier, Melanie D Ohi, Matthew J Lang, and Ryoma Ohi. Biased Brownian motion as a mechanism to facilitate nanometer-scale exploration of the microtubule plus end by a kinesin-8. *Proceedings of the National Academy of Sciences*, 112(29):E3826–E3835, 2015.

[17] Yongdae Shin, Joseph H Davis, Ricardo R Brau, Andreas Martin, Jon A Kenniston, Tania A Baker, Robert T Sauer, and Matthew J Lang. Single-molecule denaturation

and degradation of proteins by the AAA+ ClpXP protease. *Proc Natl Acad Sci U S A*, 106(46):19340–5, Nov 2009.

[18] Juan Carlos Cordova, Adrian O Olivares, Yongdae Shin, Benjamin M Stinson, Stephane Calmat, Karl R Schmitz, Marie-Eve Aubin-Tam, Tania A Baker, Matthew J Lang, and Robert T Sauer. Stochastic but highly coordinated protein unfolding and translocation by the ClpXP proteolytic machine. *Cell*, 158(3):647–58, Jul 2014.

[19] R J Davenport, G J Wuite, R Landick, and C Bustamante. Single-molecule study of transcriptional pausing and arrest by E. coli RNA polymerase. *Science*, 287(5462):2497–500, Mar 2000.

[20] M D Wang, M J Schnitzer, H Yin, R Landick, J Gelles, and S M Block. Force and velocity measured for single molecules of RNA polymerase. *Science*, 282(5390):902–7, Oct 1998.

[21] Joshua W Shaevitz, Elio A Abbondanzieri, Robert Landick, and Steven M Block. Backtracking by single RNA polymerase molecules observed at near-base-pair resolution. *Nature*, 426(6967):684–687, 2003.

[22] Kristina M Herbert, William J Greenleaf, and Steven M Block. Single-molecule studies of RNA polymerase: motoring along. *Annu Rev Biochem*, 77:149–76, 2008.

[23] Dibyendu Kumar Das, Yinnian Feng, Robert J Mallis, Xiaolong Li, Derin B Keskin, Rebecca E Hussey, Sonia K Brady, Jia-Huai Wang, Gerhard Wagner, Ellis L Reinherz, et al. Force-dependent transition in the T-cell receptor β-subunit allosterically regulates peptide discrimination and pMHC bond lifetime. *Proceedings of the National Academy of Sciences*, 112(5):1517–1522, 2015.

[24] Dibyendu Kumar Das, Robert J Mallis, Jonathan S Duke-Cohan, Rebecca E Hussey, Paul W Tetteh, Mark Hilton, Gerhard Wagner, Matthew J Lang, and Ellis L Reinherz.

Pre-T cell receptors (pre-TCRs) leverage Vβ complementarity determining regions (CDRs) and hydrophobic patch in mechanosensing thymic self-ligands. *J Biol Chem*, 291(49):25292–25305, Dec 2016.

[25] Ralf Jungmann, Christian Steinhauer, Max Scheible, Anton Kuzyk, Philip Tinnefeld, and Friedrich C Simmel. Single-molecule kinetics and super-resolution microscopy by fluorescence imaging of transient binding on DNA origami. *Nano Lett*, 10(11):4756–61, Nov 2010.

[26] Joshua R Wayment and Joel M Harris. Biotin-avidin binding kinetics measured by single-molecule imaging. *Anal Chem*, 81(1):336–42, Jan 2009.

[27] Shimon Weiss. Measuring conformational dynamics of biomolecules by single molecule fluorescence spectroscopy. *Nature Structural & Molecular Biology*, 7(9):724, 2000.

[28] Harold D Kim, G Ulrich Nienhaus, Taekjip Ha, Jeffrey W Orr, James R Williamson, and Steven Chu. Mg2+-dependent conformational change of RNA studied by fluorescence correlation and FRET on immobilized single molecules. *Proceedings of the National Academy of Sciences*, 99(7):4284–4289, 2002.

[29] Yusdi Santoso, Catherine M Joyce, Olga Potapova, Ludovic Le Reste, Johannes Hohlbein, Joseph P Torella, Nigel DF Grindley, and Achillefs N Kapanidis. Conformational transitions in DNA polymerase I revealed by single-molecule FRET. *Proceedings of the National Academy of Sciences*, 107(2):715–720, 2010.

[30] Mihhail Kurasin and Priit Väljamäe. Processivity of cellobiohydrolases is limited by the substrate. *J Biol Chem*, 286(1):169–77, Jan 2011.

[31] Antoinette C O'sullivan. Cellulose: the structure slowly unravels. *Cellulose*, 4(3):173–207, 1997.

[32] Markus Pauly and Kenneth Keegstra. Cell-wall carbohydrates and their modification as a resource for biofuels. *The Plant Journal*, 54(4):559–568, 2008.

[33] Chris Somerville. Cellulose synthesis in higher plants. *Annu Rev Cell Dev Biol*, 22:53–78, 2006.

[34] Deborah P. Delmer. Cellulose biosynthesis: Exciting times for a difficult field of study. *Annu Rev Plant Physiol Plant Mol Biol*, 50:245–276, Jun 1999.

[35] Douglas B Jordan, Michael J Bowman, Jay D Braker, Bruce S Dien, Ronald E Hector, Charles C Lee, Jeffrey A Mertens, and Kurt Wagschal. Plant cell walls to ethanol. *Biochem J*, 442(2):241–52, Mar 2012.

[36] J.S. Van Dyk and B.I. Pletschke. A review of lignocellulose bioconversion using enzymatic hydrolysis and synergistic cooperation between enzymes - factors affecting enzymes, conversion and synergy. *Biotechnology Advances*, 30(6):1458 – 1480, 2012. Special issue on {ACB} 2011.

[37] Andrew Carroll and Chris Somerville. Cellulosic biofuels. *Annu Rev Plant Biol*, 60:165–82, 2009.

[38] Rajai H Atalla and David L VanderHart. Native cellulose: a composite of two distinct crystalline forms. *Science*, 223:283–286, 1984.

[39] Diego O Serra, Anja M Richter, and Regine Hengge. Cellulose as an architectural element in spatially structured Escherichia coli biofilms. *J Bacteriol*, 195(24):5540–54, Dec 2013.

[40] Courtney E Jahn, Dija A Selimi, Jeri D Barak, and Amy O Charkowski. The Dickeya dadantii biofilm matrix consists of cellulose nanofibres, and is an emergent property dependent upon the type III secretion system and the cellulose synthesis operon. *Microbiology*, 157(Pt 10):2733–44, Oct 2011.

[41] Oscar A McCrate, Xiaoxue Zhou, Courtney Reichhardt, and Lynette Cegelski. Sum of the parts: composition and architecture of the bacterial extracellular matrix. *J Mol Biol*, 425(22):4286–94, Nov 2013.

[42] Poonam Singh, Hugo Duarte, Luís Alves, Filipe Antunes, Nicolas Le Moigne, Jan Dormanns, Benoît Duchemin, Mark P Staiger, and Bruno Medronho. From cellulose dissolution and regeneration to added value applications—synergism between molecular understanding and material development. *Cellulose-Fundamental Aspects and Current Trends*, 2015.

[43] Dieter Klemm, Brigitte Heublein, Hans-Peter Fink, and Andreas Bohn. Cellulose: fascinating biopolymer and sustainable raw material. *Angew Chem Int Ed Engl*, 44(22):3358–93, May 2005.

[44] Matthew C Gray, Alvin O Converse, and Charles E Wyman. Sugar monomer and oligomer solubility: data and predictions for application to biomass hydrolysis. *Appl Biochem Biotechnol*, 105 -108:179–93, 2003.

[45] Joshua T McNamara, Jacob L W Morgan, and Jochen Zimmer. A molecular description of cellulose biosynthesis. *Annu Rev Biochem*, 84:895–921, 2015.

[46] Robert Sinko, Shawn Mishra, Luis Ruiz, Nick Brandis, and Sinan Keten. Dimensions of biological cellulose nanocrystals maximize fracture strength. *ACS Macro Letters*, 3(1):64–69, 2013.

[47] Jingpeng Wang, Amanda Quirk, Jacek Lipkowski, John R Dutcher, Christopher Hill, Adam Mark, and Anthony J Clarke. Real-time observation of the swelling and hydrolysis of a single crystalline cellulose fiber catalyzed by cellulase 7B from Trichoderma reesei. *Langmuir*, 28(25):9664–72, Jun 2012.

[48] Albert Mihranyan, Assumpcio Piñas Llagostera, Richard Karmhag, Maria Strømme,

and Ragnar Ek. Moisture sorption by cellulose powders of varying crystallinity. *Int J Pharm*, 269(2):433–42, Jan 2004.

[49] John Houghton, Sharlene Weatherwax, and John Ferrell. *Breaking the Biological Barriers to Cellulosic Ethanol: A Joint Research Agenda*. Jun 2006.

[50] Mats Galbe, Per Sassner, Anders Wingren, and Guido Zacchi. *Process Engineering Economics of Bioethanol Production*, pages 303–327. Springer Berlin Heidelberg, Berlin, Heidelberg, 2007.

[51] Evandro Novaes, Matias Kirst, Vincent Chiang, Heike Winter-Sederoff, and Ronald Sederoff. Lignin and biomass: a negative correlation for wood formation and lignin content in trees. *Plant Physiol*, 154(2):555–61, Oct 2010.

[52] Alexander V Gusakov. Alternatives to Trichoderma reesei in biofuel production. *Trends in biotechnology*, 29(9):419–425, 2011.

[53] Shishir P S Chundawat, Giovanni Bellesia, Nirmal Uppugundla, Leonardo da Costa Sousa, Dahai Gao, Albert M Cheh, Umesh P Agarwal, Christopher M Bianchetti, George N Phillips, Jr, Paul Langan, Venkatesh Balan, S Gnanakaran, and Bruce E Dale. Restructuring the crystalline cellulose hydrogen bond network enhances its depolymerization rate. *J Am Chem Soc*, 133(29):11163–74, Jul 2011.

[54] Daniel G Olson, John E McBride, A Joe Shaw, and Lee R Lynd. Recent progress in consolidated bioprocessing. *Curr Opin Biotechnol*, 23(3):396–405, Jun 2012.

[55] Gregg T Beckham, Yannick J Bomble, James F Matthews, Courtney B Taylor, Michael G Resch, John M Yarbrough, Steve R Decker, Lintao Bu, Xiongce Zhao, Clare McCabe, Jakob Wohlert, Malin Bergenstråhle, John W Brady, William S Adney, Michael E Himmel, and Michael F Crowley. The O-glycosylated linker from the Trichoderma reesei family 7 cellulase is a flexible, disordered protein. *Biophys J*, 99(11):3773–81, Dec 2010.

[56] Jing Guo and Jeffrey M Catchmark. Binding specificity and thermodynamics of cellulose-binding modules from Trichoderma reesei Cel7A and Cel6A. *Biomacromolecules*, 14(5):1268–77, May 2013.

[57] Mingyu Wang, Kai Liu, Li Dai, Jie Zhang, and Xu Fang. The structural and biochemical basis for cellulose biodegradation. *Journal of Chemical Technology and Biotechnology*, 88(4):491–500, 2013.

[58] A V Markov, A V Gusakov, E G Kondratyeva, O N Okunev, A O Bekkarevich, and A P Sinitsyn. New effective method for analysis of the component composition of enzyme complexes from Trichoderma reesei. *Biochemistry (Mosc)*, 70(6):657–63, Jun 2005.

[59] Judith Kolbe and Christian P. Kubicek. Quantification and identification of the main components of the Trichoderma cellulase complex with monoclonal antibodies using an enzyme-linked immunosorbent assay (ELISA). *Applied Microbiology and Biotechnology*, 34(1):26–30, 1990.

[60] Akihiko Nakamura, Takeshi Tsukada, Sanna Auer, Tadaomi Furuta, Masahisa Wada, Anu Koivula, Kiyohiko Igarashi, and Masahiro Samejima. The tryptophan residue at the active site tunnel entrance of Trichoderma reesei cellobiohydrolase Cel7A is important for initiation of degradation of crystalline cellulose. *J Biol Chem*, 288(19):13503–10, May 2013.

[61] C Divne, J Ståhlberg, T T Teeri, and T A Jones. High-resolution crystal structures reveal how a cellulose chain is bound in the 50 å long tunnel of cellobiohydrolase I from Trichoderma reesei. *J Mol Biol*, 275(2):309–25, Jan 1998.

[62] Janne Lehtiö, Junji Sugiyama, Malin Gustavsson, Linda Fransson, Markus Linder, and Tuula T Teeri. The binding specificity and affinity determinants of family 1 and

family 3 cellulose binding modules. *Proc Natl Acad Sci U S A*, 100(2):484–9, Jan 2003.

[63] J Ståhlberg, C Divne, A Koivula, K Piens, M Claeyssens, T T Teeri, and T A Jones. Activity studies and crystal structures of catalytically deficient mutants of cellobiohydrolase I from Trichoderma reesei. *J Mol Biol*, 264(2):337–49, Nov 1996.

[64] Maija-Liisa Mattinen, Markus Linder, Anita Teleman, and Arto Annila. Interaction between cellohexaose and cellulose binding domains from Trichoderma reesei cellulases. $\{FEBS\}$ *Letters*, 407(3):291 – 296, 1997.

[65] Kenneth Keegstra. Plant cell walls. *Plant Physiol*, 154(2):483–6, Oct 2010.

[66] Jacob L W Morgan, Joanna Strumillo, and Jochen Zimmer. Crystallographic snapshot of cellulose synthesis and membrane translocation. *Nature*, 493(7431):181–6, Jan 2013.

[67] Okako Omadjela, Adishesh Narahari, Joanna Strumillo, Hugo Mélida, Olga Mazur, Vincent Bulone, and Jochen Zimmer. BcsA and BcsB form the catalytically active core of bacterial cellulose synthase sufficient for in vitro cellulose synthesis. *Proc Natl Acad Sci U S A*, 110(44):17856–61, Oct 2013.

[68] Jacob L W Morgan, Joshua T McNamara, Michael Fischer, Jamie Rich, Hong-Ming Chen, Stephen G Withers, and Jochen Zimmer. Observing cellulose biosynthesis and membrane translocation in crystallo. *Nature*, 531(7594):329–34, Mar 2016.

[69] Jacob L W Morgan, Joshua T McNamara, and Jochen Zimmer. Mechanism of activation of bacterial cellulose synthase by cyclic di-GMP. *Nat Struct Mol Biol*, 21(5):489–96, May 2014.

[70] Peggy A Cotter and Scott Stibitz. c-di-GMP-mediated regulation of virulence and biofilm formation. *Curr Opin Microbiol*, 10(1):17–23, Feb 2007.

[71] Carrie-Lynn Keiski, Michael Harwich, Sumita Jain, Ana Mirela Neculai, Patrick Yip, Howard Robinson, John C Whitney, Laura Riley, Lori L Burrows, Dennis E Ohman, and P Lynne Howell. AlgK is a TPR-containing protein and the periplasmic component of a novel exopolysaccharide secretin. *Structure*, 18(2):265–73, Feb 2010.

[72] Hing C Wong, Anna L Fear, Roger D Calhoon, Gregory H Eichinger, Raphael Mayer, Dorit Amikam, Morshe Benziman, David H Gelfand, James H Meade, and Anne W Emerick. Genetic organization of the cellulose synthase operon in Acetobacter xylinum. *Proceedings of the National Academy of Sciences*, 87(20):8130–8134, 1990.

[73] I M Saxena, K Kudlicka, K Okuda, and R M Brown, Jr. Characterization of genes in the cellulose-synthesizing operon (acs operon) of Acetobacter xylinum: implications for cellulose crystallization. *J Bacteriol*, 176(18):5735–52, Sep 1994.

[74] Prashanti R Iyer, Jeffrey Catchmark, Nicole R Brown, and Ming Tien. Biochemical localization of a protein involved in synthesis of Gluconacetobacter hansenii cellulose. *Cellulose*, 18(3):739–747, 2011.

[75] R Standal, T G Iversen, D H Coucheron, E Fjaervik, J M Blatny, and S Valla. A new gene required for cellulose production and a gene encoding cellulolytic activity in Acetobacter xylinum are colocalized with the bcs operon. *J Bacteriol*, 176(3):665–72, Feb 1994.

[76] Olga Mazur and Jochen Zimmer. Apo- and cellopentaose-bound structures of the bacterial cellulose synthase subunit BcsZ. *J Biol Chem*, 286(20):17601–6, May 2011.

[77] E D Korn. Biochemistry of actomyosin-dependent cell motility (a review). *Proc Natl Acad Sci U S A*, 75(2):588–99, Feb 1978.

[78] T J Mitchison and L P Cramer. Actin-based cell motility and cell locomotion. *Cell*, 84(3):371–9, Feb 1996.

[79] Song Li, Jun-Lin Guan, and Shu Chien. Biochemistry and biomechanics of cell motility. *Annu Rev Biomed Eng*, 7:105–50, 2005.

[80] Stephanie I Fraley, Yunfeng Feng, Ranjini Krishnamurthy, Dong-Hwee Kim, Alfredo Celedon, Gregory D Longmore, and Denis Wirtz. A distinctive role for focal adhesion proteins in three-dimensional cell motility. *Nat Cell Biol*, 12(6):598–604, Jun 2010.

[81] Gwendolen C Reilly and Adam J Engler. Intrinsic extracellular matrix properties regulate stem cell differentiation. *J Biomech*, 43(1):55–62, Jan 2010.

[82] Evelyn K F Yim and Michael P Sheetz. Force-dependent cell signaling in stem cell differentiation. *Stem Cell Res Ther*, 3(5):41, Oct 2012.

[83] M Liu, A K Tanswell, and M Post. Mechanical force-induced signal transduction in lung cells. *Am J Physiol*, 277(4 Pt 1):L667–83, Oct 1999.

[84] Sungsoo Na, Olivier Collin, Farhan Chowdhury, Bernard Tay, Mingxing Ouyang, Yingxiao Wang, and Ning Wang. Rapid signal transduction in living cells is a unique feature of mechanotransduction. *Proceedings of the National Academy of Sciences*, 105(18):6626–6631, 2008.

[85] Sun Taek Kim, Koh Takeuchi, Zhen-Yu J Sun, Maki Touma, Carlos E Castro, Amr Fahmy, Matthew J Lang, Gerhard Wagner, and Ellis L Reinherz. The $\alpha\beta$ T cell receptor is an anisotropic mechanosensor. *J Biol Chem*, 284(45):31028–37, Nov 2009.

[86] Dennis E Discher, Paul Janmey, and Yu-Li Wang. Tissue cells feel and respond to the stiffness of their substrate. *Science*, 310(5751):1139–43, Nov 2005.

[87] F Guharay and F Sachs. Stretch-activated single ion channel currents in tissue-cultured embryonic chick skeletal muscle. *J Physiol*, 352:685–701, Jul 1984.

[88] N Q Balaban, U S Schwarz, D Riveline, P Goichberg, G Tzur, I Sabanay, D Mahalu, S Safran, A Bershadsky, L Addadi, and B Geiger. Force and focal adhesion assembly: a close relationship studied using elastic micropatterned substrates. *Nat Cell Biol*, 3(5):466–72, May 2001.

[89] Ning Wang, Jessica D Tytell, and Donald E Ingber. Mechanotransduction at a distance: mechanically coupling the extracellular matrix with the nucleus. *Nature Reviews Molecular cell biology*, 10(1):75–82, 2009.

[90] Peter Meinke and Eric C Schirmer. LINC'ing form and function at the nuclear envelope. *FEBS Lett*, 589(19 Pt A):2514–21, Sep 2015.

[91] K. Wilhelmsen, S. H. Litjens, I. Kuikman, N. Tshimbalanga, H. Janssen, I. van den Bout, K. Raymond, and A. Sonnenberg. Nesprin-3, a novel outer nuclear membrane protein, associates with the cytoskeletal linker protein plectin. *J Cell Biol*, 171(5):799–810, 2005.

[92] F. Autore, M. Pfuhl, X. Quan, A. Williams, R. G. Roberts, C. M. Shanahan, and F. Fraternali. Large-scale modelling of the divergent spectrin repeats in nesprins: giant modular proteins. *PLoS One*, 8(5):e63633, 2013.

[93] V. C. Padmakumar, S. Abraham, S. Braune, A. A. Noegel, B. Tunggal, I. Karakesisoglou, and E. Korenbaum. Enaptin, a giant actin-binding protein, is an element of the nuclear membrane and the actin cytoskeleton. *Exp Cell Res*, 295(2):330–9, 2004.

[94] D. Rajgor and C. M. Shanahan. Nesprins: from the nuclear envelope and beyond. *Expert Rev Mol Med*, 15:e5, 2013.

[95] K. J. Roux, M. L. Crisp, Q. Liu, D. Kim, S. Kozlov, C. L. Stewart, and B. Burke. Nesprin 4 is an outer nuclear membrane protein that can induce kinesin-mediated cell polarization. *Proc Natl Acad Sci U S A*, 106(7):2194–9, 2009.

[96] Y. Y. Zhen, T. Libotte, M. Munck, A. A. Noegel, and E. Korenbaum. NUANCE, a giant protein connecting the nucleus and actin cytoskeleton. *J Cell Sci*, 115(Pt 15):3207–22, 2002.

[97] Shimon Weiss. Fluorescence spectroscopy of single biomolecules. *Science*, 283(5408):1676–1683, 1999.

[98] WE Moerner and David P Fromm. Methods of single-molecule fluorescence spectroscopy and microscopy. *Review of Scientific instruments*, 74(8):3597–3619, 2003.

[99] L Stirling Churchman, Zeynep Ökten, Ronald S Rock, John F Dawson, and James A Spudich. Single molecule high-resolution colocalization of Cy3 and Cy5 attached to macromolecules measures intramolecular distances through time. *Proceedings of the National Academy of Sciences of the United States of America*, 102(5):1419–1423, 2005.

[100] Ahmet Yildiz, Joseph N Forkey, Sean A McKinney, Taekjip Ha, Yale E Goldman, and Paul R Selvin. Myosin V walks hand-over-hand: single fluorophore imaging with 1.5-nm localization. *Science*, 300(5628):2061–5, Jun 2003.

[101] Michael J Rust, Mark Bates, and Xiaowei Zhuang. Sub-diffraction-limit imaging by stochastic optical reconstruction microscopy (STORM). *Nature methods*, 3(10):793–796, 2006.

[102] Bi-Chang Chen, Wesley R Legant, Kai Wang, Lin Shao, Daniel E Milkie, Michael W Davidson, Chris Janetopoulos, Xufeng S Wu, John A Hammer, 3rd, Zhe Liu, Brian P English, Yuko Mimori-Kiyosue, Daniel P Romero, Alex T Ritter, Jennifer Lippincott-Schwartz, Lillian Fritz-Laylin, R Dyche Mullins, Diana M Mitchell,

Joshua N Bembenek, Anne-Cecile Reymann, Ralph Böhme, Stephan W Grill, Jennifer T Wang, Geraldine Seydoux, U Serdar Tulu, Daniel P Kiehart, and Eric Betzig. Lattice light-sheet microscopy: imaging molecules to embryos at high spatiotemporal resolution. *Science*, 346(6208):1257998, Oct 2014.

[103] Liang Gao, Lin Shao, Bi-Chang Chen, and Eric Betzig. 3D live fluorescence imaging of cellular dynamics using bessel beam plane illumination microscopy. *Nature protocols*, 9(5):1083–1101, 2014.

[104] Keir C Neuman and Attila Nagy. Single-molecule force spectroscopy: optical tweezers, magnetic tweezers and atomic force microscopy. *Nat Methods*, 5(6):491–505, Jun 2008.

[105] Juan Carlos Cordova, Dibyendu Kumar Das, Harris W Manning, and Matthew J Lang. Combining single-molecule manipulation and single-molecule detection. *Curr Opin Struct Biol*, 28:142–8, Oct 2014.

[106] Keir C Neuman and Steven M Block. Optical trapping. *Rev Sci Instrum*, 75(9):2787–809, Sep 2004.

[107] Arthur Ashkin. Acceleration and trapping of particles by radiation pressure. *Physical review letters*, 24(4):156, 1970.

[108] Arthur Ashkin and JM Dziedzic. Optical levitation by radiation pressure. *Applied Physics Letters*, 19(8):283–285, 1971.

[109] Arthur Ashkin, JM Dziedzic, JE Bjorkholm, and Steven Chu. Observation of a single-beam gradient force optical trap for dielectric particles. *Optics letters*, 11(5):288–290, 1986.

[110] I.A. Vorobjev, H. Liang, W.H. Wright, and M.W. Berns. Optical trapping for chro-

mosome manipulation: a wavelength dependence of induced chromosome bridges. *Biophysical Journal*, 64(2):533 – 538, 1993.

[111] H. Liang, K.T. Vu, P. Krishnan, T.C. Trang, D. Shin, S. Kimel, and M.W. Berns. Wavelength dependence of cell cloning efficiency after optical trapping. *Biophysical Journal*, 70(3):1529 – 1533, 1996.

[112] Keir C. Neuman, Edmund H. Chadd, Grace F. Liou, Keren Bergman, and Steven M. Block. Characterization of photodamage to Escherichia coli in optical traps. *Biophysical Journal*, 77(5):2856 – 2863, 1999.

[113] Matthew J Lang, Charles L Asbury, Joshua W Shaevitz, and Steven M Block. An automated two-dimensional optical force clamp for single molecule studies. *Biophys J*, 83(1):491–501, Jul 2002.

[114] Thomas T Perkins. Optical traps for single molecule biophysics: a primer. *Laser & Photonics Reviews*, 3(1-2):203–220, 2009.

[115] Elio A Abbondanzieri, William J Greenleaf, Joshua W Shaevitz, Robert Landick, and Steven M Block. Direct observation of base-pair stepping by RNA polymerase. *Nature*, 438(7067):460–465, 2005.

Chapter 2

CELLOBIOHYDROLASE 1 FROM *TRICHODERMA REESEI* DEGRADES CELLULOSE IN SINGLE CELLOBIOSE STEPS

*This chapter is adapted from Brady et al, "Cellobiohydrolase 1 from Trichoderma reesei degrades cellulose in single cellobiose steps" Nature Communications, 6:10140 (2015) by permission granted under the Nature Publishing Group (NPG) license policy.

2.1 Summary

Cellobiohydrolase 1 from *Trichoderma reesei* (*Tr*Cel7A) processively hydrolyzes cellulose into cellobiose. While enzymatic techniques have been established as promising tools in biofuel production, a clear understanding of the motor's mechanistic action has yet to be revealed. We developed an optical tweezers based single molecule (SM) motility assay for precision tracking of *Tr*Cel7A. Direct observation of motility during degradation reveals processive runs and distinct steps on the scale of 1 nm. Our studies suggest *Tr*Cel7A is not mechanically limited, can work against 20 pN loads and speeds up when assisted. Temperature dependent kinetic studies establish the energy requirements for the fundamental stepping cycle which likely includes energy from glycosidic bonds and other sources. Through SM measurements of isolated *Tr*Cel7A domains, we determine that the catalytic domain alone is sufficient for processive motion, providing insight into *Tr*Cel7A's molecular motility mechanism

2.2 Introduction

Cellulose, the most abundant polymer on Earth [1, 2] is highly resistant to hydrolysis, and is degraded by a number of enzymes referred to as cellulases. Cellulases are used in many industries including food processing, pulp and paper, and most recently, the biofuel

industry, as a feedstock derived sugar source for conversion to ethanol. Cellulose is also a major component of biofilm mats such as those in aquatic environments, pipe fouling, and dental plaques [3, 4, 5]. Despite the remarkably diverse uses of cellulose based products, its structural stability often leads to disposal as waste in biofuel production processes and problems due to its role in biofilm and bacterial mat stability.

The decomposition of cellulose into basic sugar components, cellobiose and glucose, is a bottleneck in cellulosic biofuel production [6, 7]. The most common and effective industrial cellulose degradation processes include heat, mechanical and acid treatment. However, enzymatic degradation has become an attractive alternative due to its more environmentally benign nature [8, 9]. Enzymatic processing allows for lower operating temperatures, leading to greater net energy production, milder processing conditions, and minimized wear on processing units. Unfortunately, enzymes are expensive and slow. A better understanding of cellulase mechanisms could lead to decreased enzyme costs and improved economics of industrial production plants.

Enzymatic cellulose degradation occurs naturally through a system of cellulases such as those secreted by the fungus *Trichoderma reesei*. Here a mixture of cellulases serve specialized roles in cellulose and oligosaccharide hydrolysis. Cellobiohydrolase 1 from *Trichoderma reesei* (*Tr*Cel7A), representing 60% of the enzyme cocktail population, is the primary exocellulase and degrades cellulose into cellobiose [10]. Exocellulases act on crystalline regions of cellulose fibers, tend to be processive, are directionally dependent, and are thought to be powered, in part, by the energy from hydrolysis of the glycosidic bond [11]. *Tr*Cel7A has three major parts: a small carbohydrate-binding module (CBM), a larger catalytic domain (CD) and a short, 27 aa linker domain (LD) connecting the two (Fig. 2.1a).

Prior work using high speed atomic force microscopy (HS-AFM) tracked the motility of low concentrations of *Tr*Cel7A motors on highly crystalline ($>$80%) *Cladophora* derived cellulose [12] showing *Tr*Cel7A translocation with an average apparent velocity of 5.3 $\pm$

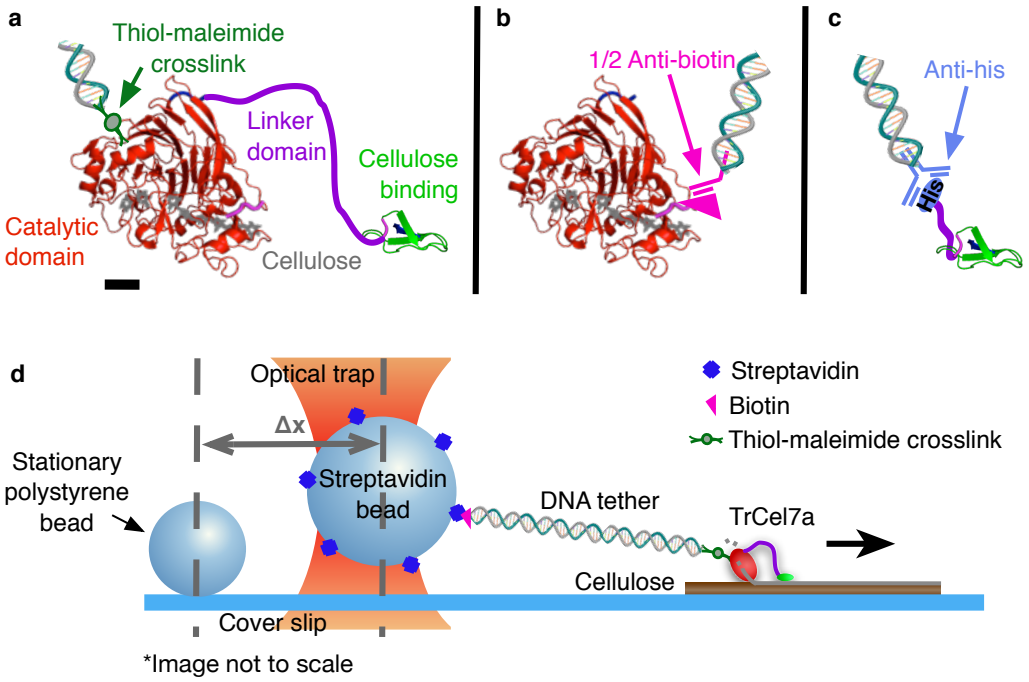

Figure 2.1: **Constructs and assay schematic.** Construct details and optical trap assay schematic for (a) wt*Tr*Cel7A ,where a DNA-bound sulfo-SMCC crosslinks through available surface lysines (scale bar, 1 nm), (b) isolated biotin-labelled CD ligated to DNA through a 1/2 anti-biotin antibody and (c) isolated CBM tethered through a DNA-bound anti-His antibody. Structures in (a)-(c) are from PDB -7Cel and 2CBH. (d) A schematic of the wt*Tr*Cel7A motility assay tracks motility through a 1,010-bp tether attached to a 1.25-μm streptavidin bead held in an optical trap. Stationary fiducial beads serve to compensate for drift.

4.9 nm s^{-1} at 25 °C [7, 13]. Records from Igarashi *et al.* [7] showed global pause and run states spanning up to 70 nm and observed a 'traffic jam' tendency of cellulases to bunch up along the track. Single molecule (SM) fluorescence studies revealed unloaded on and off rates, observing non-productive dwells as well as longer associations [13, 14, 15].

Here, we designed a SM motility assay based on optical tweezers (Fig. 2.1d) for precision tracking of individual wild-type *Tr*Cel7A (wt*Tr*Cel7A) and isolated CD (Fig. 2.1b) on, primarily, filter paper derived cellulose (∼68% crystalline) [16], with nanometer resolution under load. Studies reveal translocation in single cellobiose steps with velocity and stepping behavior almost identical for both constructs, indicating that the CD is independently responsible for translocation (and hydrolysis). Binding studies of isolated CBM (Fig. 2.1c)

reveal that the presence of CBM may sometimes even hinder translocation, a small price to pay given the decreased binding of the motor when the CBM is removed, as noted in our activity studies. Additional experiments probing *Tr*Cel7A motility at elevated temperatures also provide insight into the energetic barriers of the motility cycle.

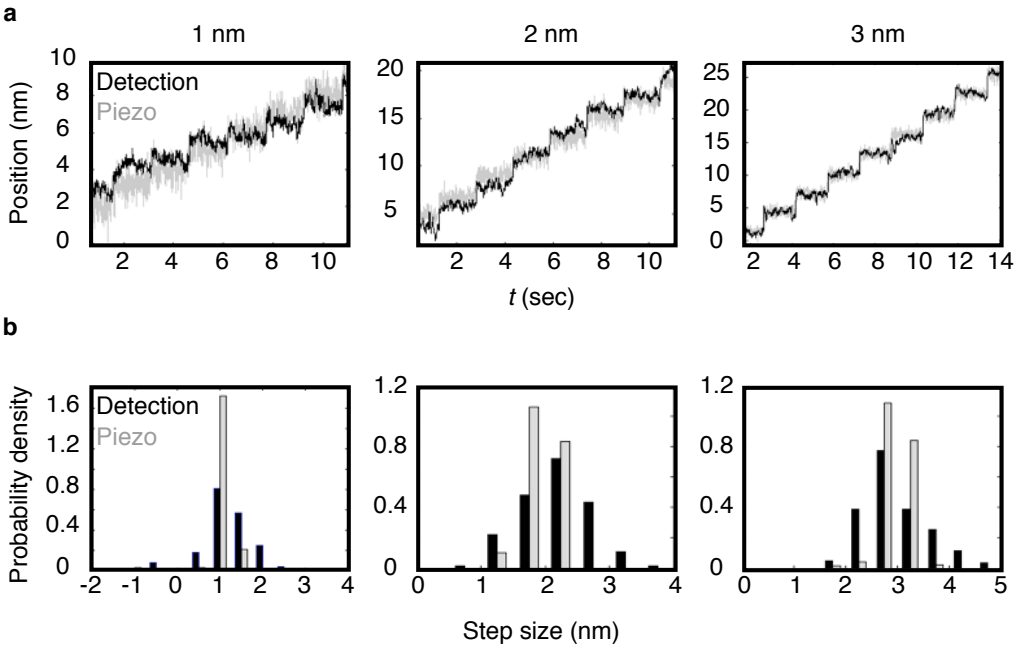

Figure 2.2: **Spatial resolution controls.** a) Sample traces of step controls showing both the movement of the piezo stage (grey) and the associated position of an immobilized bead by the detection laser (black). b) Histograms of the step sizes detected by our step-finding algorithm for both the piezo stage (grey) and detection laser data (black). This data is shown for nominal step sizes of 1 nm (N=40), 2 nm (N=75), and 3 nm (N=15) from left to right with resulting average observed step sizes (piezo / detection) of 1.15 nm/1.00 nm, 2.19 nm/1.93 nm, and 2.97 nm/2.95 nm, respectively.

A spatial resolution of 1 nm was determined through a number of controls using artificial motion enabled through actuating a piezo stage with surface bound beads. Here we instructed the stage to step by 1 and 2 nm intervals at an average rate consistent with our observed dwell times with one step taken every 1-3 seconds. These steps were readily re-created with our analysis programs (Fig. 2.2), indicating a step resolution of at least 1 nm.

2.3 Results

2.3.1 Optical trapping assay overview

Our primary motility assay consists of full motors, wt*Tr*Cel7A, that are purified from a mixture of *T. reesei* cellulases (Sigma) using ion-exchange chromatography [17]. Motors are biotinylated, via a 1010 bp DNA tether, and attached to a 1.25 μm streptavidin coated polystyrene bead. Beads were trapped and placed on cellulose fibers, derived from filter paper, that are affixed to a cover glass surface. Smaller 0.75 μm beads, serving as fiducial markers for position to compensate for drift, were also affixed to the cover glass (Fig. 2.1d).

To ensure the validity of our drift adjustment method, data was collected following the same translocation tracking procedure as described for wt*Tr*Cel7A except a fixed, non-functionalized 1.25 μm bead adhered to the surface was tracked rather than an enzyme functionalized bead. The relative position of the larger bead was then compared to the position of a video tracked fiducial bead (0.75 μm). Once the control bead position was adjusted for drift, it was found that 85-95% of the drift was removed from the analyzed control traces. All residual influence from drift resulted in velocities at least an order of magnitude lower than the observed average velocity of wt*Tr*Cel7A.

2.3.2 Motility characterization of wt*Tr*Cel7A

Motility of wt*Tr*Cel7A on filter paper substrate was processive with an average weighted velocity (time basis) of 0.25 nm s^{-1} $\pm$ 0.16 (s.d.) obtained from a total of N=180 traces from 64 separate enzymes at 21°C. The velocity distribution ranges from slow to fast runs spanning 0.1 nm s^{-1} to 0.8 nm s^{-1} (Fig. 2.3a). Most traces were 30-60 nm in length with a few as long as 150 nm. A smaller study was also carried out on *Cladophora* derived native cellulose I (N=68 from 17 enzymes). In this study, an average weighted velocity, based on trace length (time basis) of 0.25 nm s^{-1} $\pm$ 0.35 (s.d.) was observed with velocities 0.05 up to 2.5 nm s^{-1} (Fig. 2.3b). Motility trajectories on both substrates were gener-

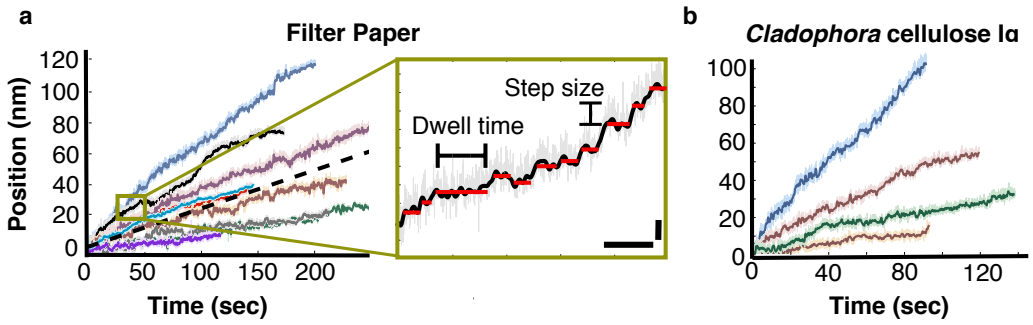

Figure 2.3: **Motility traces and stepping definitions.** (a) Sample wt*Tr*Cel7A motility traces on filter paper exhibit a range of velocities with an average of 0.25 nm s^{-1} $\pm$ 0.16 (s.d.) dashed line. The average is representative of 180 traces from 64 separate enzymes at 21 °C. The inset reveals an enlarged region of one trace highlighting the fine stepping motion of wt*Tr*Cel7A. Scale bars are 5 s and 2 nm, respectively. (b) Sample *Tr*Cel7A motility traces on *Cladophora*-derived cellulose. The average velocity is 0.25 nm s^{-1} $\pm$ 0.35 (s.d.) and is representative of 68 traces from 17 separate enzymes at 21 °C.

ally straight and some contained pauses. Traces terminated by reaching the end of our 10 minute measurement window, exiting our detector zone, stalls, or by unbinding. A closer look at the motility on filter paper revealed steps with a fundamental size of 1.3 nm. Step and dwell distributions were extracted through a step-finding algorithm described in the Methods. Gaussian fits captured the overall step size distribution when multiples of 1x and 2x the fundamental step size were included for both positive and negative steps (Fig. 2.4a). Positive and negative fractions represented 68% and 32% of the population, respectively. Distributions of dwell times between steps averaged 1.6 s $\pm$ 0.05 (s.e.m.), yet persistent dwells as long as 10 seconds were observed. A double exponential fit to the dwell time distribution resulted in time constants of 1.9 s (86%) and 0.5 s (14%) (Fig. 2.4b).

The relationship between step size and dwell time revealed that positive steps were associated with slightly longer dwells than negative steps (Fig. 2.4c). Particularly straight and fast traces yielded step distributions generally lacking negative steps (Fig. 2.4d-e).

Our measurements included loads generally assisting and opposing motility. Opposing loads (negative axial force) do not appear to significantly affect velocity for loads up to 20 pN, suggesting a stall force greater than 20 pN. The velocity is calculated as the slope of a

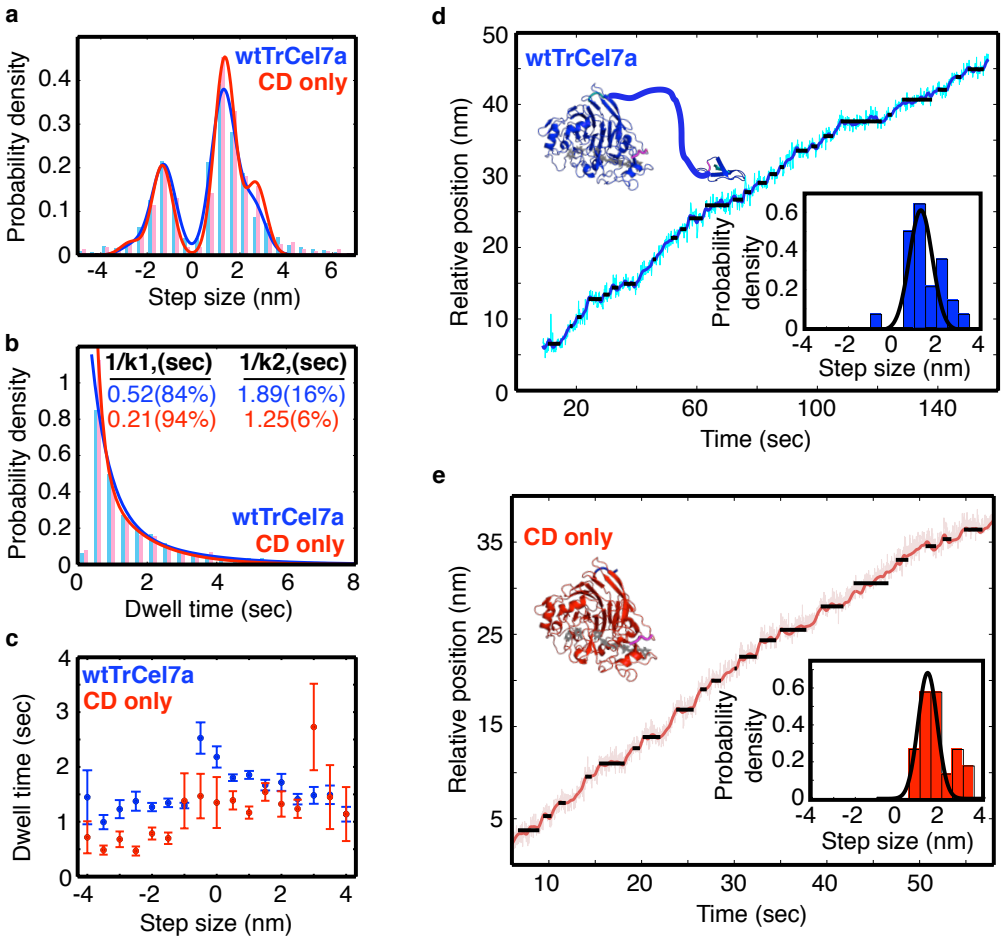

Figure 2.4: **Stepping analysis of wt*Tr*Cel7A (blue) and isolated CD (red).** (a) Step size distributions fit to Gaussian curves based on the fundamental and 2x fundamental steps (wt*Tr*Cel7A: 1.28 $\pm$ 0.7 nm (s.d.), N=1614; isolated CD: 1.34 $\pm$ 0.6 nm (s.d.), N=360). (b) Dwell distributions fit to a double exponential with exponential time constants, 1/k1 and 1/k2, indicated in the figure. The mean dwell time of wt*Tr*Cel7A (N=1628) and isolated CD (N=369) are 1.6 and 1.2 s, respectively. (c) The relationship between step size and dwell time shows generally shorter dwell times associated with negative steps and isolated CD measurements (red). Error bars denote s.e.m. (d) and (e) provide sample traces with individual trace step distributions (insets) with similar behavior between the wt*Tr*Cel7A and isolated CD constructs.

time trace over a five second window and is calculated at each point along a trace. Although a handful of traces appeared to have a stall profile, a formal stall force was not determined as the opposing force velocity profile remained relatively flat. Assisting loads indicate an apparent increase in translocation velocities, nearly doubling for forces approaching 25 pN (Fig. 2.5a). Note that lines included in Fig. 2.5a simply highlight the general trend

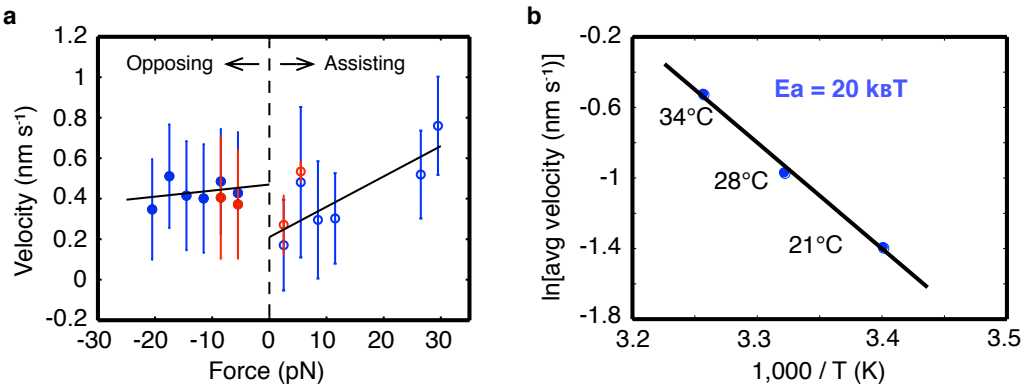

Figure 2.5: **Force and temperature dependence of velocity.** (a) The force velocity relationship for wt*Tr*Cel7A. Opposing loads (negative) appear to have little effect up to 20 pN while assisting loads (positive) increase velocity. Full data set (blue, N=15666 opposing and N=5939 assisting) and an axial trace subset (red, N=5855 opposing and N=208 assisting), in which the force vector is within 18.5° of the cellulose axis. Error bars represent standard deviation (s.d.). (b) An Arrhenius fit of wt*Tr*Cel7A motility data from 21 to 34 °C using average velocity (cellobiose units per s) as a rate and yielding an activation energy of 20 k_BT (49.8 kJ mol^{-1}). The averages are found from N=76 (21 °C), N=47 (28 °C), N=52 (34 °C).

of the force velocity data and not necessarily the precise shape of the relationship. The velocity increase is due to a 0.2 second decrease in dwell time, where apparent long dwells are reduced (Fig. 2.6a). A moderate increase in larger steps is also observed, although it should be noted that the fundamental step size as well as the percent of negative steps remains unchanged. Further visualization of these results can be found in Fig. 2.6b-d.

2.3.3 Motility characterization of isolated CD

To separate the function and behavior of the CD and CBM from the behavior of the full enzyme, we expressed isolated CD as well as isolated CBM with a partial linker. In the case of isolated CD, a biotin tag on the N-terminal served as a handle for tethering the domain to the bead in a similar assay geometry to the full enzyme (Fig. 2.1b), while an N-terminal His-tag was used in the case of isolated CBM (Fig. 2.1c). Strikingly, motility measurements with isolated CD revealed almost identical stepping and processive motion

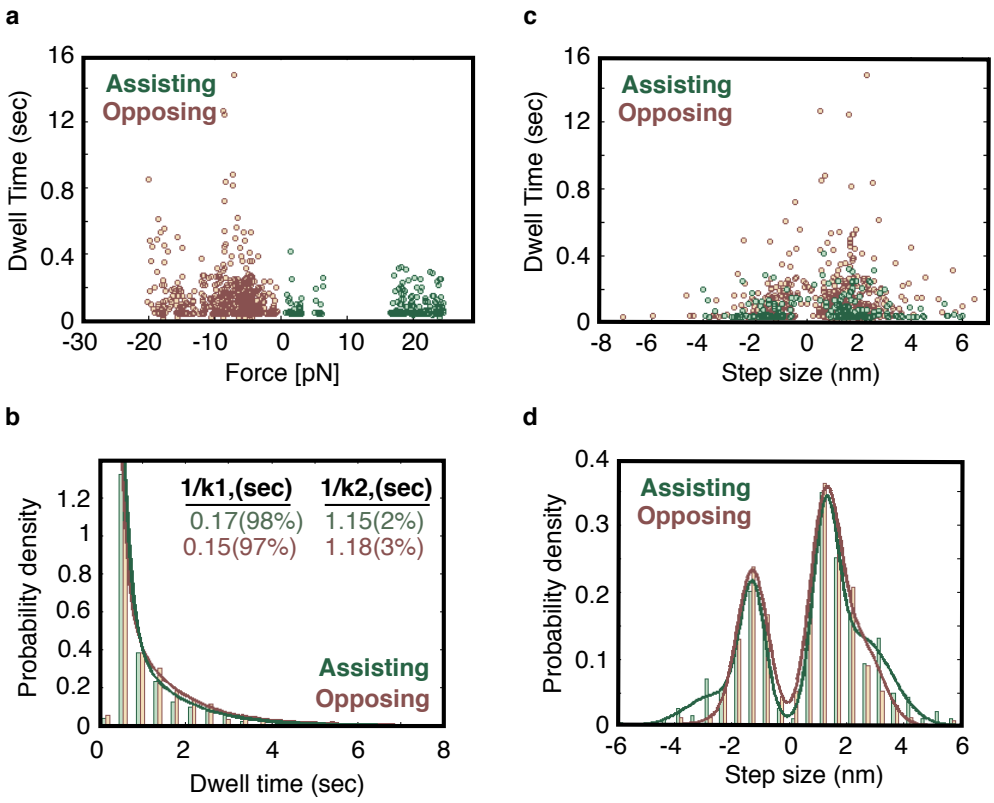

Figure 2.6: **Stepping analysis of opposing (brown) and assisting (green) traces of wt*Tr*Cel7A.** (a) The relationship between dwell time vs. force for different load types. Note the reduction of long dwells for assisting load motility. (b) Dwell distributions fit to a double exponential with the fit values indicated in the figure. (c) The relationship between dwell time vs. step size. (d) Step size distributions fit to the sum of Gaussian curves based on the fundamental and 2x fundamental forward and rearward steps yield a fundamental step size of 1.3 nm.

as the full enzyme (Fig. 2.4a,e). Slightly shorter dwell times (1.2 seconds) are most notable when associated with negative steps (Fig. 2.4b-c). In addition, a double exponential fit of the dwell time distribution shows a shift to a higher preference for the faster step (1/k1=0.21 s (94%) and 1/k2=1.25 s (6%) for isolated CD). This suggests the CD is fully and independently capable of translocation mimicking the full enzyme.

2.3.4 Activity measurements of wt*Tr*Cel7A and isolated CD

While SM behavior is unchanged, it is noted that bulk activity assays were challenging and required implementation of multiple approaches. These assays, specifically mass spectrometry analysis of cellobiose product and fluorescence decoration of fibers, indicate an apparent reduction of activity in CD that is 50 times lower than wt*Tr*Cel7A, almost exclusively due to the absence of the CBM. The standard Filter Paper Assay was also used to measure activity but the detection limit was insufficient to measure the activity of isolated CD. All three activity assays are described in more detail below.

Mass spectrometry of CD and wt*Tr*Cel7A activity: CD samples were positive for cellobiose with a sample concentration of 15.6 μM and corresponding undiluted concentration of 260 μM (0.09 mg mL^{-1}) (Fig. 2.7). Similarly, wt*Tr*Cel7A shows a sample concentration of 50.86 μM and undiluted concentration of 15.26 mM (5.22 mg mL^{-1}). Filter paper controls show low response below the detection limit with an undiluted concentration estimated to be below 1.5 μM. Our standards reveal a detection limit of cellobiose near 1 μM while maintaining a signal to noise ratio of 10:1. These results indicate that wt*Tr*Cel7A has an apparent activity approximately 58.7 times higher than that of isolated CD. As supported in the following fiber decoration method, this difference is thought to be almost entirely due to a decrease in binding as a result of a lack of CBM and not a result of misfolded or enzymatically inactive motor.

Fluorescence decoration of fibers: Both CD and wt*Tr*Cel7A enzyme specifically bound to the cellulose fibers. However, in order to observe CD binding at similar intensity to that of wt*Tr*Cel7A at 125 pM, the required CD concentration was elevated 50x to 6 nM (Fig. 2.8). This result is consistent with reports by Igarashi et al [6], which state that at least 10x more CD than *Tr*Cel7A was required to observe binding using AFM. Decoration studies suggest that isolated CD is competent to bind fibers but with lower apparent activity, due to an inability to commit to cellulose binding in the absence of the CBM. This level of apparent activity reduction is consistent with that seen in mass spectrometry indicating that

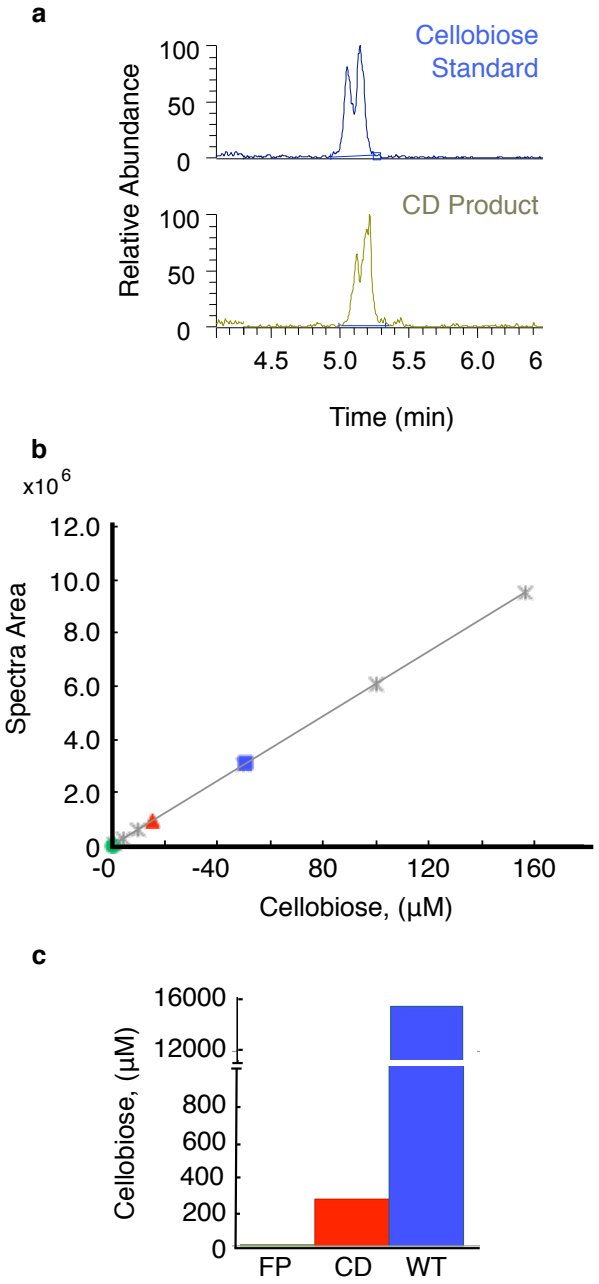

Figure 2.7: **Mass spectrometry activity results.** (a) The spectra show a 1 μM cellobiose standard (Sigma - C7252) peak (top - blue) for comparison to the peak obtained from CD product (bottom - green) demonstrating that enzymatic product is consistent with that of cellobiose. (b) Cellobiose calibration curve (grey "x") and diluted sample product concentration including filter paper control (green circle), CD product (red triangle), and wt*Tr*Cel7A (blue square). (c) A comparison of undiluted enzymatic product from the filter paper control (FP), CD, and wt*Tr*Cel7A (WT).

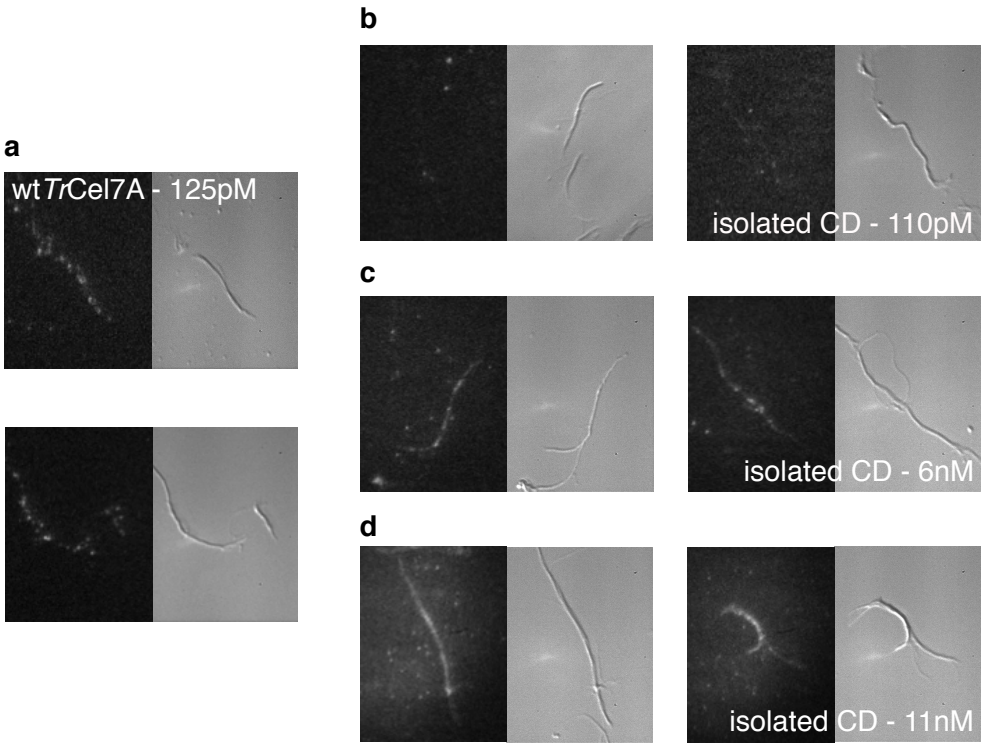

Figure 2.8: **Fluorescently labelled protein specifically binds substrate.** Fluorescent images and the corresponding bright field (DIC) images show specific binding of TAMRA(5)-se labelled protein to surface bound fibers. The degree of decoration can be compared between two representative pairs of each condition for (a) wt*Tr*Cel7A at 125 pM, (b) CD at 110 pM, (c) CD at 6 nM, and (d) CD at 11 nm. Similar decoration of 125 pM wt*Tr*Cel7A (a) is achieved for 6 nM CD (c) which is approximately 50x more concentrated that wt*Tr*Cel7A.

nearly all CD that binds is also enzymatically active. Thus, *E. coli* is capable of successful heterologous expression of active CD.

Filter paper assay (FPA): Using 1 mg mL^{-1} [15 μM] concentrations of wt*Tr*Cel7A and succinimidyl ester modified wt*Tr*Cel7A (wt*Tr*Cel7A*), cellobiose productions of 3.35 and 4.2 mg mL^{-1}, respectively, were seen for an incubation with filter paper substrate of 50 hours at room temperature (Fig. 2.9). The results show that succinimidyl modification of the free lysines on the enzyme during bead preparation does not negatively affect activity. For isolated CD at 1 mg mL^{-1} [22 μM], the DNS assay did not reveal detectable activity. The detection limit is approximately 0.4 mg mL^{-1} cellobiose which is greater than the

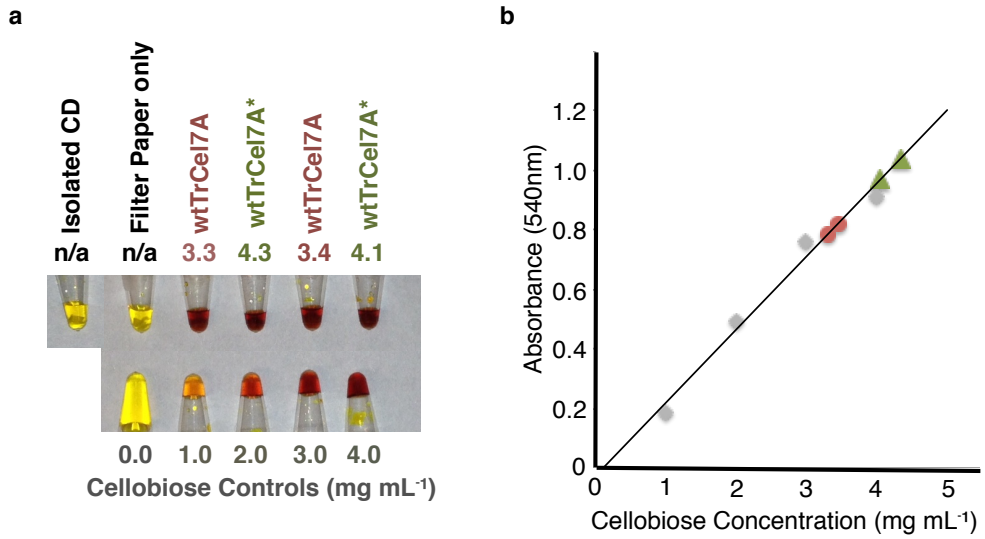

Figure 2.9: **Filter paper assay (FPA).** Filter paper assay using DNS to visualize reducing sugar (cellobiose) product generated over 50 hours at room temperature. (A) Visual confirmation of activity by wt*Tr*Cel7A, both with (wt*Tr*Cel7A*) and without (wt*Tr*Cel7A) succinimidyl ester modification and a lack of detectable activity by isolated CD and a filter paper negative control. (B) Analysis of activity measured at 540 nm shows high activity of both wt*Tr*Cel7A (red circles) and wt*Tr*Cel7A* (green triangles) with slightly elevated activity for wt*Tr*Cel7A*.

expected 0.07 mg mL^{-1} given a 50x reduction in apparent activity for CD.

Heterologous expression of CD in *E. coli*, which can produce misfolded or inactive proteins [18], and the lack of pyroglutamic acid [19] at the N-terminus of the CD, due to the biotin carboxyl carrier protein (BCCP) tag, may contribute to this lack of apparent activity. However, mass spectrometry results show the expression of active enzyme (CD) in *E. coli*, and fluorescent binding studies suggest that the observed decrease in apparent activity for CD is almost exclusively due to a lack of binding facilitated through the CBM. Note that we detect no difference in the motility traces so any effects from a lack of pyroglutamic acid are likely to occur upstream during motility commitment. Rather, we believe the large differences observed in activity here are due to the lack of CBM, which increases the local concentration of CD near the substrate and the motor's commitment to degradation. CBM binding function is rescued in our CD experiments when the bead is actively brought near

the surface to bind. It is conceivable that the lack of the CBM could allow for large differences in apparent activity at the bulk scale while processive motility remains unchanged as observed at the single molecule level. This type of discrepancy is seen in other motor systems such as ClpXP in which a 4 fold difference in commitment to degradation is observed when comparing bulk solution to single molecule results [20]. Additionally, any concern regarding the analysis of inactive motor is eliminated in single molecule experiments where only motility from active motors is recorded. Our observations are supported by Igarashi [6] and Nidetzky [21] who report similar activities of absorbed *Tr*Cel7A and *Tr*Cel7A core (CD) while also noting, in the case of Igarashi et al, that at least a 10x higher concentration of CD is needed to observe binding.

2.3.5 CBM binding studies

Loaded single molecule measurements on tethers formed directly through isolated CBM domain binding revealed no motility and an average bond lifetime of 1.7 s $\pm$ 0.27 (s.e.m.), which is consistent with the non-productive off rate reported by Shibafuji [13]. This average represents lifetimes at a range of forces, with an average (and median) force of 7.1 (and 5.2) pN $\pm$ 0.95 (s.e.m.). Solution based binding through Biacore on substrate and motors identically prepared to those used here reveals an off rate of 0.32 s^{-1}, corresponding to a bond lifetime of 3.1 seconds, slightly longer than the SM dwell time. A CBM activity assay (detailed in the Methods) reveals over 50% of our expressed CBM exhibit high affinity for cellulose.

2.3.6 Temperature dependence of wt*Tr*Cel7A

While the described studies were carried out at 21°C, *Tr*Cel7A performance is optimized near 50°C [22]. A temperature of 50°C was not used due to instrument limitations, however, we did track wt*Tr*Cel7A at temperatures from 20 to 34°C. Measurements at elevated temperatures can reveal activation barriers to mechanical cycle [23, 24]. As ex-

pected, the velocity of wt*Tr*Cel7A increases with an elevating temperature (0.25, 0.4, and 0.6 nms^{-1} at 21, 28, and 34°C, respectively) (Fig. 2.5b). Step sizes remain constant while dwell times are reduced (1.6, 1.4, and 1.2 seconds, respectively). Here we used an assay with the motor bound directly to the bead (no DNA tether) due to increased noise at elevated temperatures. To ensure consistency between this assay and the DNA tethered assay at 21°C, the temperature dependent results were compared to a smaller study incorporating the DNA tether in which the temperature was only elevated to 28°C. The observed rates are consistent within error.

2.4 Discussion

This optical tweezers based motility assay permits direct monitoring of *Tr*Cel7A motion revealing steps, dwell times and energetic barriers associated with cellulose degradation. The 1.3 nm fundamental step size identified here suggests the motility cycle is tied to processing of a single cellobiose unit (1 nm). Although we believe a single step underlies the dominant preferred cycle, *Tr*Cel7A is also able to step in multiples of this unit, move backwards and pause. Backstepping and pausing, common in other motors [25, 26, 27, 28, 29], may allow *Tr*Cel7A to negotiate roadblocks, including those created by its own CBM and linker domains, and re-set motility.

Our study reveals processivity of isolated *Tr*Cel7A motors is at least 50 steps (50 nm). Here we conservatively analyzed our traces, only considering segments with no obvious interruption in motility. Our processivity results, in which *Tr*Cel7A stays bound for 1.5 minutes or longer, are consistent with 'productive binding' dwell times reported earlier [14, 15]. Given the relative insensitivity of wt*Tr*Cel7A to load, these results suggest the CD domain is sufficient for maintaining a tight grip during active motility.

Our temperature study yields an activation barrier of 20 k_BT (49.8 kJ mol^{-1}) to stepping. This assumes a velocity in which one catalytic event is equal to one cellobiose unit ($\sim$1 nm step). Thus, the velocity is treated as a rate without a unit length correc-

tion (Fig. 2.5b). This result is similar to the rate-limiting barrier of 15.5 kcal mol^{-1} (60 kJ mol^{-1}) found by Knott and coworkers in their 2014 computational study [30]. From a thermodynamic analysis of the cellulose degradation process, a mere quarter of this activation energy is available from the glycosidic bond, 5 k_BT, or 12.5 kJ mol^{-1} [6, 31]. Crystalline cellulose contains hydrogen bonds within and between adjacent polymer strands, which may provide more than half this barrier, 13.86 k_BT or (4 bonds*3.38 k_BT or 34.3 kJ mol^{-1}). Combining the hydrogen bonds with the glycosidic bond energy represents 94% of the barrier. An additional 2.32 k_BT (5.73 kJ mol^{-1}) is available from solvation of cellobiose. From a work perspective we can conservatively estimate that *Tr*Cel7A can step 1 nm against a 20 pN load, which is 20 pN*nm or 5 k_BT equal to virtually all of the energy available from the glycosidic bond. Both the activation barrier result and measured work suggest *Tr*Cel7A uses energy in addition to the glycosidic bond such as contributions from cellulose decrystallization, hydrogen bonding, and cellobiose solvation. In this analysis, we consider the energies available in the context of the initial and final state of each cycle of processive steps such that the order of energy usage from these potential sources is not determined or dictated. Additionally, the flat profile of the force-velocity curve for opposing load suggests that the rate limiting steps in a cycle are non-mechanical (biochemical) [32, 33].

Comparing wt*Tr*Cel7A, isolated CD and CBM constructs parses the role of each of the various sub-domains. The CD fully captures step size and dwell time distributions of wt*Tr*Cel7A motility, establishing that the motility cycle mechanism is wholly contained within the CD unit. This indicates that the CD is independently capable of the translocation exhibited by the full wt*Tr*Cel7A enzyme. However, the shorter dwell times of the isolated CD construct suggests that the presence of the CBM and linker domains may slightly impede motility. At the same time, CBM bond lifetimes (1.7 s), while consistent with wt*Tr*Cel7A dwell times (1.6 s), are sufficiently weak in comparison to the performance of the wt*Tr*Cel7A motor. This indicates that the CBM is likely designed to avoid imped-

ing motility while also increasing substrate adsorption. CBM bond lifetimes are similar to those found in solution through Biacore (3.1 s) and consistent with reported non-productive binding times (1.16 s) [13].

Given the relative processivity of the CD it is curious why *Tr*Cel7A maintains its 'ball and chain' partner. The presence of the CBM suggests binding enhancement is needed for initial commitment to motility, a rate limiting step, where a free cellulose end is found and threaded into the CD. Actively placing a CD functionalized bead atop a cellulose strand, artificially associating the two as in our tweezers based assay, was sufficient to initiate motility. Strong initial binding to cellulose by the CD itself might aide in initiating motility, but interfere with productive stepping. Sequestering these tasks across separate domains, through a flexible linker, with similar stepping and off rate times achieves both goals while minimizing physical interference between conflicting desires to bind, negotiate roadblocks, and move. The cellulose/cellulase system in many ways parallels other degradation machinery and strategies found in systems such as in protein degradation by ClpXP [20, 32] and collagen by collagenases [34] both of which play significant roles in balance and regulation of natural systems.

Leveraging this and other SM assays with functional mutation of motor domains holds much promise in revealing cellulose degradation mechanisms. In contrast to this SM assay, Igarashi measured higher velocities using highly crystalline algae derived cellulose under conditions of higher motor concentration (30 fold greater) [7] supporting previous studies that suggest subtle variations in substrate and motor-motor interactions may significantly enhance motility [12, 35, 36, 37]. Despite high spatial resolution of the AFM, individual steps were not observed. The observed velocity increase with assisting loads seen here suggests multiple motor interactions, as seen in by Igarashi *et al*. [7], may substantially enhance degradation rates. Both Igarashi's and the present study report a spread of velocities while some individual traces exhibit relatively straight trajectories. The spread in velocities can be indicators of heterogeneity in types of motility, stochastics of individual

motors and substrate inhomogeneity while the level of uniformity within individual traces can occur from a cycle containing multiple steps of similar rates in individual motor or from multiple motors working in concert. Future work focused on cellulose degradation systems with multiple enzymatic components will investigate various processing strategies of cellulose substrates and synergistic interactions between cellulase cocktail component enzymes. Ultimately, processes that integrate biological strategies with industrial processing of cellulose as an energy source have much promise.

2.5 Materials and Methods

2.5.1 Materials

Sulfo-SMCC crosslinker (Thermo Scientific - 22622), 1010 bp DNA functionalized with appropriate end groups (primers specified in the following methods), 1.25 μm streptavidin polystyrene beads (Spherotech - SVP-10-5), 0.75 μm polystyrene beads (Spherotech - PP-08-10), 1.0 μm carboxylated polystyrene beads (Polysciences - 08266), biotinylated BSA (5 mg mL^{-1}, received as a gift from Ted Feldman at Harvard University), BSA (Sigma - A3059), 50 mM acetate buffer (pH 4.9), PBS (1x, pH 7.4), Whatman Grade 1 Filter Paper (Sigma - WHA1001110), *Trichoderma reesei* cellulase mixture (Sigma - C2730) and deionized (DI) water.

2.5.2 Enzyme purification (wt*Tr*Cel7A)

wt*Tr*Cel7A was purified from a *Trichoderma reesei* cellulase mixture (Sigma C2730) using step-elution ion chromatography [17]. First, 450 μL cellulase mixture was buffer exchanged to 10 mM TEA-HCl (pH 7.6) using 6 x Biorad P30 chromatography columns according to the columns' protocol. Purification was then carried out using a Q-Trap ion chromatorgraphy column (GE Healthcare - 17-1153-01). The column was first washed with 5 column volumes (5 mL) of 20 mM TEA-HCl (pH 7.0) at a rate of approximately 1 mL

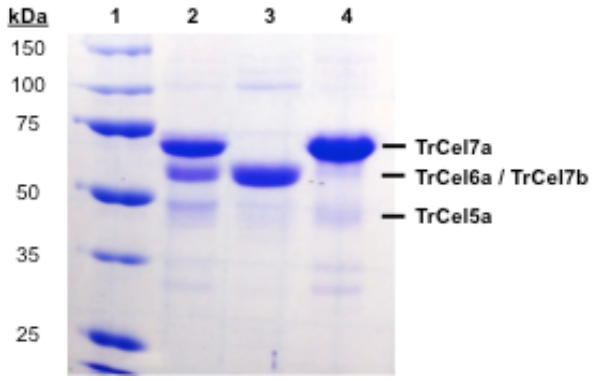

Figure 2.10: **wt*Tr*Cel7A purification (SDS-PAGE).** SDS-PAGE gel showing the purification *Tr*Cel7A from a commercial *Trichoderma reesei* cellulase mix. Lane 1 is a prestained protein standard whose band values are listed to the left of the image. Lane 2 is the original cellulase mixture. Lane 3 is the low salt elutant containing mostly the lighter *Tr*Cel6A and *Tr*Cel7B at 55 kDa. Lane 4 is the high salt elutant containing the desired *Tr*Cel7A at approximately 64 kDa. The light band seen at approximately 49 kDa in all lanes is due to the endoglucanase, *Tr*Cel5A.

min^{-1}. Note that flow through the column is promoted through a pressure differential created by applying a vacuum to the collection container. The column was then washed with 5 column volumes (5mL) of 0.1M NaCl in 20mM TEA-HCl (pH 7.0) and again washed with 5 mL of 20 mM TEA-HCl (pH 7.0). Three hundred microliters of the cellulase sample is then loaded into the top of the column. The column was washed with 4 mL of 20 mM TEA-HCl (pH 7.0). The other enzymes in the sample were then eluted by applying 2 mL of 0.1M NaCl in 20 mM TEA-HCl (low salt solution) to the column. Finally, the desired *Tr*Cel7A was eluted by applying 1.6 mL 0.33M NaCl in 20 mM TEA-HCl, pH 7.0 (high salt solution) to the column. Purity was confirmed using SDS-PAGE (Fig. 2.10) where *Tr*Cel7A is approximately 64-66 kDa and accounts for 55-60% of the cellulase mixture [10, 17]. Purified samples were buffer exchanged to acetate buffer with 10% glycerol, diluted to 0.4 mg mL^{-1} aliquots and stored at -80°C for future use.

2.5.3 Enzyme expression and purification (isolated CD and CBM)

Carbohydrate-binding domain (CBM) and the catalytic domain (CD) were both expressed in Singapore by Sarangapani Sreelatha using GC5 competent *E. coli*. The CBM includes 9 aa of the linker domain with a His tag at the N terminus (His6-TTTGSSPGP-TQSHYGQCGGIGYSGPTVCASGTTCQVLNPYYSQC). The CD has a biotin tag, via a His6 tag and BCCP link, at the 11th amino acid (His) on the N terminus. No linker domain is present in the CD construct.

Expression plasmids DNA fragments encoding the linker domain sequence with the CBM region and the CD region were amplified by PCR using primers containing appropriate restriction sites for fusion and insertion into the pUC 57 plasmid to create entry clones of the constructs. The primers used are as follows: for the CBM, forward primer - CCC GAC CCA GAG CCA TTA T and reverse primer - CAC TGG CTA TTA ATA CGG GTT CAG, and for the CD, forward primer - CGA TAC CCC TGT GCA TTG TGG and reverse primer - AGT TCG CAT CAA TCA CCA CG. The PCR conditions were 30 cycles of denaturation at 94°C for 1 min, annealing at 50°C for 2 min and extension at 72°C for 30 s with the final extension step run for 5 min. The sequence encoding the CBM with linker was restricted with NdeI and XhoI (Promega, USA) and sub cloned between the restriction sites of pET28b expression vector, enabling fusion of the polypeptide His6 tag. In the case of the CD the entire fragment encoding the CD of *Tr*Cel7A with a BCCP subunit was subcloned into NdeI and XhoI sites of the pET28b expression vector with fusion of the polypeptide His6 tag. The recombinant plasmids were then transformed in GC5TM (Sigma-Aldrich, USA) competent *E.coli* cells. Kanamycin resistant colonies were isolated and their nucleotide sequence verified by DNA sequencing (First base, Singapore).

Enzyme production and Purification. Overnight pre-cultures of the transformants (2.5 mL) were inoculated into 100 mL of lysogeny broth (LB) medium containing 50 μg mL^{-1} of kanamycin and shaken at 37°C and 120 rpm. Protein expression was induced by adding 1 mM of isopropyl-β-D-thio-galactopyranoside (IPTG), when the OD600 reached

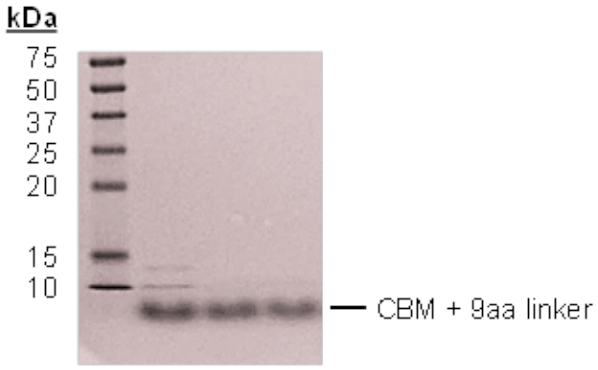

Figure 2.11: **Isolated CBM purification (SDS-PAGE).** A gel showing purified, isolated CBM including 9 aa of the linker domain (∼6 kDa).

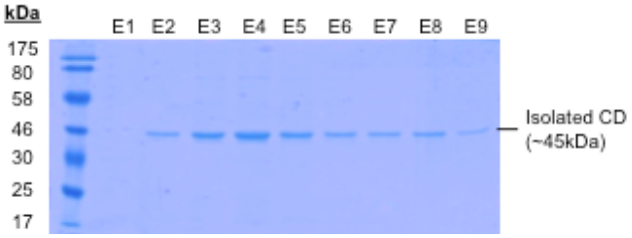

Figure 2.12: **Isolated CD purification (SDS-PAGE).** A gel showing purified, isolated CD domain (∼45 kDa) in which each lane is a fraction of the sequential elution of CD from the HisTrap FF Ni2+-NTA affinity column during purification.

0.4-1.0. After induction, the transformants were grown under the same conditions for 6 h (CBM and CD) to produce proteins. After cultivation, cells were collected by centrifugation at 5000 xg for 10 min and gently disrupted by the use of B-PER bacterial extraction reagent (Thermoscientifc) according to the manufacturer's instruction. Two volumes of 100 mM sodium acetate buffer (pH 4.0) was added to remove the *E.coli* derived proteins. After 1 day, the cell suspension was centrifuged at 18,000 g for 20 min. The resulting soluble extract was purified with HisTrap FF Ni2+-NTA affinity column (GE healthcare). The supernatant containing the purified enzyme was dialyzed by ultrafiltration (PBGC membrane, Millipore) with 10 mM acetate buffer to pH values allowing for protein stability. The purified enzymes were frozen and stored at -20°C. Purity of the proteins was confirmed using SDS-PAGE (Figs. 2.11-2.12). Protein concentrations were determined using Nanodrop 1000 (Thermoscientific, USA).

2.5.4 Bead functionalization

All proteins were tethered to polystyrene beads with a 1010 bp DNA linker with the appropriate functionalizations. The 1010 bp DNA linkers were created using PCR and the M13mp18 plasmid template. All primers were ordered from Integrated DNA Technologies (IDT). In the case of wt*Tr*Cel7A, one 5' biotinylated primer (forward, 5'-biotin-TAT TGC GTT TCC TCG GTT TC-3') and one 5' thiol functionalized primer (reverse, 5'-thiol-TTG AAA TAC CGA CCG TGT GA-3') were used. One 5' amine primer (reverse, 5'-amine-TTG AAA TAC CGA CCG TGT GA-3') and one 5' digoxygenin functionalized primer (forward, 5'-Dig-TAT TGC GTT TCC TCG GTT TC-3') were used for isolated CD and isolated CBM. After PCR the amine functionalized end of the tethers for isolated CD were crosslinked to 1/2 anti-biotin antibody (described later) while tethers for isolated CBM were crosslinked to anti-His antibody (Genscript - A000186-100), using EDC chemisty. Similar DNA linkers have been used in the lab previously [32, 38].

In the case of wt*Tr*Cel7A, enzyme was tethered to 1.25 μm streptavidin polystyrene beads (Spherotech - SVP-10-5) in three steps to achieve approximately one enzyme per bead. First, a wt*Tr*Cel7A sample was reacted with sulfo-SMCC crosslinker in PBS on a rotator at room temperature for 30 minutes. The reaction targets the approximately 8 surface lysines found on the CD. Following incubation, excess crosslinker was removed using a Biorad P-30 chromatography column. The resulting proteins were then bound to the thiol-functionalized end of a 1010 bp DNA linker via the sulfo-SMCC (sulfosuccinimidyl 4-(N-maleimidomethyl)cyclohexane-1-carboxylate) crosslinker by incubating the components at room temperature in PBS (1x, pH 7.4) for 30 minutes, on a rotator. Finally, functionalized beads were created by mixing biotinylated linker-bound enzyme and biotinylated BSA (bBSA) (1:10 ratio), with a final enzyme concentration of approximately 5 μg mL^{-1} ($\sim$78 nM *Tr*Cel7A), and 1.25 μm streptavidin polystyene beads in acetate buffer. The bead solution is incubated on a rotator at 4°C for 45 minutes. After incubation, beads were washed by centrifuging for 2.5 minutes at 9400 xg, aspirating, and re-suspending the pellet

in 50mM acetate buffer (pH 4.9) to remove unreacted bBSA and enzyme.

CD functionalized beads were created by tethering CD to 1.0 μm anti-Dig coated polystyrene beads in one step. The protein, expressed with a BCCP biotin tag is mixed with picomolar concentrations of 1010 bp DNA tethers (functionalized with Dig at one end and 1/2 anti-biotin at the other), anti-Dig beads, and BSA (0.125 mg mL^{-1} final concentration) in PBS. After incubation on at rotator at 4°C for 45 minutes, the beads are washed and the buffer replaced with 50 mM acetate buffer (pH 4.9) three times by centrifuging the sample for 4 minutes at 8000 xg in order to remove excess and unreacted CD and DNA. The 1/2 anti-biotin used to functionalize the DNA tether is prepared as described below.

CBM functionalized beads were created by tethering CBM to 1.0 μm anti-Dig coated polystyrene beads in one step. The protein, expressed with a His6 tag, is mixed with picomolar concentrations of DNA tethers (functionalized with Dig at one end and anti-His at the other), anti-Dig beads, and BSA (0.125 mg mL^{-1} final concentration) in PBS. After incubation on at rotator at 4°C for 45 minutes, the beads are washed and the buffer replaced with 50 mM acetate buffer (pH 4.9) three times by centrifuging the sample for 4 minutes at 8000 xg in order to removed excess and unreacted CBM and DNA.

2.5.5 Partial reduction of anti-biotin antibody

Anti-biotin antibody is obtained from Sigma-Aldrich (B3640) and dissolved into reaction buffer (20 mM sodium phosphate, 0.15 M NaCl, 5 mM EDTA at pH 7.4) to a concentration of 10 mg mL^{-1}. A 19 mg mL^{-1} solution of 2-MEA in reaction buffer is also prepared. Two microliters of 2-MEA solution is then mixed with 10 μL anti-biotin antibody solution and incubated for 90 minutes at 37°C. Reduced antibody is then purified using a Biorad P-30 chromatography column. The methods described here are the same as those used by Das et al [38]. The resulting 1/2 anti-biotin antibody is linked to the amine functionalized end of DNA tethers using Sulfo-SMCC crosslinker.

2.5.6 Filter paper preparation

The substrate used in these studies, except when specifically specified as *Cladophora*, is Whatman Grade 1 Filter Paper (Sigma - WHA1001110)) and contains 99% cellulose. To generate the desired fibers, small 1 mm^2 pieces were cut from a single filter paper sheet. Approximately 20 mg of filter paper was wetted with a few drops of DI water in a tissue homogenizer and homogenized for 5 minutes. The substrate solution was then diluted to a mixture of 2 mg substrate mL^{-1} with 50 mM acetate buffer (pH 5.0). The substrate was then subjected to mechanical processing through repeated sonication, vortexing, and shearing/mixing by passing the solution through a 16 gauge syringe. The substrate was stored at 4°C until use.

2.5.7 *Cladophora* cellulose preparation and characterization

Highly crystalline, triclinic cellulose Iα from *Cladophora sp.* (*Cladophora glomerata*) filamentous green algae was harvested from fresh water Lake Mendota (Madison, WI, USA) and adjoining water-bodies connected by the Yahara river [39, 40], prepared, and provided to us for this study by Shishir Chundawat using the following procedures. Recovered algae was washed extensively with deionized water to remove contaminants prior to long-term storage at -20°C. The cleaned algae fibers were bleached for 30 mins at room temperature by immersing 5-15 g of algae (on dry weight basis) in 100 ml of 10% acetic acid solution containing 20 g sodium chlorite. The solution was diluted to 1 liter with deionized water, incubated at 60°C in a hot water bath for 3 hours, and subsequently washed to neutral pH with deionized water. The fibers were then incubated twice overnight in a 1 liter solution of 4% sodium hydroxide at 60°C to facilitate removal of non-cellulosic polysaccharides. The recovered samples were then washed to neutral pH and incubated with 250 mL of boiling solution of 5% hydrochloric acid for 15 mins and left incubated in the same solution overnight at room temperature to facilitate hydrolysis

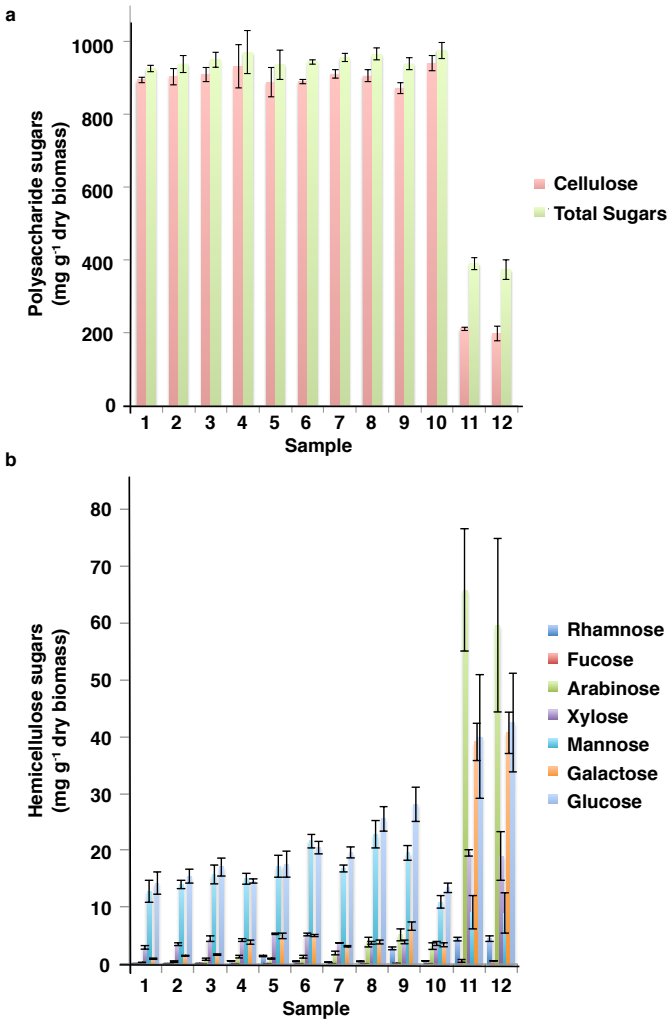

Figure 2.13: ***Cladophora* derived substrate carbohydrate composition.** Carbohydrate compositions (dry weight basis) of twelve tested extraction conditions (% acetic acid, acetic acid solution pH, NaOH extraction solution strength and number of extractions) as outlined in Samples 11 and 12 are unextracted controls. Samples were tested for (a) cellulose and (b) hemicellulosic carbohydrate composition. All assays were carried out in triplicates with mean values reported here. Error bars indicate s.d. for reported mean values. Unextracted Cladophora algae biological replicates (Samples 11 and 12) were collected from two separate locations in Lake Mendota and adjoining water bodies.

and removal of amorphous cellulose. The samples were washed extensively with deionized water till neutral pH the next day to obtain highly crystalline cellulose fibrils suspension slurry. The cellulose slurry was either stored at 4°C in the presence of sodium azide or lyophilized for long-term storage and further characterization by x-ray diffraction, Raman

spectroscopy, and carbohydrate composition analysis. The algal cellulose extraction conditions were varied (Table. 2.1) to maximize total crystalline cellulose content (Fig. 2.13a) as estimated using standard carbohydrate detection and quantification methods [41]. Additionally, non-cellulosic polysaccharide contamination was verified to be minimal for all samples (Fig. 2.13b) with crystalline cellulose content for samples used in this study to be $96.2 \pm 5.7\%$ (dry weight basis).

Table 2.1: *Cladophora* cellulose extraction conditions

Sample Number	% Acetic Acid, pH	1st NaOH Extraction*	2nd NaOH Extraction*
1	1%, 2.5	1M	-
2	1%, 2.5	0.5M	-
3	1%, 2.5	0.1M	-
4	1%, 2.5	0.1M	0.5M
5	1%, 2.5	0.1M	0.1M
6	1%, 2.5	0.5M	0.5M
7	10%, 2.5	1M	-
8	10%, 4.5	1M	-
9	1%, 4.5	0.5M	-
10	1%, 4.5	0.5M	0.5M
11	Unextracted Cladophora algae biological replicate 1		
12	Unextracted Cladophora algae biological replicate 2		

*Each NaOH extraction step was carried out overnight at 60°C.

Pelletized lyophilized cellulose samples (100-150 mg; dry weight per pellet) were analyzed on a Bruker MultiRam spectrometer (Bruker Instruments Inc., Billerica, Massachusetts) at the USDA-FPL (Madison, WI). Data was collected using a 600 mW Nd-YAG laser with 512 scans per sample. Bruker's OPUS software was used to determine peak positions and analyze Raman spectral data. Data was normalized at 1096 cm^{-1} wavenumber shift to facilitate comparison between different samples [42]. Raman spectroscopy analysis confirmed the algal cellulose allomorph type to be predominantly Iα in content as indicated by the OH stretching vibrations resultant shoulder around wavenumber 3240 cm^{-1}, that is absent in Iβ [37, 43, 44]. Other characteristic Raman spectral features for algal cellulose Iα compared to plant-derived cellulose Iβ control (Avicel) are also shown in Fig. 2.14. X-ray diffraction analysis (Fig. 2.15) was also carried out on dried algal cellulose Iα fibers

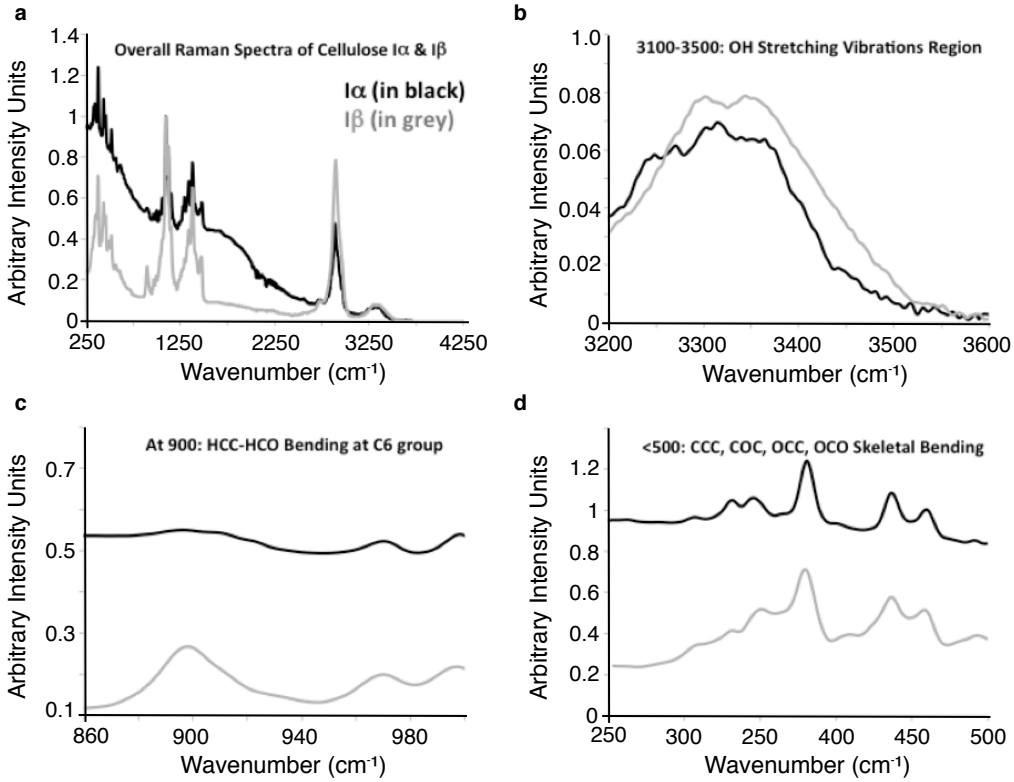

Figure 2.14: **Raman spectroscopy analysis of isolated *Cladophora*.** *Cladophora* cellulose Iα (black lines) used in this study is compared to a cellulose Iβ control (grey lines) which is the cellulose structure present in Avicel or microcrystalline cellulose from plant-derived sources. Absence of a sharp peak at 900 cm^{-1} wavenumber confirms the highly crystalline nature of algal cellulose, unlike heterogeneous plant-derived cellulose Iβ.

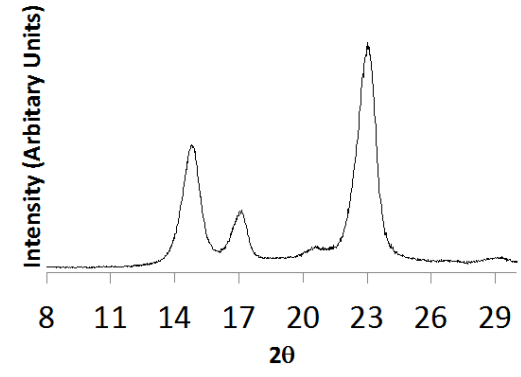

Figure 2.15: **X-ray diffraction spectra of *Cladophora* derived cellulose Iα.** The Segal method can be used to estimate algal cellulose crystallinity index (CrI) to be $\sim$92% (CrI=100*(I_{23}-I_{18})/I_{18}). Where, I_{23} and I_{18} are the XRD spectral intensities at 23 and 18 degrees two-theta values, respectively.

to determine total cellulose crystallinity of >92% based on the Segal method [37]. X-ray analysis confirmed absence of any regenerated cellulose II allomorph formed during the algal cellulose isolation process.

2.5.8 Slide preparation

Slides were prepared by first creating an approximately 15 μL flow cell using double sided sticky tape. The flow cell is then loaded through capillary action with diluted cellulose slurry. In all cases the substrate is nonspecifically immobilized on the coverslip surface by allowing the loaded chamber to evaporate until dry in an oven at 85-90°C (approximately 1 hour). Dried slides were then allowed to cool to room temperature and incubated with a BSA blocking solution before loading the functionalized beads. In the case of wt*Tr*Cel7A and isolated CD experiments, 0.75 μm non-functionalized beads were allowed to non-specifically adhere to the coverslip surface in an incubation step before BSA blocking. These beads served as fiducial markers allowing for instrumental drift tracking during data acquisition.

2.5.9 Single molecule data collection

Enzyme functionalized beads were trapped with a 1064 nm laser and placed alongside a surface bound stationary fiber. After position calibration and trap stiffness measurements, the bead was held above the fiber to facilitate binding between the protein and the substrate. Upon binding, the bead was centered by an automated 2 axis piezo stage centering routine and loaded with up to 25 pN of force through piezo stage offset motions. Bead position was recorded at 3 kHz to track motility records as long as 10 minutes. To account for instrumental drift during the measurements, the smaller non-functionalized fiducial beads were tracked simultaneous with motility records using an Andor Ixon camera to acquire synchronized images at approximately 4 Hz. In the collection of CBM bond lifetime data, instrumental drift was not tracked due to the shorter acquisition times and the nature of the

data being collected. Thus fiducial beads were left out of the assay.

Experiments were carried out at 21°C except for temperature dependence studies. For experiments at elevated temperatures (28°C and 34°C) the temperature-controlled box surrounding the microscope was equilibrated to the set temperature prior to data acquisition. Temperature dependent data sets include DNA tethered wt*Tr*Cel7A (28°C) as well as enzyme bound directly to the bead using biotinylated succinimidyl ester (21, 28 and 34°C).

2.5.10 Data analysis

Given the low velocity of the *Tr*Cel7A motor, and long experiment acquisition time ($\sim$10 minutes) we developed a method to appropriately handle sample drift. Our strategy included tracking a stationary fiducial bead so that its position could be removed from the baseline of the motor-bead position traces to yield the true enzyme trajectory. To do this, we employed a cross correlation video tracking algorithm and time-synchronized our video with motor-bead tracking by starting both acquisitions simultaneously. Drift data was then smoothed and subtracted from the motor-bead tracking data.

Data was collected at a 3 kHz sampling frequency in all experiments and decimated to 20 Hz during further analysis. Nanometer position and piconewton force values were found using calibration data and trap stiffness. Custom MATLAB scripts were used to calculate bond lifetimes, velocities, and local force-velocity information. The step finding script was modified from a previous version within the lab and based on a sliding student T-test that detects the edges of each step to prescribe a dwell and allows for varied step sizes [45]. A dwell was defined as a period of constant position between bursts of motion (steps). Specifically, an enzyme is said to be in a dwell if the change in the moving average of position is less than 0.9 nm (the minimum step-size threshold). This threshold was chosen as a result of step finding optimization and the 1nm step resolution controls. It was determined that the first bin of the dwell distributions is an artifact of the analysis and is not representative of actual behavior at those times. Thus, dwell distribution fits ignore the first

bin. It is also noted that step analysis for each trace was visually inspected for accuracy. The same analysis conditions were used for all traces in a data set. As such, step finding was not optimal for all traces, for example, a trace with larger or smaller noise than average, or those traces with very low velocity. In these cases, step analysis not always sufficiently accurate. If more than one step was obviously missed or if noise was too large, resulting in an apparent large number of steps, the trace was not used for step and dwell analysis.

Force changes during the motility trace as the bead is pulled within the fixed trap. The force was evaluated along a trace using bead position relative to the trap center over 5 second windows. The associated average velocity over the same time period was then evaluated using a linear fit of the drift adjusted time trace.

2.5.11 Activity - Mass Spectrometry

To investigate enzymatic activity, mass spectrometry was used to analyze the cellobiose product (molecular weight = 342.3) of both wt*Tr*Cel7A and isolated CD samples (1 mg mL^{-1} enzyme) that were incubated with filter paper for 68 hours at room temperature. In preparation for mass spectrometry, product from isolated CD, only filter paper negative control (no enzyme), and wt*Tr*Cel7A were diluted 0.6:10, 1.2:21.2, and 1:300, respectively, into 95.5% acetonitrile (CH_3CN) in water. Standards were prepared by creating a 100 μM solution of cellobiose (Sigma) in Millipore water and diluting to appropriate concentrations using 95.5% acetonitrile (CH_3CN) in water.

Samples were analyzed using LC-MS/MS at the Vanderbilt Mass Spectrometry Core Laboratory by Dr. Wade Calcutt on a Water Acquity UPLC system (Waters, Milford, MA), made up of a binary solvent manager, refrigerated sample manager, and a heated column manager. Tandem mass spectrometric detection was performed using a TSQ Quantum triple quadrupole mass spectrometer (Thermo Scientific, San Jose, CA) equipped with an Ion Max API source, an ESI probe, and a 50 μm ID stainless steel capillary. Experiments were performed by Assistant Director, Dr. Wade Calcutt, using his procedure below. A

Sequant ZIC-cHILIC PEEK analytical column (2.1 mm x 150 mm, 3.0 μm particle size, Merck, Darmstadt, Germany) was used for all chromatographic separations. The mobile phases consisted of 0.2% AcOH and 5 mM NH_4OAc in (A) H_2O/CH_3CN (9:1) and in (B) $CH_3CN/MeOH/H_2O$ (90:5:5). A flow rate of 300 μL min^{-1} for 15 minutes was used with sample volumes of 10 μL. Mass spectrometry analyses was in positive ion mode with a scan time of 100 ms and scan width of 0.5 Da. The calibration curve was created using the LC-MS/MS peak area against analyte concentration for cellobiose standards from 1 to 150 μM.

2.5.12 Activity - Fluorescence decoration of fibers

Binding activity was tested by observing specific decoration of both wt*Tr*Cel7A and CD to immobilized filter paper substrate. Both wt*Tr*Cel7A and isolated CD were labeled with TAMRA(5)-succinimidyl ester (se) fluorophores overnight in PBS by reacting the succinimidyl ester end of the fluorophore with surface lysines on the CD. The buffer was then exchanged to 50 mM acetate buffer (pH 4.9) and excess fluorophore removed using three P-30 column washings (Bio-rad) in series. The concentration of each solution was found using a NanoDrop and samples diluted to known molarities. Slides with immobilized cellulose (filter paper), prepared as described in the Methods section of the manuscript, were loaded with labeled enzyme of various concentrations.

2.5.13 Activity - Filter Paper Assay (FPA)

In these studies, an enzymatic activity assay using our standard filter paper substrate was conducted where reducing sugars are reacted with dinitrosalicylic acid (DNS) to form a spectroscopically detectable product. This assay was scaled down to a 7.5 μL reaction volume from the original 1987 procedure [46] and a small volume 96 well plate procedure (as described in the review by Dashthan et al. [47]). To do this, 7.5 μL of enzyme at 1mg mL^{-1} (or cellobiose standard at appropriate concentration) was added to a microcentrifuge

tube containing 1/16 of a filter paper disk created using a 3 ring hole punch. The sample was allowed to incubate at room temperature for 50 hours. At the end of the incubation time, 15 μL of DNS solution was added to the sample and incubated for 25 minutes at approximately 100°C to generate the color change associated with its reaction with reducing sugars (cellobiose). After cooling to room temperature, the reducing sugar concentration of each sample is measured by finding the absorbance at 540 nm, using the NanoDrop (Fig. 2.9).

2.5.14 Activity - CBM

During purification, CBM was purified using a His-tag column. Affinity estimates from wash and resuspension stages of a cellulose based purification procedure was also used to test the strong binding activity of the CBM, as follows. A custom cellulose column was first created in which a 0.7 mL Eppendorf tube was filled half-way to the 100 μL line with cellulose (cotton linters, Sigma). A 0.634 mg mL^{-1} (106 μM) CBM sample in 50 mM acetate buffer (183 μL total) was added to the tube and rotated at 4°C overnight. The next morning, to remove excess protein, the sample was centrifuged at room temperature for 15 minutes at 18000 xg and the supernatant removed (labeled ”flow through”). The cellulose was resuspended in 300 μL of 50 mM sodium acetate buffer (pH 4.9) and again centrifuged for 15 minutes at 18000 xg. The supernatant was collected and labeled ”wash”. The wash collects protein exhibiting low binding.

2.6 Acknowledgements

This work was supported by Singapore-MIT Alliance for Research and Technology - BioSyM, NSF (1330792), and GAANN (P200A090323). This work was also partially supported by Rutgers University, the National Science Foundation Grant Number 1236120 (CBET - Energy for Sustainability), and the Great Lakes Bioenergy Research Center (supported by the Department of Energy, Office of Science, Office of Biological and Envi-

ronmental Research, through Cooperative Agreement DE-FC02-07ER64494 between The Board of Regents of the University of Wisconsin System and the Department of Energy (DG, VB, BED, SPSC). We thank Izak Smith, Kate Helmich, Cameron Seiser, Cassandra Hainer, Umesh Agarwal, Leonardo Sousa, Cliff Foster, and Brian Fox for their timely assistance and overall support on this work. We would like to thank Dr. Yongdae Shin, Professor Clare McCabe, and Faizan Zubair, for many helpful conversations throughout this study and Kelsea Best for her help in filter paper substrate preparation. We especially thank the Vanderbilt Mass Spectrometry Core Laboratory and specifically Dr. Wade Calcutt for providing the instrumentation, expertise, and time to complete the mass spectrometry necessary for our activity studies. We thank Professor Ryoma Ohi and his lab for their guidance and advice in the expression and production of the isolated motor domains. We would also like to thank anonymous reviewers for helpful comments.

2.7 Bibliography

[1] Mihhail Kurasin and Priit Väljamäe. Processivity of cellobiohydrolases is limited by the substrate. *The Journal of biological chemistry*, 286(1):169–77, jan 2011.

[2] ANTOINETTE C O'SULLIVAN. Cellulose: the structure slowly unravels. *Cellulose*, 4(3):173–207, 1997.

[3] J. WIlliam Costerton, K. J. Cheng, Gill G. Geesey, Timothy I. Ladd, J. Curtis Nickel, Mrinal Dasgupta, and Thomas J. Marrie. Bacterial Biofilms in Nature and Disease. *Ann. Rev. Microbiol.*, 41:435–464, 1987.

[4] Cristina Solano, Begoña García, Jaione Valle, Carmen Berasain, Jean Marc Ghigo, Carlos Gamazo, and Iñigo Lasa. Genetic analysis of Salmonella enteritidis biofilm formation: Critical role of cellulose. *Molecular Microbiology*, 43(3):793–808, 2002.

[5] B Rosan and R J Lamont. Dental plaque formation. *Microbes and infection / Institut Pasteur*, 2(13):1599–1607, 2000.

[6] Kiyohiko Igarashi, Anu Koivula, Masahisa Wada, Satoshi Kimura, Merja Penttilä, and Masahiro Samejima. High speed atomic force microscopy visualizes processive movement of Trichoderma reesei cellobiohydrolase I on crystalline cellulose. *The Journal of biological chemistry*, 284(52):36186–90, dec 2009.

[7] Kiyohiko Igarashi, Takayuki Uchihashi, Anu Koivula, Masahisa Wada, Satoshi Kimura, Tetsuaki Okamoto, Merja Penttilä, Toshio Ando, and Masahiro Samejima. Traffic jams reduce hydrolytic efficiency of cellulase on cellulose surface. *Science (New York, N.Y.)*, 333(6047):1279–82, sep 2011.

[8] Andrew Carroll and Chris Somerville. Cellulosic biofuels. *Annual review of plant biology*, 60:165–82, jan 2009.

[9] Douglas B Jordan, Michael J Bowman, Jay D Braker, Bruce S Dien, Ronald E Hector, Charles C Lee, Jeffrey a Mertens, and Kurt Wagschal. Plant cell walls to ethanol. *The Biochemical journal*, 442(2):241–52, mar 2012.

[10] Tuula T. Teeri. Crystalline cellulose degradation: New insight into the function of cellobiohydrolases. *Trends in Biotechnology*, 15(5):160–167, 1997.

[11] M L Sinnott. The cellobiohydrolases of Trichoderma reesei: a review of indirect and direct evidence that their function is not just glycosidic bond hydrolysis. *Biochemical Society transactions*, 26(2):160–164, 1998.

[12] Dieter Klemm, Brigitte Heublein, Hans Peter Fink, and Andreas Bohn. Cellulose: Fascinating biopolymer and sustainable raw material. *Angewandte Chemie - International Edition*, 44(22):3358–3393, 2005.

[13] Yusuke Shibafuji, Akihiko Nakamura, Takayuki Uchihashi, Naohisa Sugimoto, Shingo Fukuda, Hiroki Watanabe, Masahiro Samejima, Toshio Ando, Hiroyuki Noji, Anu Koivula, Kiyohiko Igarashi, and Ryota Iino. Single-molecule imaging analysis of elementary reaction steps of Trichoderma reesei cellobiohydrolase I (Cel7A) hydrolyzing crystalline cellulose Iα and III(i). *Journal of Biological Chemistry*, 289(20):14056–14065, 2014.

[14] Jaemyeong Jung, Anurag Sethi, Tiziano Gaiotto, Jason J. Han, Tina Jeoh, Sandrasegaram Gnanakaran, and Peter M. Goodwin. Binding and movement of individual Cel7A cellobiohydrolases on crystalline cellulose surfaces revealed by single-molecule fluorescence imaging. *Journal of Biological Chemistry*, 288(33):24164–24172, 2013.

[15] Nicolaj Cruys-Bagger, Hirosuke Tatsumi, Guilin Robin Ren, Kim Borch, and Peter Westh. Transient kinetics and rate-limiting steps for the processive cellobiohydrolase

Cel7A: Effects of substrate structure and carbohydrate binding domain. *Biochemistry*, 52(49):8938–8948, 2013.

[16] Anders Thygesen, Jette Oddershede, Hans Lilholt, Anne Belinda Thomsen, and Kenny Ståhl. On the determination of crystallinity and cellulose content in plant fibres. *Cellulose*, 12(6):563–576, 2005.

[17] Zhuoliang Ye, Andrew N Lane, Gerold A Willing, and R Eric Berson. Scaled-up separation of cellobiohydrolase1 from a cellulase mixture by ion-exchange chromatography. *Biotechnology progress*, 27(6):1644–1652, 2011.

[18] Francois Baneyx. Recombinant protein expression in Escherichia coli. *Current Opinion in Biotechnology*, 10:411–421, 1999.

[19] Craig M. Dana, Alexandra Dotson-Fagerstrom, Christine M. Roche, Sarala M. Kal, Harshal a. Chokhawala, Harvey W. Blanch, and Douglas S. Clark. The importance of pyroglutamate in cellulase Cel7A. *Biotechnology and Bioengineering*, 111(4):842–847, 2014.

[20] Juan Carlos Cordova, Adrian O Olivares, Yongdae Shin, Benjamin M Stinson, Stephane Calmat, Karl R Schmitz, Marie-Eve Aubin-Tam, Tania A Baker, Matthew J Lang, and Robert T Sauer. Stochastic but highly coordinated protein unfolding and translocation by the ClpXP proteolytic machine. *Cell*, 158(3):647–658, 2014.

[21] Bernd Nidetzky, W Steiner, and Marc Claeyssens. Cellulose hydrolysis by the cellulases from Trichoderma reesei: adsorptions of two cellobiohydrolases, two endocellulases and their core proteins on filter paper and their relation to hydrolysis. *Biochemical Journal*, 303(3):817–823, 1994.

[22] H Boer, T T Teeri, and a Koivula. Characterization of Trichoderma reesei cellobiohydrolase Cel7A secreted from Pichia pastoris using two different promoters. *Biotechnology and bioengineering*, 69(5):486–94, sep 2000.

[23] Elio a Abbondanzieri, Joshua W Shaevitz, and Steven M Block. Picocalorimetry of transcription by RNA polymerase. *Biophysical journal*, 89(6):L61–L63, 2005.

[24] Julie L Fiore, Benedikt Kraemer, Felix Koberling, Rainer Edmann, David J Nesbitt, and J David. Enthalpy-Driven RNA Folding: Single -Molecule Thermodynamics of Tetraloop-Recertor Tertiary Interaction. *Biochemistry*, 48(11):2550–2558, 2009.

[25] Elio a Abbondanzieri, William J Greenleaf, Joshua W Shaevitz, Robert Landick, and Steven M Block. Direct observation of base-pair stepping by RNA polymerase. *Nature*, 438(7067):460–465, 2005.

[26] R S Rock, S E Rice, a L Wells, T J Purcell, J a Spudich, and H L Sweeney. Myosin VI is a processive motor with a large step size. *Proceedings of the National Academy of Sciences of the United States of America*, 98(24):13655–13659, 2001.

[27] Bason E Clancy, William M Behnke-Parks, Johan O L Andreasson, Steven S Rosenfeld, and Steven M Block. A universal pathway for kinesin stepping. *Nature structural & molecular biology*, 18(9):1020–1027, 09 2011.

[28] Samara L. Reck-Peterson, Ahmet Yildiz, Andrew P. Carter, Arne Gennerich, Nan Zhang, and Ronald D. Vale. Single-Molecule Analysis of Dynein Processivity and Stepping Behavior. *Cell*, 126(2):335–348, 2006.

[29] Roop Mallik, Brian C Carter, Stephanie a Lex, Stephen J King, and Steven P Gross. Cytoplasmic dynein functions as a gear in response to load. *Nature*, 427(6975):649–652, 2004.

[30] Brandon C. Knott, Michael F. Crowley, Michael E. Himmel, Jerry Ståhlberg, and Gregg T. Beckham. Carbohydrate-protein interactions that drive processive polysaccharide translocation in enzymes revealed from a computational study of cellobiohydrolase processivity. *Journal of the American Chemical Society*, 136(24):8810–8819, 2014.

[31] Chandrika Mulakala and Peter J. Reilly. Hypocrea jecorina (Trichoderma reesei) Cel7A as a molecular machine: A docking study. *Proteins: Structure, Function and Genetics*, 60(4):598–605, 2005.

[32] Marie-Eve Aubin-Tam, Adrian O Olivares, Robert T Sauer, Tania A Baker, and Matthew J Lang. Single-molecule protein unfolding and translocation by an ATP-fueled proteolytic machine. *Cell*, 145(2):257–267, 2011.

[33] Michelle D Wang, Mark J Schnitzer, H Yin, Robert Landick, Jeff Gelles, and Steven M Block. Force and velocity measured for single molecules of RNA polymerase. *Science (New York, N.Y.)*, 282(5390):902–7, 1998.

[34] Susanta K Sarkar, Barry Marmer, Gregory Goldberg, and Keir C Neuman. Single-molecule tracking of collagenase on native type I collagen fibrils reveals degradation mechanism. *Current Biology*, 22(12):1047–1056, 2012.

[35] Thomas Ganner, Patricia Bubner, Manuel Eibinger, Claudia Mayrhofer, Harald Plank, and Bernd Nidetzky. Dissecting and reconstructing synergism: in situ visualization of cooperativity among cellulases. *The Journal of biological chemistry*, 287(52):43215–22, dec 2012.

[36] Mélanie Hall, Prabuddha Bansal, Jay H. Lee, Matthew J. Realff, and Andreas S. Bommarius. Cellulose crystallinity - A key predictor of the enzymatic hydrolysis rate. *FEBS Journal*, 277(6):1571–1582, 2010.

[37] Shishir P S Chundawat, Giovanni Bellesia, Nirmal Uppugundla, Leonardo Da Costa Sousa, Dahai Gao, Albert M. Cheh, Umesh P. Agarwal, Christopher M. Bianchetti, George N. Phillips, Paul Langan, Venkatesh Balan, S. Gnanakaran, and Bruce E. Dale. Restructuring the crystalline cellulose hydrogen bond network enhances its depolymerization rate. *Journal of the American Chemical Society*, 133(29):11163–11174, 2011.

[38] Dibyendu Kumar Das, Yinnian Feng, Robert J. Mallis, Xiaolong Li, Derin B. Keskin, Rebecca E. Hussey, Sonia K. Brady, Jia-Huai Wang, Gerhard Wagner, Ellis L. Reinherz, and Matthew J. Lang. Force-dependent transition in the T-cell receptor β-subunit allosterically regulates peptide discrimination and pMHC bond lifetime. *Proceedings of the National Academy of Sciences*, 112(5):1517–1522, 2015.

[39] Shahrizim B. Zulkifly, James M. Graham, Erica B. Young, Robert J. Mayer, Michael J. Piotrowski, Izak Smith, and Linda E. Graham. The Genus Cladophora Kützing (Ulvophyceae) as a Globally Distributed Ecological Engineer. *Journal of Phycology*, 49(1):1–17, 2013.

[40] Albert Mihranyan. Cellulose from Cladophorales Green Algae: From Environmental Problem to High-Tech Composite Materials. *Journal of Applied Polymer Science*, 119:2449–2460, 2011.

[41] Cliff E. Foster, Tina M. Martin, and Markus Pauly. Comprehensive Compositional Analysis of Plant Cell Walls (Lignocellulosic biomass) Part II: Carbohydrates. *Journal of Visualized Experiments*, (37):10–13, 2010.

[42] Umesh P Agarwal, Sally A Ralph, Richard S Reiner, and Carlos Baez. Probing crystallinity of never-dried wood cellulose with Raman spectroscopy. *Cellulose*, 23(1):125–144, 2016.

[43] Shishir P. S. Chundawat, Bryon S. Donohoe, Leonardo da Costa Sousa, Thomas Elder, Umesh P. Agarwal, Fachuang Lu, John Ralph, Michael E. Himmel, Venkatesh Balan, and Bruce E. Dale. Multi-scale visualization and characterization of lignocellulosic plant cell wall deconstruction during thermochemical pretreatment. *Energy & Environmental Science*, 4(3):973, 2011.

[44] Rajai H. Atalla and David L. Vanderhart. Studies on the structure of cellulose using

raman spectroscopy and solid state 13C NMR. *IPC Technical Paper Series*, 217, 1987.

[45] Brian C Carter, Michael Vershinin, and Steven P Gross. A comparison of step-detection methods: how well can you do? *Biophysical journal*, 94(1):306–319, 2008.

[46] T. K. Ghose. Measurement of Cellulase Activities. *Pure and Applied Chemistry*, 59(2):257–268, 1987.

[47] Mehdi Dashtban, Miranda Maki, Kam Tin Leung, Canquan Mao, and Wensheng Qin. Cellulase activities in biomass conversion: measurement methods and comparison. *Critical reviews in biotechnology*, 30(4):302–309, 2010.

Chapter 3

*Tr*Cel7A MOTILITY COMMITMENT IS DEPENDENT ON SUBSTRATE CRYSTAL STRUCTURE

3.1 Summary

Expanding on the findings in Chapter 2, this chapter explores the motility and binding behavior of *Tr*Cel7A on native cellulose I and pretreated cellulose III from *Cladophora* algae. Our work seeks to help explain the increased rate of hydrolysis seen for cellulose III despite decreased binding affinity and decreased activity of many of the isolated enzymes [1]. Our findings agree with these previous observations as we see slower motility on cellulose III, instability of initial binding of full *Tr*Cel7A on cellulose III, and a lower average bond lifetime of CBM1 on cellulose III. A closer look at these findings seeks to explain the causes of these observations and speculates as to the synergy that allows for high rates of hydrolysis when a mixture of enzymes is present.

3.2 Introduction

Over the years, researchers have optimized processes to hydrolyze cellulose using native substrates and enzymes by adjusting reaction conditions, concentrations, residence times, etc. However, this is not enough. The process is slow and too much cellulose is lost as waste. As a result, researchers have taken two main approaches to improve processes of cellulose hydrolysis: the engineering of cellulases and the modification of cellulose substrates.

Substrate modification can be accomplished with phosphoric acid treatment that decreases crystallinity to produce amorphous cellulose [2, 3] or through a pretreatment process using an ammonia treatment [4]. The latter yields a cellulose substrate, cellulose III, that maintains the same high crystallinity of native cellulose I allomorphs, but has a more

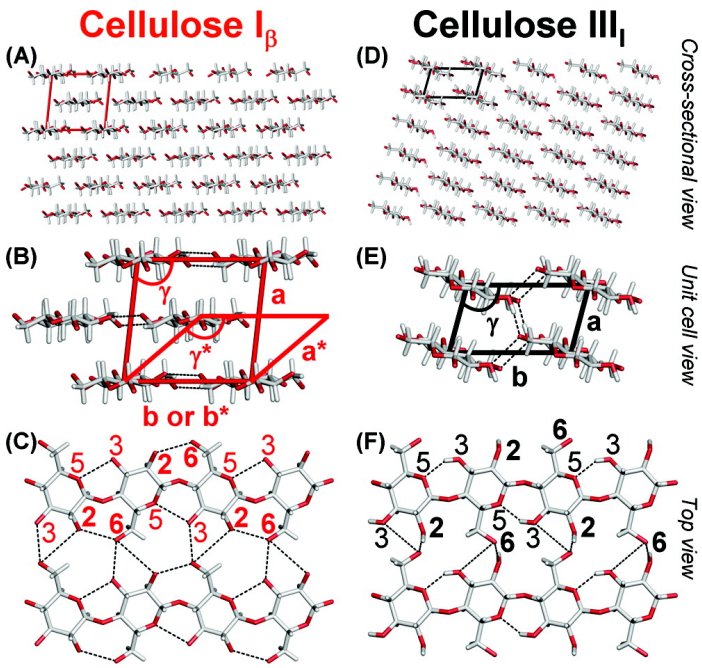

Figure 3.1: **Crystal structure** of cellulose I_β (A-C) and cellulose III (D-F) and their hydrogen bonding, including cross sectional (A,D), unit cell (B,E), and top views (C,F). This figure is reprinted with permission from (Chundawat, Shishir PS, et al. "Restructuring the crystalline cellulose hydrogen bond network enhances its depolymerization rate." Journal of the American Chemical Society 133.29 (2011): 11163-11174.). Copyright 2011 American Chemical Society.

hydrophilic surface with fewer interstrand hydrogen bonding [1, 5] (Fig. 3.1).

Interestingly, it has been found that bulk hydrolysis rates are consistently higher on cellulose III (up to five times that of cellulose I) for cellulase cocktails [1]. A 2007 report also reported that isolated *Tr*Cel7A had increased rates of hydrolysis on cellulose III [6], however, Chundawat et al's more recent work found that the opposite to be true [1]. Studies probing enzyme affinity for this new substrate have yielded mixed results. However, the increased hydrophilicity of cellulose III would predict a lower affinity to *Tr*Cel7A. More recent studies have supported this prediction, including work by Chundawat *et al.* [7] which shows that in addition to isolated enzymes exhibiting a lower affinity, an array of CBMs, including the CBM1 associated with *Tr*Cel7A, all yield reduced partition coefficients (ratio of bound to free protein). They found this to be true on both algae and corn stover derived cellulose III, so it is not a function of the specific source of the substrate.

To further investigate the findings of Chundawat *et al.* and to determine the substrate's affect on single molecule behavior, we utilized the optical trapping assays developed in Chapter 2 and exchanged the filter paper substrate with cellulose I_α, denoted here simply as cellulose I, and III from *Cladophora* algae.

3.3 Results

3.3.1 Motility characterization

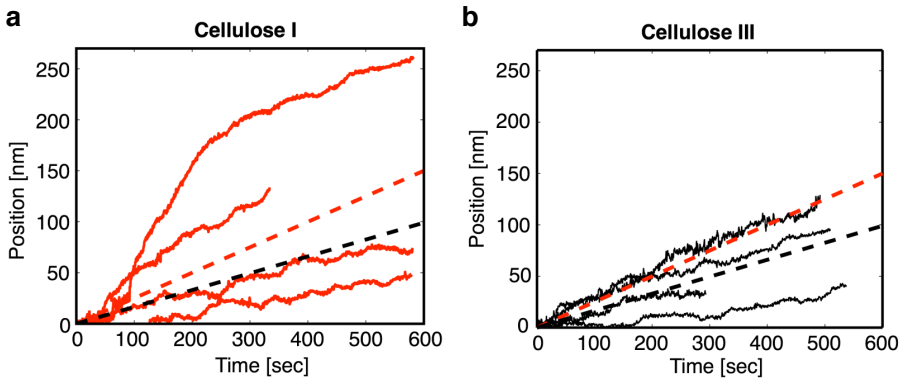

Figure 3.2: **Sample motility traces** on (a) *Cladophora* cellulose I and (b) *Cladophora* cellulose III, showing the average velocities of 0.25 $\pm$ 0.35 nm s^{-1} (s.d.; N=68; red - cellulose I) and 0.17 $\pm$ 0.14 nm s^{-1} (s.d.; N=30; black - cellulose III) using dotted lines.

Optical trapping experiments mirroring those described in Chapter 2 were employed to continue studies on these algae-based substrates. As on filter paper, motility experiments yield structured position vs time traces with a range of velocities for each. As seen in Fig. 3.2, traces were generally straight, although changes in velocity throughout the trace were observed with velocities for cellulose I ranging from 0.03 to 2.54 nm s^{-1} while that of cellulose III ranges from 0.02 to 0.59 nm s^{-1}. As suggested by bulk experiments, *Tr*Cel7A has a higher velocity on cellulose I compared to cellulose III with a weighted average velocity of 0.25 nm s^{-1} $\pm$ 0.04 (s.e.m.) compared to 0.17 nm s^{-1} $\pm$ 0.02 (s.e.m.) on cellulose III. Average velocities are found by applying a linear fit to each trace and are weighted based on the duration of each trace. These averages represent all traces, including

those in which steps were not clear enough for step analysis.

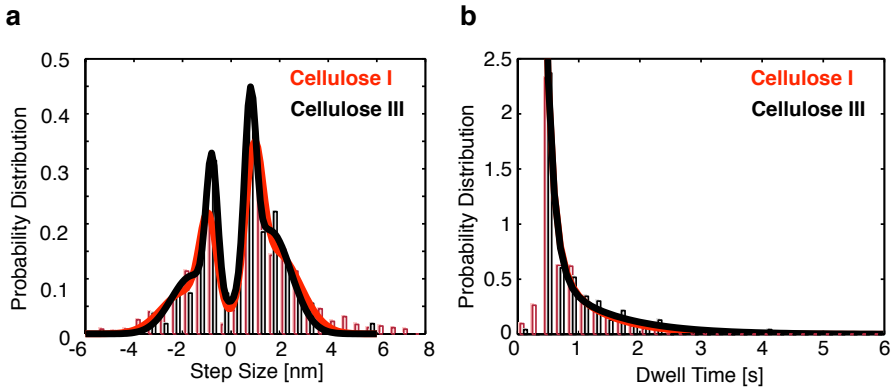

Figure 3.3: **Step size and dwell time distributions** (a) Step size distributions for both cellulose I (N=701) and III (N=108), fit to quadruple gaussian curves based on 1x and 2x fundamental step sizes of 0.94 $\pm$ 0.7 nm (s.d.) and 0.79 $\pm$ 0.6 nm (s.d.), respectively. (b) Dwell distributions fit to double exponential fits with time constants (1/k1 and 1/k2) of 0.12 s and 0.75 s for cellulose I and 0.12 s and 0.98 s for cellulose III. The mean dwell times for cellulose I (N=720) and III (N=116) are 0.75 s $\pm$ 0.02 (s.e.m.) and 0.93 s $\pm$ 0.08 (s.e.m.), respectively.

A closer look at traces with clear structure reveals a base step sizes of 0.94 nm and 0.79 nm for cellulose I and III, respectively. Steps both 1x and 2x the base steps sizes are present in both positive and negative step size distributions for each substrate (Fig. 3.3a). Mean dwell times were evaluated to be 0.75 s $\pm$ 0.02 s (s.e.m.) and 0.93 s $\pm$ 0.08 s for cellulose I and III with persistent dwells as long as six seconds (Fig. 3.3b). The dwell times are consistent with the slow rates generated from double exponential fits in which rate k_2 is 1.342 s^{-1} (0.75 s) and 1.025 s^{-1} (0.98 s) for cellulose I and III, respectively. The first rate k_1 in for each substrate is 8.199 (0.12 s) and 8.020 s^{-1} (0.12 s), respectively. These translocation parameters reveal that the decrease in observed velocity on cellulose III is due to a decrease in step size and an increase in dwell time. Additionally, cellulose III yields a slightly higher prevalence of backwards steps than cellulose I (38.9% versus 35.5%).

It was also noted that initial binding to cellulose III was often slow and unstable. This instability was observed as repeated binding and unbinding until a stable binding event occurred (Fig. 3.4a). This is in comparison to *Tr*Cel7A behavior on cellulose I from both

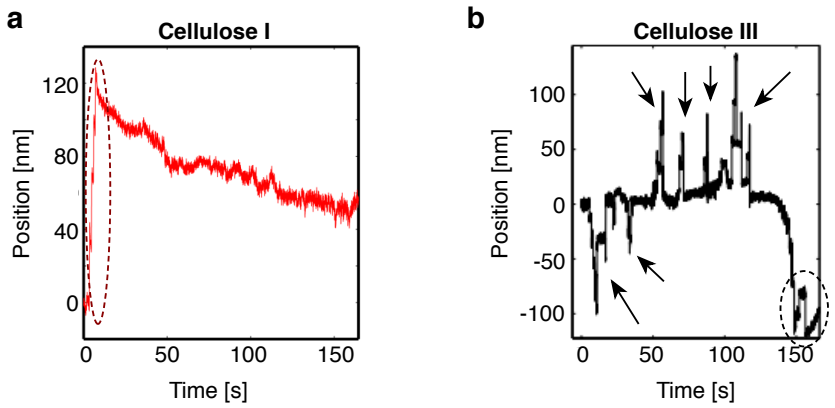

Figure 3.4: **Binding stability** (a) Cellulose I exhibits immediate and stable binding, allowing for force to be applied (shown as a dramatic change in position) when the sample stage is moved, indicated in the area encompassed in the dashed oval. (b) Cellulose III exhibits repeated unstable binding, indicated by arrows, before finally exhibiting stable binding at the end of time trace (dashed oval). In this case the enzyme repeatedly becomes unbound when force is applied by moving the sample stage, causing the position to jump back to baseline.

Cladophora and filter paper in which instability is never seen (Fig. 3.4b).

3.3.2 CBM1 binding

To further investigate the enzyme's behavior, the binding of isolated CBM1 to each substrate was tested. Binding studies reveal complex binding behavior. Binding is typically expected to show slip-bond behavior; when force increases, bond lifetime decreases. However, this is not the case here. While it is difficult to determine an exact number of binding states from the current data, it is clear that there is fluctuation in the bond lifetime with an increase in force up to 15-20 pN (Fig. 3.5). It should be noted that some of the difficulty lies in the fact that while we apply force generally along the fiber axis, it is unknown whether the CBM1 is being pulled towards the reducing or non-reducing end of the fiber, and it is likely that pulling direction reveals differences in binding behavior. In any case, the result is a mean lifetime on *Cladophora* I of 1.13 $\pm$ 0.17 s (SEM), and a possible peak in lifetime (3 s) near 13 pN (Fig. 3.5). *Cladophora* III exhibits a mean lifetime of 0.75 $\pm$

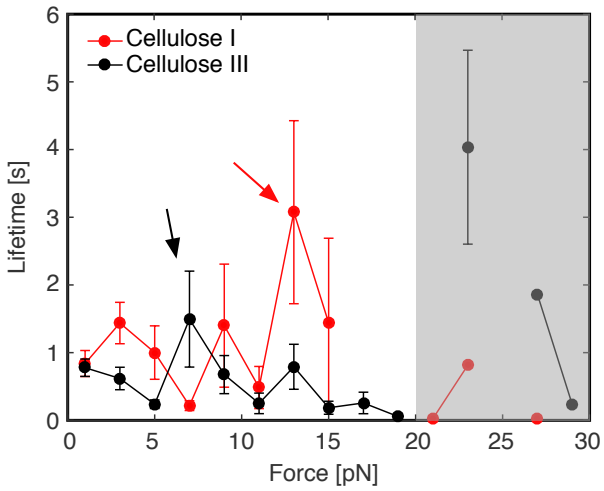

Figure 3.5: **CBM1 bond lifetime** averaged and separated into 2 pN width bins with s.e.m. error bars. Cellulose I (N=109) is in red while cellulose III is in black (N=104). Possible peaks at 13 and 7 pN are indicated with arrows. Data at forces greater than 20 pN is rare and is indicated by a shaded gray box. Error bars represent s.e.m.

0.11 s (SEM) and a possible peak in lifetime (1.5 s) near 7 pN (Fig. 3.5). The shorter bond lifetime on *Cladophora* III supports previous work showing that cellobiohydrolase has a lower affinity for cellulose III [7].

3.4 Discussion

Our results here support previous work showing that while cellulase mixtures may increase hydrolysis rates, the affinity for and the hydrolysis rate of purified *Tr*Cel7A on cellulose III is decreased. The decrease in velocity on cellulose III indicates this lower rate of hydrolysis and we see that this change is due to a decrease in step size, an increase in dwell time, and a slight increase in backwards steps. It seems, therefore, that cellulose III limits the ability of *Tr*Cel7A to catalyze the hydrolysis reaction which allows for the enzyme to translocate, increasing the time between each step.

It is particularly interesting to note, however, that while in Chapter 2 we observe that the presence of the CBM increases the dwell time, thus concluding that the CBM may actually self inhibit translocation to an extent on cellulose I from filter paper [8], this is

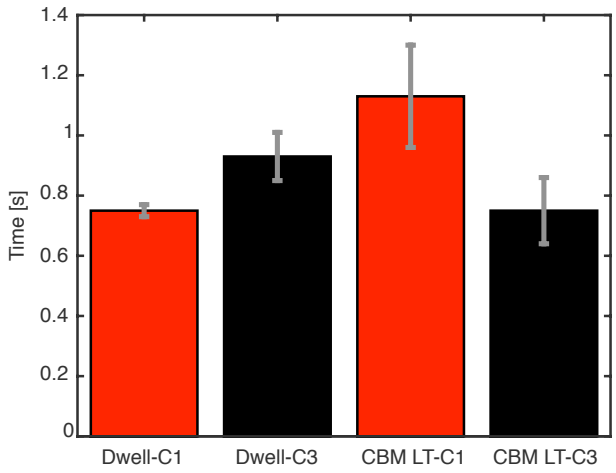

Figure 3.6: **Comparing dwell time and CBM1 bond lifetime.** Average dwell times and CBM1 bond lifetimes for each substrate are plotted for comparison. Dwell time increases for cellulose III, but the CBM1 bond lifetime decreases. Cellulose I and III are notated as C1 or C3, respectively. Error bars indicate s.e.m.

not necessarily the case for cellulose III. We see that the average bond lifetime of CBM1 is shorter than the average dwell time of full motor on cellulose III (Fig. 3.6). This result indicates a decrease in binding affinity for cellulose III and also eliminates the CBM1 as the cause of longer dwell times.

It is also worthy to note the difference in fundamental step size between cellulose I and cellulose III. The crystal structure has changed, but cellulose is still a glucose polymer. Thus, the step size should remain constant at 1 nm. It is speculated that perhaps the difference we see is due to a non-linear component of motion that is not present with cellulose I. For example, if a cellulose strand is more easily dissociated from the crystal, the application of force on the system may peel a strand from the surface causing the hydrolyzing end to be oriented at an angle, creating a linear projection of motion in the x direction that is smaller than the expected 1 nm. An angle of approximately 38 degrees, appropriate given the geometry of our system, would yield a projection of 0.79 nm for a 1 nm distance along the angle.

While our study does not address hydrolysis using cellulase mixtures, it does allow us

to speculate as to how the rate may be increased by a mixture. The structure of cellulose III lends itself to a larger accessible surface area which may also offer more active sites. Additionally, given the lower affiinity for cellulose III, inactive enzymes are able to more easily dissociate from the substrate, reducing self inhibition due to inactive enzymes. If longer segments of cellulose strands are able to be pulled from the surface during translocation, there may also be more opportunity for endoglucanases to catalyze hydrolysis, generating new active sites and removing exocellulase that have become inactive.

Additional studies addressing both the the behavior of other cellulases as well as *Tr*Cel7A in the presence of other cellulases, at the single molecule level, are necessary to help answer some of the outstanding questions concerning the interactions between cellulases that aid in increasing hydrolysis rates in bulk on cellulose III.

3.5 Materials and Methods

3.5.1 Cellulose solution preparation

Cladophora cellulose samples were collected, purified, and provided to us for this study by Prof. Shishir Chundawat (Rutgers University). The samples were prepared according to the methods in Chapter 2. Dried cellulose samples (*Cladophora* I or III) were used to create a heterogeneous cellulose mixture by first mixing the desired cellulose sample in deionized water at a 1 mg mL^{-1} concentration. The mixture is then sonicated for 2 minutes at 50% in a cup sonicator and vortexed for 15 seconds on high. The cellulose, still pretty clumped at this point, is pulled up and down in solution with a 16-gauge syringe for 1-2 minutes before going back on the vortex for 15 seconds. These steps are repeated three times. The resulting mixture is then diluted in a 1:20 ratio by mixing 500 μL of the prepared solution with 500 μL deionized water. This is then stored at 4 °C. When preparing to load a slide, a small sample ($\sim$100 μL) of the stored cellulose mixture is removed from the stock and the cellulose pulled apart by sonicating for 2 minutes at 50% in a cup sonicator and vortexed

for 15 seconds. This solution is what is loaded onto the slide.

3.5.2 *Tr*Cel7A bead functionalization

Bead functionalization with *Tr*Cel7A was achieved as described in Chapter 2. *Tr*Cel7A was purified and provided by Prof. Shishir Chundawat.

3.5.3 CBM1 bead functionalization

CBM1 functionalized beads were created such that, statistically, zero or one CBM1 molecule is bound to each bead. This was determined through serial dilution until a maximum of half the beads bound to cellulose fibers during experiment. To functionalize the beads, 1.09 μm streptavidin beads were mixed with a 1010 bp DNA linker functionalized with a biotin at one end and an anti-His at the other, purified CBM1 in PBS, bovine serum albumin (BSA) at a final concentration of 0.06 mg mL^{-1}, and PBS. The mixture was incubated at room temperature for 45 minutes on a rotator. After incubation, the beads were pelleted at 9250 rpm for 3.5 minutes, the supernatant removed to remove unreacted components, and resuspended in 50 mM acetate buffer (pH 4.9). This was repeated twice. To break up any clumps, the beads were then sonicated in a cup sonicator for 2 minutes at 20%. CBM1 was expressed and purified by Prof. Shishir Chundawat who is currently at Rutgers University.

3.5.4 Slide preparation

Slides are prepared by creating a 10-15 μL volume flow cell using an etched coverslip and double-sided sticky tape. A cellulose solution (*Cladophora* I or III) is then added to the flow cell and allowed to dry out in an oven at $\sim$95 °C for an hour, non-specifically binding the cellulose to the slide surface. The surface is then blocked with 10 mg mL^{-1} BSA in acetate buffer for 10 minutes to prevent non-specific sticking of the beads. Finally, the bead

solution is loaded into the slide and the slide sealed.

3.5.5 Data acquisition and analysis - motility studies

Motility assays were performed and the data analyzed as described in the Materials and Methods of Chapter 2.

3.5.6 Data acquisition and analysis - binding studies

Data was acquired for motility assays (full *Tr*Cel7A) as described in Chapter 2. CBM1 functionalized beads were trapped using a 1064-nm laser. After calibration, the bead was actively placed on a cellulose fiber roughly running along the axis of the microscope stage. Upon binding, the bead was centered, acquisition started, and a force applied to the tethered bead by stepping the piezo stage along the axis of the fiber. With force applied, the position is the bead is held until rupture. Once a tether is ruptured, it is sometimes possible to tether the bead to the fiber again, in which case, the same method of force application is applied while data acquisition continues.

Data were collected at a 3-kHz sampling frequency and then filtered with a 10 point exponential moving average before analysis. Custom Matlab codes were then used determine the rupture forces and the bond lifetimes of full ruptures.

3.6 Acknkowledgements

This work was completed through a collaboration with Prof. Shishir Chundawat (Rutgers) who provided us with enzyme and substrate samples. This work was supported by Singapore-MIT Alliance for Research and Technology - BioSyM, NSF (1330792), and GAANN (P200A090323). The work by Prof. Chundawat was also partially supported by Rutgers University, the National Science Foundation Grant Number 1236120 (CBET - Energy for Sustainability), and the Great Lakes Bioenergy Research Center (DE-FC02-

07ER64494).

3.7 Bibliography

[1] Shishir P S Chundawat, Giovanni Bellesia, Nirmal Uppugundla, Leonardo da Costa Sousa, Dahai Gao, Albert M Cheh, Umesh P Agarwal, Christopher M Bianchetti, George N Phillips, Jr, Paul Langan, Venkatesh Balan, S Gnanakaran, and Bruce E Dale. Restructuring the crystalline cellulose hydrogen bond network enhances its depolymerization rate. *J Am Chem Soc*, 133(29):11163–74, Jul 2011.

[2] Y-H Percival Zhang, Jingbiao Cui, Lee R Lynd, Lana R Kuang, et al. A transition from cellulose swelling to cellulose dissolution by o-phosphoric acid: evidence from enzymatic hydrolysis and supramolecular structure. *Biomacromolecules*, 7(2):644–648, 2006.

[3] Noppadon Sathitsuksanoh, Zhiguang Zhu, Sungsool Wi, and Y-H Percival Zhang. Cellulose solvent-based biomass pretreatment breaks highly ordered hydrogen bonds in cellulose fibers of switchgrass. *Biotechnology and bioengineering*, 108(3):521–529, 2011.

[4] Joseph A Rollin, Zhiguang Zhu, Noppadon Sathitsuksanoh, and Y-H Percival Zhang. Increasing cellulose accessibility is more important than removing lignin: a comparison of cellulose solvent-based lignocellulose fractionation and soaking in aqueous ammonia. *Biotechnol Bioeng*, 108(1):22–30, Jan 2011.

[5] Masahisa Wada, Henri Chanzy, Yoshiharu Nishiyama, and Paul Langan. Cellulose III(i) crystal structure and hydrogen bonding by synchrotron X-ray and neutron fiber diffraction. *Macromolecules*, 37(23):8548–8555, 2004.

[6] Kiyohiko Igarashi, Masahisa Wada, and Masahiro Samejima. Activation of crystalline cellulose to cellulose III(i) results in efficient hydrolysis by cellobiohydrolase. *FEBS J*, 274(7):1785–92, Apr 2007.

[7] Dahai Gao, Shishir PS Chundawat, Anurag Sethi, Venkatesh Balan, S Gnanakaran, and Bruce E Dale. Increased enzyme binding to substrate is not necessary for more efficient cellulose hydrolysis. *Proceedings of the National Academy of Sciences*, 110(27):10922–10927, 2013.

[8] Sonia K Brady, Sarangapani Sreelatha, Yinnian Feng, Shishir P S Chundawat, and Matthew J Lang. Cellobiohydrolase 1 from Trichoderma reesei degrades cellulose in single cellobiose steps. *Nat Commun*, 6:10149, Dec 2015.

Chapter 4

BACTERIAL CELLULOSE SYNTHASES A AND B (BcsAB) ELONGATE CELLULOSE IN A BIOCHEMICALLY LIMITED PROCESS

4.1 Summary

Cellulose is of great interest to the healthcare industry given its prevalence in biofilms and the huge health implications of biofilm derived infections. As a result and in an effort to develop effective biofilm prevention and remediation procedures, researchers are seeking to understand the underlying mechanism of bacterial cellulose synthesis. Cellulose synthesis is a complex process that presents challenges for *in vitro* studies as it is a transmembrane system. However, the development of amphipol and nanodisc embedded BcsAB constructs has opened a path to the *in vitro* study of this catalytic complex. Here, we utilize these constructs in optical trapping assays to characterize BcsAB behavior under force and reveal a biochemically limited system that exhibits structured elongation at lengths greater than the elongation length of a single glucose unit and rates similar to single molecule cellulose degradation by *Tr*Cel7A.

4.2 Introduction

Cellulose, as described in the Introduction (section 1.2.1), often takes the form of highly stable micro or macro-fibril crystalline structures that help maintain the structural integrity of cell walls. However, it is also produced by lower order organisms as single strand or small amorphous bundles as part of the cell's extracellular secretion. Often this cellulose becomes the foundation of biofilms [1, 2, 3]. Given the health implications of biofilms as antibiotic resistant environments for bacteria and the prevalence of biofilms in everything from water treatment facilities, to food processing plants, to catheter tubes, other medical devices, and dental plaques, there is a significant effort to understand how this cellulose is

produced.

Cellulose, and other polysaccharide polymers, are produced by glycosyltransferases (GT), transmembrane proteins that simultaneously synthesize the polymer and transport the polymer across the cell membrane [4]. In bacteria, cellulose is produced by bacterial cellulose synthase (Bcs), a multicomponent complex, usually consisting of at least five domains: BcsA, B, C, D, and Z as described in Chapter 1 (Fig. 1.5a). BcsA is the catalytic domain that synthesizes cellulose from UDP activated glucose (UDP-glucose) and extends from the cytoplasm, through the inner membrane, into the periplasm [5]. The synthesized cellulose polymer then encounters BcsB, a protein residing in the periplasm but anchored in the inner membrane. While only 41 amino acids of the BcsB C-terminus are required for BcsA to be catalytically active [6], it is thought that BcsB may help guide the cellulose polymer across the periplasm to BcsC, which extends from the periplasm across the outer membrane and is thought to facilitate transport and the assembly of more complex cellulose structures. The other domains, BcsD and Z, are periplasmic proteins but their functions are unclear and they are not necessary for BcsA activity [7].

Recent work by the Zimmer lab at the University of Virginia has elegantly described the mechanism of cellulose synthesis and translocation by *Escherichia coli* expressed BcsAB from *Rhodobacter sphaeroides* [6, 5, 8, 9]. They have shown that synthesis is dependent upon ion concentration, most notably Mg^{2+}, c-di-GMP, and activated UDP-glucose. c-di-GMP is a molecule that regulates synthesis by opening a 'gating loop' that allows UDP-glucose access to the active site upon binding (Fig. 1.5b). It has additionally been observed that free UDP, but not substrate, can cause inhibition of the synthesis reaction [6]. However, there are still questions to be answered in regards to the kinetics, force response, and the mechanism of BcsAB activity.

Single molecule experiments provide the perfect opportunity to fill in the gaps in our understanding of BcsAB behavior, however, one hurdle in doing so is the *in vitro* isolation of active BcsAB as it is a transmembrane protein complex. BcsAB can be stabilized

without detergent using two methods. The first is by embedding the protein in nanodiscs (ND), small (∼10 nm) phospholipid discs stabilized by membrane scaffold proteins, providing an environment similar to the protein's native membrane environment. These NDs have previously been used in the reconstitution of the SecYEG complex [10]. The Zimmer lab has also already demonstrated the use of NDs with BcsAB in work published in 2013 [6]. Another method is the use of amphipols, amphiphilic polymers that stabilize the transmembrane portion of BcsAB and have previously been shown to stabilize other membrane proteins [11, 12]. Both of these constructs are stable once formed and allow for the isolation of single protein complexes which is essential for experiments that are single molecule in nature. We test both of these constructs and provide preliminary data concerning the truncated S678 construct in amphipols. This construct contains BcsA and a truncated BcsB which only includes the transmembrane anchor of BcsB. This construct has been found to be the minimal active construct [6].

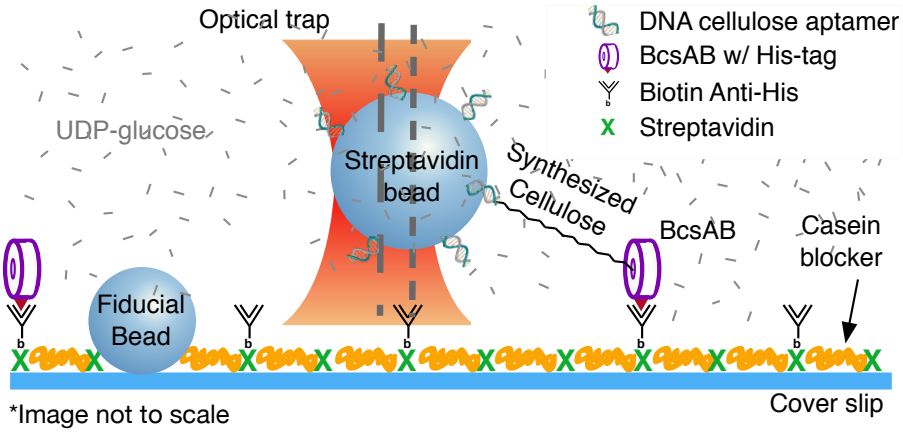

Figure 4.1: **Bcs assay schematic** A schematic of the BcsAB cellulose synthesis assay tracks motility through a tether created by attaching BcsAB to the surface and then binding a 1.25- μm streptavidin bead held in an optical trap to the pre-synthesized cellulose produced by BcsAB. Stationary fiducial beads serve to compensate for drift.

This work focuses on optical trapping based assays (Fig. 4.1) carried out on both full length BcsAB complexes. The proteins are tethered to the surface on one end via the His tag on the C-terminus of BcsA and to a bead functionalized with cellulose specific DNA

aptamer by means of the synthesized cellulose strand exiting BcsA. It should be noted that while all constructs contain a His-tag on BcsA, the ND construct contains an additional His-tag on the ND itself. Multiple His-tags complicates data analysis as it opens the possibility of an additional population of results since we can bind to either His-tag or both. However, a separate population has not been observed with the current data. The work seeks to observe translocation by single BcsAB complexes and characterize its behavior using mechanical parameters such as translocation rates and stall forces.

4.3 Results

As cellulose is synthesized the cellulose strand will elongate. In our assay, we apply low assisting force at the beginning of data acquisition to offset the bead from the center of the trap allowing the bead to move back towards the center of the trap as cellulose is synthesized. Note that due to the assay geometry, all forces are assisting forces and work towards pulling synthesized cellulose through BcsA's transmembrane pore. Synthesis was first qualitatively visualized by observing the tether length (how far a bead can move from it's tethering point - directly proportional to the length of cellulose) over time. The initial tether length is variable as the cellulose specific DNA aptamer is not specific for cellulose chain ends, however, over the course of an hour, tethers were seen to elongate from 100-200 nm up to a couple micrometers, translating to a velocity of roughly 0.2-0.5 nm s^{-1}. This confirmed construct activity and allowed for the development of the single molecule assay.

The synthesis rate of cellulose by BcsAB at 21°C is not well defined, however, it is predicted to be on the order of 90 UDP molecules s^{-1} (or $\sim$45 nm s^{-1}) at 37°C using real time monitoring of NADH oxidation as a measure of polymer elongation when BcsAB is coupled with pyruvate kinase (PK) and lactate dehydrogenase (LDH) activity [6]. As a result of the rather slow and unknown rate, small (0.75 μm) fiducial beads were incorporated into the assay to allow for drift tracking and adjustment during analysis as detailed in

Chapter 2 for *Tr*Cel7A.

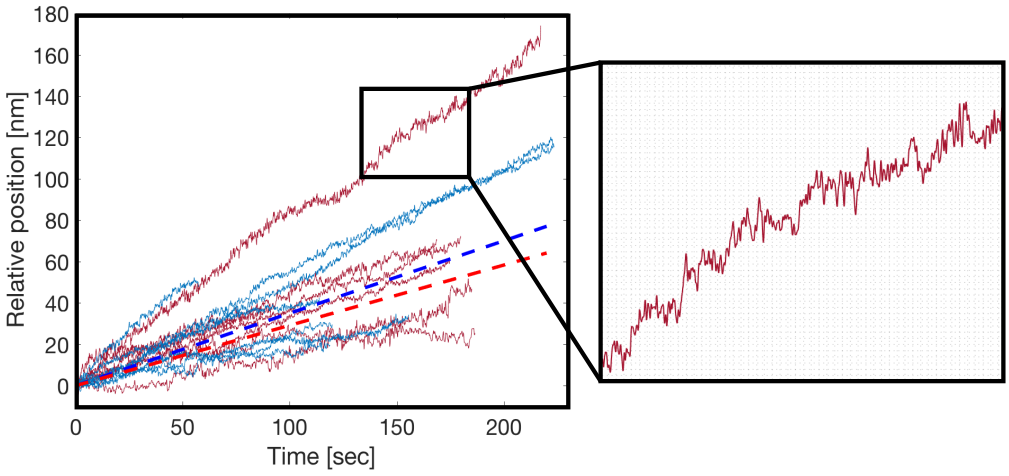

Figure 4.2: **Sample traces of cellulose elongation by BcsAB** exhibit a range of velocities with a weighted average of 0.35 nm s^{-1} $\pm$ 0.19 (s.d.) and 0.29 nm s^{-1} $\pm$ 0.18 (s.d.) for full length amphipol (blue) and ND (red) constructs, respectively. The weighted averages are reppresented by the dashed lines. The averages are representative of 54 traces from 28 separate beads (amphipol) and 36 traces from 22 separate beads (ND) at 21°C. The inset reveals an enlarged region of one trace highlighting the step-like structure that is visible in some traces.

A total of 90 traces were collected from the two full length constructs (amphipol - 54 traces from 28 separate beads, ND - 36 traces from 22 separate beads). The result is a collection of time traces with velocities ranging from 0.07 to 0.9 nm s^{-1}, as seen in Figure 4.2 with a combined average weighted velocity of 0.32 nm s^{-1} (0.35 nm s^{-1} $\pm$ 0.03 (s.e.m.) and 0.29 nm s^{-1} $\pm$ 0.03 (s.e.m.) for amphipol and ND constructs, respectively). Further analysis, as shown later, reveals that the small difference in velocities between the constructs is due to the presence of a couple higher force (low velocity) traces in the ND data. The agreement of the velocities (and spread) between constructs validates that the stabilization method (amphipol vs ND) does not affect BcsAB activity. A histogram of trace velocities (Fig. 4.3) also shows strong consistency in the distribution of velocities suggesting that the His-tag by which a tether is formed on the ND construct does not affect apparent velocity of activity.

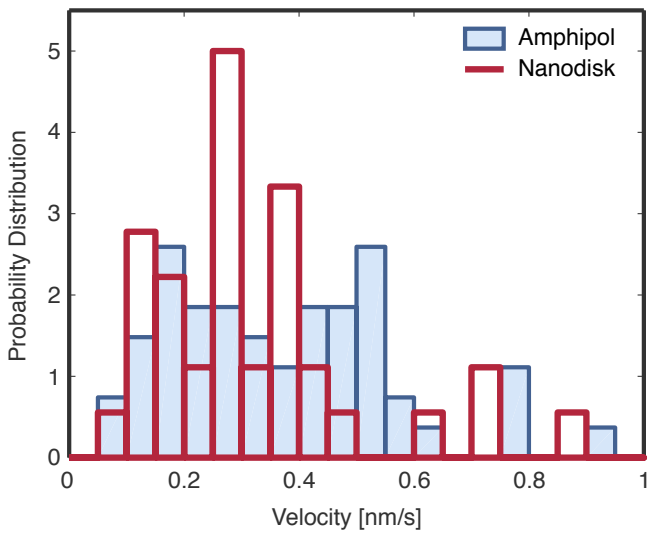

Figure 4.3: **A velocity histogram of cellulose elongation by BcsAB** showing the consistent spread of velocities between amphipol and ND constructs.

Structure within the traces is present but somewhat inconsistent. Analysis of traces using a point to point analysis reveals visible structure in 43% (amphipol) to 57% (ND) of traces. Further analysis that generates the spatial frequency spectra of structured traces reveals varying characteristic distances from 2.9-13 nm (amphipol - 4.0, 6.8, and 13.2 nm; ND - 2.9 and 3.9 nm) as seen in Fig. 4.4. This structure is somewhat surprising as cellulose has been extensively biochemically characterized and shown to be elongated one glucose unit (0.5 nm) at a time [9]. As 0.5 nm is beyond our reliable resolution, it was not expected to able to resolve 0.5 nm structure (which we don't), however, the source of the larger observed structure observed here is unclear.

By considering the effect of assisting load on trace velocity, we note the presence of average trace forces up to 5.7 pN (amphipol) and 6.5 pN (ND) and a stable and consistent velocity at low forces. If local forces and associated velocities are found using a 5 second moving window along each trace (as done in Chapter 2), we extend our force range up to 8 pN (ND). By combining amphipol and ND data, a clear force velocity relationship is generated (Fig. 4.5). This relationship can be fit to a general Boltzmann force velocity

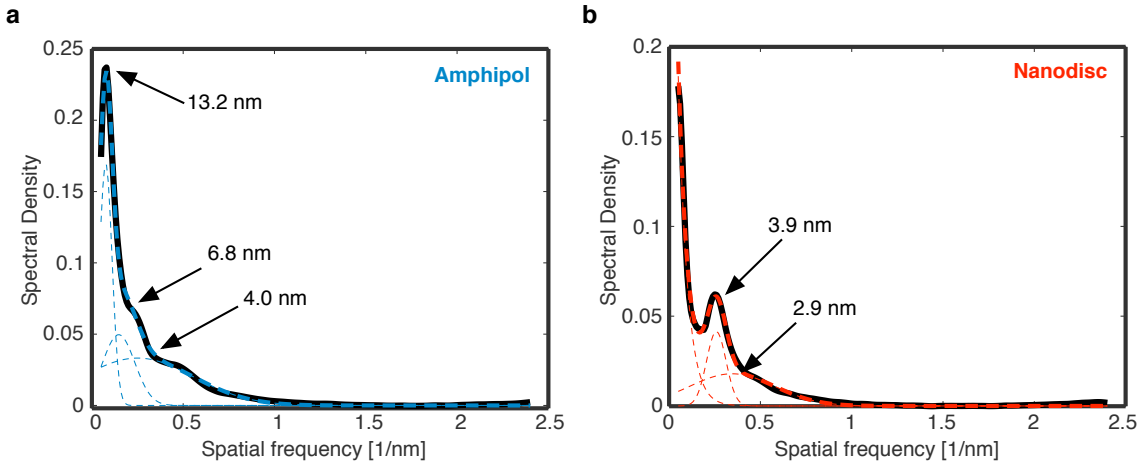

Figure 4.4: **Spatial frequency spectra of cellulose elongation traces** by amphipols (a) reveals structure corresponding to 4.0, 6.8, and 13.2 nm in lengths while that of the ND construct (b) reveals structures of 2.9 and 3.9 nm in length. The spectra are sums of the spectra of structured traces ($\sim$50% of all traces) for each of the full length constructs. These sums have been adjusted to a baseline defined by that of red noise.

relationship like that used to develop the one-parameter force-velocity fit used by Wang *et al.* for RNA polymerase [13].

$$V(F) = \frac{V_o(1+A)}{1+A\exp(F\delta/k_BT)} \tag{4.1}$$

In this model V_o is the no force velocity, A is a constant that indicates whether the process is biochemically ($A << 1$) or mechanically ($A \geq 1$) limited, and δ is a characteristic distance. Additionally, $F_{1/2}$, the force at which the velocity is half the maximum velocity, the stall force, can be approximated to be the following.

$$F_{1/2} = \frac{k_BT}{\delta}\ln(A^{-1}) \tag{4.2}$$

In applying this fit, our data yields a V_o of 0.32 nm s^{-1}, consistent with the weighted average trace velocity. This is expected given the extremely flat nature of the force-velocity curve at low forces. This low force behavior also indicates a highly biochemically limited process, as is confirmed with the generation of a very small A (2.22 x 10^{-8}). As force

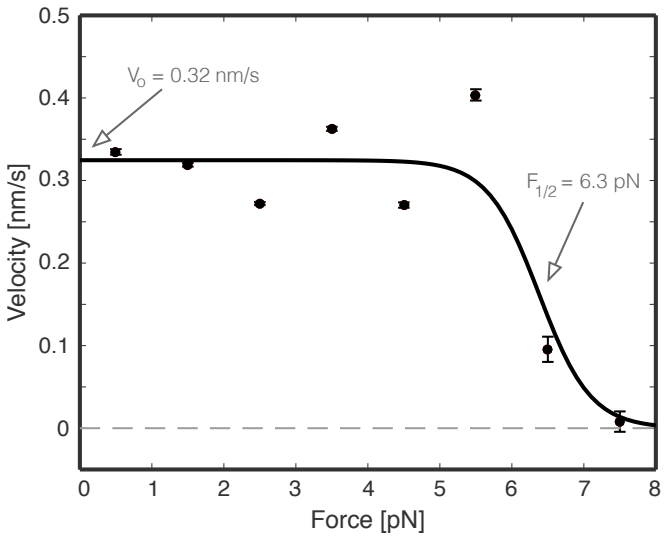

Figure 4.5: **Force velocity curve** fit to a Boltzmann model reveals a biochemically limited process (flat shape at low forces) with a zero force velocity, V_o, or 0.32 nm s^{-1} and a stall force, $F_{1/2}$, or 6.3 pN. The data in this plot represents local force data and the associated velocities as calculated by finding the average of each over a 5 second moving window. The data was then averaging in 1 pN force bins. The error bars represent standard error on the mean (s.e.m.).

increases, the fit reveals a steep decrease in velocity with a $F_{1/2}$ of 6.3 pN. Additionally, we note a characteristic distance, δ, of $\sim$11 nm. This is consistent with some of the larger observed structure, particularly in amphipol constructs and is consistent with the length of the transmembrane pore that extends through BcsA, however, the exact nature of this δ is unknown.

In addition to the characterization of full length BcsAB, preliminary studies on S678 (amphipol) have been done. A total of 7 traces from 5 separate beads yield time traces and force velocity characteristics similar that of full length BcsAB (Fig. 4.6a) with a weighted average velocity of 0.4 nm s^{-1}, although the spread of velocities is large and N is small. Data on the characteristic structure is minimal given the size of the data set but evidence of structure at $\sim$8.5 and 12.8 nm is present (Fig. 4.6b). While the data is currently preliminary, the activity of S678 appears to be consistent with that of full length BcsAB, as expected. Further studies and increasing the size of the data set will reveal any differences in the

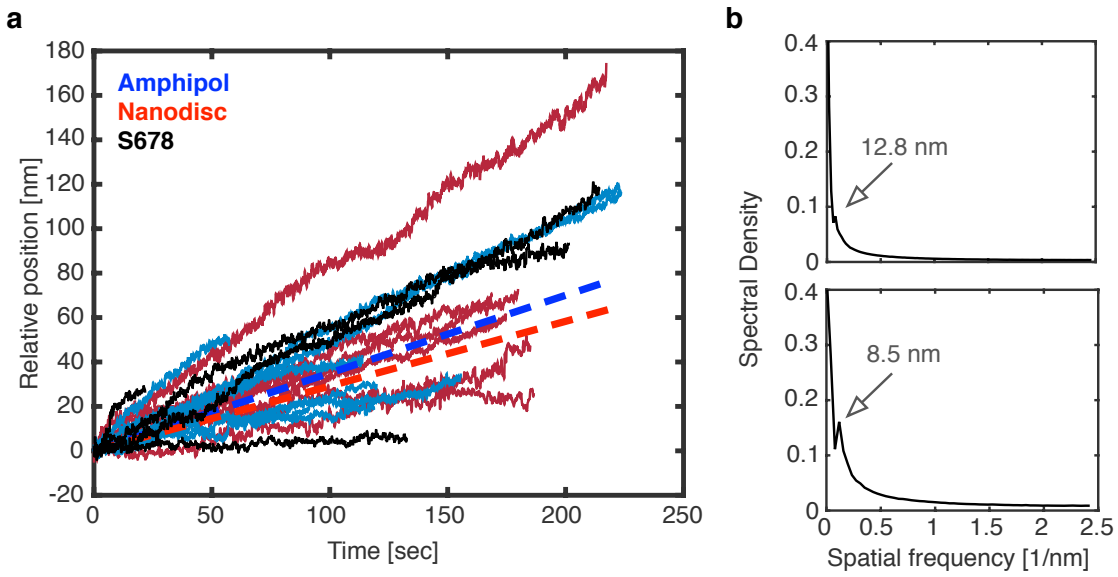

Figure 4.6: **Preliminary S678 data** yields sample traces (a) consistent with traces from each full length construct. Evidence of structured cellulose elongation is also evident in S678 spatial frequency spectra (b) in which large with lengths of 8.5 and 12.8 nm can be seen. These spectra are the spectra from individual traces and the baseline has not been adjusted to that of red noise.

construct's behavior and could shed light on the nature of the observed structure in collected traces.

4.4 Discussion

Here we observe a fully functional *in vitro* BcsAB complex stabilized by two different methods. Using these methods, cellulose elongation is seen to occur at a rate of 0.32 nm s^{-1}. This is particularly interesting due to its similarity to the rate of cellulose degradation as discussed in Chapters 2 and 3. While the source(s) of the observed structure in the traces is unclear, it is conceivable that there is a weak interaction between the synthesized cellulose strand and a location external to the pore on BcsA or BcsB that, *in vivo*, help guide the synthesized strand towards BcsC and the outer membrane. It is also curious that the larger structure is consistent with the length of the BcsA pore. Although the inconsistency and variability in the structure coupled with Zimmer's previous work [5, 8, 9] makes it un-

likely that the structure is due to cellulose slipping or being pulled through the pore. More data on full length, truncated, and mutated constructs are necessary to fully understand the observed behavior.

Perhaps the most insightful result, however, is the force velocity curve. The curve reveals a biochemically limited system that is blind to force up to a stall force of 6.3 pN, above which activity quickly drops to zero. Noting that our assay applies an assisting load in all cases allows for speculation regarding the biological importance of this stall force. Synthesized cellulose must somehow be accurately transported across the periplasm to BcsC for translocation to the outside of the cell. There are some theories that suggest BcsZ can hydrolyze synthesized cellulose in the periplasm as a way to assist in the regulation of cellulose transport across the periplasm and run remediation efforts if the process goes awry. Similarly, perhaps, the stall force acts as a switch such that if too much tension is stored in the synthesized cellulose BcsA can recognize that as a sign there is a problem (ie. cellulose twisted, misguided, or building up in the periplasmic space) and can stop production.

Although more data must be collected and the effect of controls such as limited UDP-glucose and c-di-GMP observed, the information gained here is exciting and provides a platform from which more complex single molecule assays can be developed. For example, the development of a system that also includes BcsC, thus allowing, for the first time, a fully reconstituted *in vitro* system for cellulose synthesis and translocation that could provide unprecedented clarity in the understanding of the Bcs system. This work also makes accessible the use of amphipol and nanodisc stabilization methods in the development of single molecule assays with other membrane bound proteins.

4.5 Materials and Methods

All protein preparation including expression, purification, and integration into amphipols and nanodiscs was completed in the lab of Jochen Zimmer and provided to us as

complete constructs. Incomplete synthesis buffer has a final composition of 25 mM sodium phosphate (pH 7.5), 5 mM cellobiose, 10% glycerol, and 20 mM $MgCl_2$. Complete synthesis buffer also includes 30 μM cyclic diguanylic acid (c-di-GMP), 5 mM UDP-glucose, an additional 5 mM cellobiose for a final concentration of 10 mM cellobiose, and 0.5 mg mL^{-1} BSA to prevent sticking.

4.5.1 Slide Preparation

Slides were prepared using flow cells created with a slide, KOH etched coverslip, and double sided tape with a volume of approximately 15 μL. The slide is loaded with a Cy3-streptavidin (Sigma - S6402, $\sim$1 mg mL^{-1} protein) and polystyrene bead (0.75 μm) mixture in PBS (pH 7.4) such that the final dilution of each is 1:2000 from stock and incubated for 15 minutes. The slide is then washed and incubated (15 minutes) with 1 mg/mL blotting-grade blocker (casien) in PBS to prevent non-specific binding of anti-His to the coverslip surface, followed by an incubation with biotinylated anti-His antibody at a 1:100 dilution in PBS (final concentration of 5 μg mL^{-1}). To remove excess antibody, the slide is washed with 5 mg/mL BSA in Tris-HCl (20 mM, pH7). The protein is then added and the slide incubated (20 minutes) to allow BcsAB binding to the antibodies. BcsAB is diluted to 1:2000 from 8 μM stock and 1:50,000 from 3 μM stock in Tris-HCl (20 mM, pH 7) for amphipol and nanodisc constructs, respectively. The truncated S678 amphipol construct is diluted 1:1500 from 6 μM stock. Unbound protein is then removed by washing the flow cell with 5 mg mL^{-1} BSA in Tris-HCl (20 mM, pH 7). Finally, tethers are passively formed by incubating with strepatavidin beads functionalized with cellulose specific DNA aptamper [14] in incomplete synthesis buffer (with a 0.1 mg mL^{-1} final concentration of BSA) that will bind to the synthesized cellulose strand extending from the end of the protein. After incubating for 20 minutes, most untethered beads are removed and synthesis initiated by washing the slide with complete synthesis buffer. In this procedure all incubations are carried out at room temperature in a humidity chamber. The slide can then be sealed with

nail polish and is ready for testing. It is noted that there is a large difference in the dilutions, and thus, final concentrations of amphipol versus nanodisc constructs. These dilutions were determined using serial dilution such that approximately 2-4 passive tethers are formed per field of view after incubation. It was found that this coverage allowed for a combination of minimum non-specific binding to the surface and a maximum number of tethers. Also not that complete synthesis buffer refers to a buffer containing 25 mM sodium phosphate (pH 7.5), 100 mM NaCl, 5 mM cellobiose, 10% glycerol, 20 mM $MgCl_2$, 30 μM c-di-GMP, and 5 mM UDP-glucose. Incomplete synthesis buffer is missing UDP-glucose and c-di-GMP.

4.5.2 Data Acquisition

Immediately after the addition of complete synthesis buffer to the flow cell, the slide is loaded onto a custom inverted microscope outfitted with an optical trap. A free bead (1.09 μm) is then found, trapped, and calibrated using a fifth order calibration routine, the results of which are subsequently used to find the trap stiffness. This free bead is calibrated at a z-position close to that which will be used for beads during data acquisition and with a cutoff frequency of 30 kHz. After calibration, the bead is released and a tethered bead (1.09 μm) within the same field of view as a firmly stuck fiducial bead (0.75 μm) is found. The bead is centered using a piezo stage based centering routine and the trap is turned on. Upon centering, data acquisition is initiated for both video tracking of the fiducial bead (using an Andor iXon camera) and the tethered bead using PSDs. When data acquisition has been initiated, the stage is moved at 2 μm s^{-1} in 50 nm steps until the bead is 0.5-1.5 V from the trap center to apply tension to the tether, generating an assisting load on the enzyme. Data is acquired at 3000 scans s^{-1} for the tethered bead with an antialias filter cut-off of 1.5 kHz. The fiducial bead position is tracked at $\sim$4 Hz using the Andor iXon camera. Acquisition is set to be limited to a maximum of approximately 4 minutes.

4.5.3 Data Analysis

Given the low cellulose synthesis rate of BcsAB, it was necessary that instrumental drift be removed from the data. To do this, smaller fiducial beads (0.75 μm) were recorded using the Andor iXon camera to determine the instrumental drift. The fiducial bead position over time was determined using a cross correlation video tracking algorithm. The resulting time versus position trace was then smoothed and subtracted from the larger tethered bead (1.09 μm) position data acquired using a PSDs. This results in up to 95% of instrumental drift, with an average removal of 81%.

Analysis of the data was then carried out using custom Matlab scripts. Tethered bead position at nanometer resolution and picoNewton forces was found using the calibration and trap stiffness. All position data was initially decimated to 60 Hz. Additionally, all position data used in analysis was corrected for drift and then rotated to be along the x-axis for easier computation. A drift correction was not applied to force data as the force is dependent upon the distance of the bead from the center of the trap.

Average trace velocities were calculated using a linear fit to the entire time trace while average trace force was calculated by finding the mean force for the trace. Weighted average trace velocities and forces were weighted based on the time length of the trace. These were used for comparison with local force-velocities. Local force and velocity were found by calculating the mean force and the slope of a moving five second window. Point to point analysis was conducted using a 0.5 nm bin size and then used to generate frequency power spectra. A power spectra sum was generated by adding all generated spectra that revealed structure ($\sim$50% of collected traces) and used to determine if the structure collapsed to one or more signature peaks.

4.6 Acknowledgements

This work was completed in collaboration with Prof. Jochen Zimmer at the University of Virginia who suppled us with all BcsAB constructs, buffer components, and the expertise on Bcs systems that made this work possible. The single molecule experiments at Vanderbilt were supported by Singapore-MIT Alliance for Research and Technology - BioSyM, NSF (1330792), and GAANN (P200A090323).

4.7 Bibliography

[1] Courtney E Jahn, Dija A Selimi, Jeri D Barak, and Amy O Charkowski. The Dickeya dadantii biofilm matrix consists of cellulose nanofibres, and is an emergent property dependent upon the type III secretion system and the cellulose synthesis operon. *Microbiology*, 157(Pt 10):2733–44, Oct 2011.

[2] Oscar A McCrate, Xiaoxue Zhou, Courtney Reichhardt, and Lynette Cegelski. Sum of the parts: composition and architecture of the bacterial extracellular matrix. *J Mol Biol*, 425(22):4286–94, Nov 2013.

[3] Diego O Serra, Anja M Richter, and Regine Hengge. Cellulose as an architectural element in spatially structured Escherichia coli biofilms. *J Bacteriol*, 195(24):5540–54, Dec 2013.

[4] Yunchen Bi, Caitlin Hubbard, Pallinti Purushotham, and Jochen Zimmer. Insights into the structure and function of membrane-integrated processive glycosyltransferases. *Curr Opin Struct Biol*, 34:78–86, Oct 2015.

[5] Jacob L W Morgan, Joanna Strumillo, and Jochen Zimmer. Crystallographic snapshot of cellulose synthesis and membrane translocation. *Nature*, 493(7431):181–6, Jan 2013.

[6] Okako Omadjela, Adishesh Narahari, Joanna Strumillo, Hugo Mélida, Olga Mazur, Vincent Bulone, and Jochen Zimmer. BcsA and BcsB form the catalytically active core of bacterial cellulose synthase sufficient for in vitro cellulose synthesis. *Proc Natl Acad Sci U S A*, 110(44):17856–61, Oct 2013.

[7] Olga Mazur and Jochen Zimmer. Apo- and cellopentaose-bound structures of the bacterial cellulose synthase subunit BcsZ. *J Biol Chem*, 286(20):17601–6, May 2011.

[8] Jacob L W Morgan, Joshua T McNamara, and Jochen Zimmer. Mechanism of activation of bacterial cellulose synthase by cyclic di-GMP. *Nat Struct Mol Biol*, 21(5):489–96, May 2014.

[9] Jacob L W Morgan, Joshua T McNamara, Michael Fischer, Jamie Rich, Hong-Ming Chen, Stephen G Withers, and Jochen Zimmer. Observing cellulose biosynthesis and membrane translocation in crystallo. *Nature*, 531(7594):329–34, Mar 2016.

[10] Meriem Alami, Kush Dalal, Barbara Lelj-Garolla, Stephen G Sligar, and Franck Duong. Nanodiscs unravel the interaction between the SecYEG channel and its cytosolic partner SecA. *The EMBO journal*, 26(8):1995–2004, 2007.

[11] Aleksandr Sverzhinsky, Shuo Qian, Lin Yang, Marc Allaire, Isabel Moraes, Dewang Ma, Jacqueline W Chung, Manuela Zoonens, Jean-Luc Popot, and James W Coulton. Amphipol-trapped ExbB-ExbD membrane protein complex from Escherichia coli: a biochemical and structural case study. *J Membr Biol*, 247(9-10):1005–18, Oct 2014.

[12] Kevin W Huynh, Matthew R Cohen, and Vera Y Moiseenkova-Bell. Application of amphipols for structure–functional analysis of TRP channels. *The Journal of membrane biology*, 247(9-10):843–851, 2014.

[13] M D Wang, M J Schnitzer, H Yin, R Landick, J Gelles, and S M Block. Force and velocity measured for single molecules of RNA polymerase. *Science*, 282(5390):902–7, Oct 1998.

[14] Qing Yang, Irwin J Goldstein, Houng-Yau Mei, and David R Engelke. DNA ligands that bind tightly and selectively to cellobiose. *Proceedings of the National Academy of Sciences*, 95(10):5462–5467, 1998.

Chapter 5

THE NESPRIN-CYTOSKELETON INTERFACE PROBED DIRECTLY ON SINGLE NUCLEI IS A MECHANICALLY RICH SYSTEM AND SUBJECT TO NUCLEAR HISTORY

*This chapter is adapted from Balikov, Brady, et al, "The nesprin-cytoskeleton interface probed directly on single nuclei is a mechanically rich system and subject to nuclear history" *Nucleus* (submitted 12-14-2016 and under revision at the time of submission of this dissertation) by permission granted under the Taylor & Francis copyright guidelines.

5.1 Summary

The cytoskeleton provides structure and plays an important role in cellular function such as migration, resisting compression forces and transport. The cytoskeleton also reacts to physical cues such as fluid shear stress or extracellular matrix remodeling by reorganizing filament associations, most commonly focal adhesions and cell-cell cadherin junctions. These mechanical stimuli can result in genome-level changes, and the physical connection of the cytoskeleton to the nucleus provides an optimal conduit for signal transduction by interfacing with nuclear envelope proteins, called nesprins, within the LINC (linker of the nucleus to the cytoskeleton) complex. Using single-molecule on single nuclei assays, we report that the nesprin-cytoskeleton interface is highly sensitive to force magnitude and direction depending on whether cells are historically interfaced with the matrix or with cell aggregates. Application of $\sim$10-30 pN forces to these nesprin linkages yield structural transitions, with a base transition size of 5-6 nm, which are speculated to be associated with partial unfoldings of the spectrin domains of the nesprins and/or structural changes of histones within the nucleus.

5.2 Introduction

Cells are very sensitive to physical forces. A quintessential example of this is endothelial cells delineating between laminar and turbulent flow [1, 2]. Depending on the flow profile, endothelial cells are able to respond quickly and reprogram their entire protein expression profile [3, 4]. Mechanistic studies investigating which signaling cascades and mechanical connections are responsible for phenotype change were conducted by directly probing the cell surface and the associated cell-cell and cell-matrix interfaces [5, 6]. Because cytoskeletal elements conduct the majority of physical inputs on the cell, it is critical to study how these forces propagate within the cell, particularly as they propagate to a termination point such as the nucleus.

Much of the research in mechanotransduction has focused on the plasma membrane where cell-cell adhesion complexes and focal adhesions serve as mechanosensors [7]. Similarly, proteins at each end of cytoskeletal filaments serve not only as anchors for filaments but also as mechanosensors [8]. However, while interest in cytoskeletal anchoring at the nuclear envelope has developed over the past decade, it remains challenging to study because accessing the nuclear-cytoskeletal interface is difficult.

The first demonstration of a physical linkage between the nucleus and the plasma membrane represented a seminal shift in defining the mechanism by which the cell's external environment physically connects to organelles deep within the cytoplasm [9]. In endothelial cells, shear stress applied to cells has been shown to displace cytoskeletal elements (e.g. actin, vimentin) and nodal structures (e.g. focal adhesions, cadherin junctions) [10]. It is logical that similar protein elements on the outer nuclear membrane could be just as mechanically rich. In fact, magnetic bead microrheology on lamin A-deficient fibroblasts allowed for greater bead displacement coupled with higher reported forces compared to wild type fibroblasts, thus further suggesting that subtle changes in nuclear envelope proteins can yield cellular phenotype changes [11]. However, the microrheology experiment stopped short of single-molecule interrogations of the nuclear envelope.

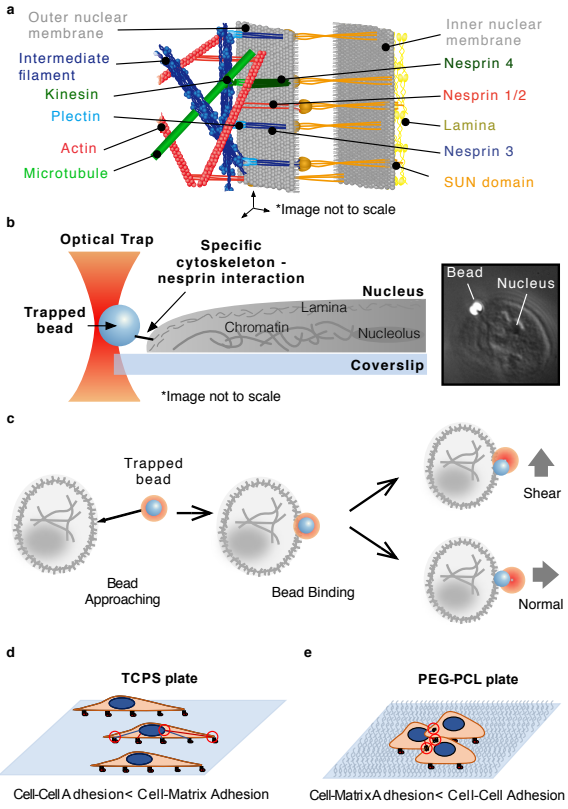

Figure 5.1: **The nuclear membrane and experimental strategy with** (a) depicting the complexity of the environment near the nuclear membrane, including the interactions of cytoskeletal elements with nesprins which are associated with the SUN protein in the periplasm. (b) A general representation of the optical tweezer based assay design for characterization of specific cytoskeleton-nesprin interactions. (c) Binding was achieved by bringing the bead close to the nucleus and waiting for binding, after which force was applied by moving the sample stage to apply either a shear or normal force. Cells were grown on either TCPS (d) or PEG-PCL (e) plates leading towards cell-matrix or cell-cell adhesion biases, respectively.

The principle nuclear envelope proteins engaging the cytoskeleton are known as nesprins, of which there are many isoforms and splice variants, which are key components of the LINC complex (linker of nucleus to cytoskeleton). The cytoskeleton is principally composed of three major protein filaments: actin, intermediate filaments, and microtubules (plus their associated molecules). Nesprins 1 and 2 primarily bind actin, nesprin 3 binds intermediate filaments via the actin-binding domain (ABD) of plectin, and nesprin 4 binds microtubules through kinesin intermediates [12, 13, 14, 15, 16], as seen in Fig. 5.1a. Dis-

ruption or inhibition of these proteins results in decreased cell stiffness and nucleus deformation [17].

Methods to probe nesprin biology have been limited to basic *in vitro* and *in vivo* studies that manipulate gene expression or truncated forms of the nesprin protein itself [18, 19]. A direct connection to gene expression was recently seen in genetically engineered bacteria with fluorescent chromatin-binding proteins subjected to bacterial surface magnetic twisting cytometry. The study demonstrated that increasing force in specified loading directions allowed for greater chromatin unfolding and promoted transcription of sterically repressed genes [20]. Despite this data, little is known about the physical dynamics of the interaction of nesprins with their cytoskeletal partners that ultimately leads to potential changes in gene expression. Thus, there remains an unmet need for new assays that investigate the effects of force on LINC complex proteins, conformational changes and protein-protein/protein-chromatin interactions that can lead to changes in cell phenotype or response.

Optical tweezer based single-molecule assays provide pick-and-place force application with high spatial (nm), temporal (ms), and force (pN) resolution, allowing for the elucidation of molecular mechanisms previously out of reach [8]. We isolated single nuclei and developed a single-molecule on single nuclei assay to probe how force inputs may influence nuclear programming. Here, individual cytoskeletal elements (actin or plectin-ABD) were bound to beads and actively coupled with their respective binding partner (nesprin 1/2 or nesprin 3, respectively) on the nucleus surface (Fig. 5.1b).

5.3 Results

We focused on the effects of three factors on the mechanotransduction of signals from the cytoskeleton to the nucleus: the specific interaction at the nuclear membrane (actin-nesprin 1/2 vs plectin ABD-nesprin 3), the direction of force application (normal vs shear) (Fig. 5.1c), and cell culture history biases as dictated by pre-measurement growth conditions (tissue culture polystyrene (TCPS) versus polyethylene glycol (PEG)-poly(ε-caprolactone)

(PCL) block copolymer). TCPS permits uninhibited cell binding to the entire culture surface. PEG-PCL is a softer culture substrate than TCPS, and inclusion of PEG reduces binding to the substrate. Hence PEG incorporation forces increased cell-cell interactions to avoid anoikis (Fig. 5.1d-e). The morphological changes that result from these growth conditions at the cellular level are mirrored in the nucleus and conserved throughout the 4 hour maximum experimental window in which isolated nuclei were used. Human mesenchymal stem cells (hMSCs) were chosen due to their large nuclei and their known altered phenotype when cultured as single cells on TCPS versus as aggregates on PEG-PCL [21].

Single molecule interactions were achieved through serial dilution of the cytoskeletal component during bead functionalization such that fewer than 50% of beads yielded productive binding. Controls with non-functionalized streptavidin beads showed minimal or no binding to the nuclear membrane (0-2 of 20 beads). Binding was achieved by holding a bead fixed in a trap on the nucleus surface. Force was then applied by moving the sample stage at 20 nm s^{-1}, resulting in a loading rate of 1.8 ± 1.2 (s.d.) pN s^{-1}, which varied with changes in trap stiffness and cell compliance.

Abrupt changes in bead position (Fig. 5.2a), referred to as transitions, were observed for all conditions. A range of transition sizes were present and larger transitions ($>$23 nm) were more prevalent in the actin data. Some transitions were clustered through quick succession of multiple smaller events. These transitions can be described as in a stair steps in which multiple transitions separated by short pauses occurred with the pauses being shorter than the time necessary for reloading of force. A cartoon representative of this behavior is shown in Fig. 5.3. In these cases, a transition was defined at the change in position between two subsequent pauses. Thus, each ”step” in the stair case was analyzed as a separate transition. Full ruptures, indicating the complete disruption of the nesprin/cytoskeleton interaction, were also observed, but were rarer under PEG-PCL conditions (2.5% compared to 9.8% for TCPS nuclei) (Table 5.1).

Top-down plots of these transitions were critical in distinguishing between on- and off-

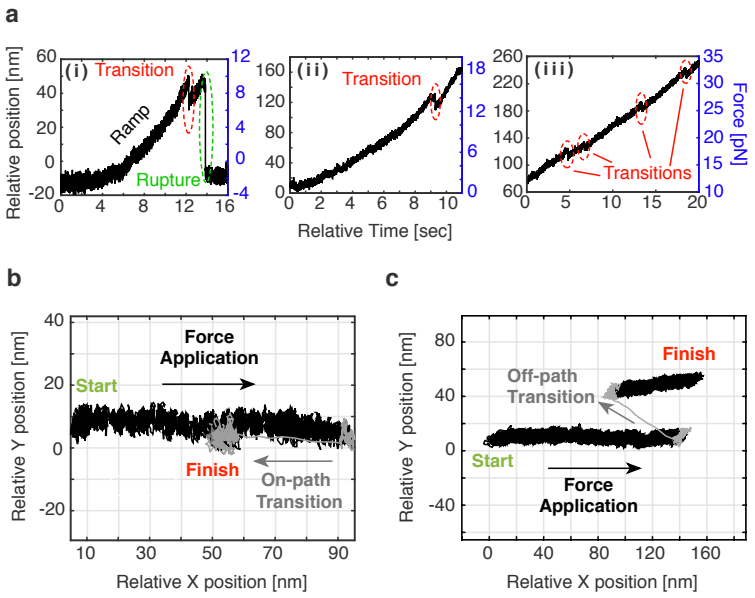

Figure 5.2: **Representative traces** with (a) depicting transitions during force application. Full rupture (i) and small transitions (i-iii) are observed. In some cases, multiple transitions are present in the same trace. (b) A representative top-down plot depicting an on-path transition in which the transition follows the same path back to the origin as during force application. (c) A representative top-down plot depicting an off-path transition in which the transition does not result in a position along the path of force application.

path transitions. On-path transitions were defined as transitions that followed the path of force application back towards the origin (Fig. 5.2b), while off-path transitions indicated a displacement that shifts to a point creating a new vector with respect to the direction of force application (Fig. 5.2c). Off-path transitions were twice as common in actin data (13.5%) as they were in plectin-ABD data (7.8%). Further transition analysis was only completed for on-path transitions. As nesprins 1/2 contain actin-binding domains, more than one nesprin may bind along an actin filament simultaneously. In fact, a nesprin-associated protein, FHOD1, which binds nesprin 2 (at spectrin repeats 11-13), also contains 2 actin-interaction sites [22].

A closer look at the transitions reveals shifts in transition forces given changes in experimental conditions, particularly with respect to force application direction and cell culture conditions. For actin we see a shift to a higher transition force for TCPS nuclei, 22.8 $\pm$ 1.5

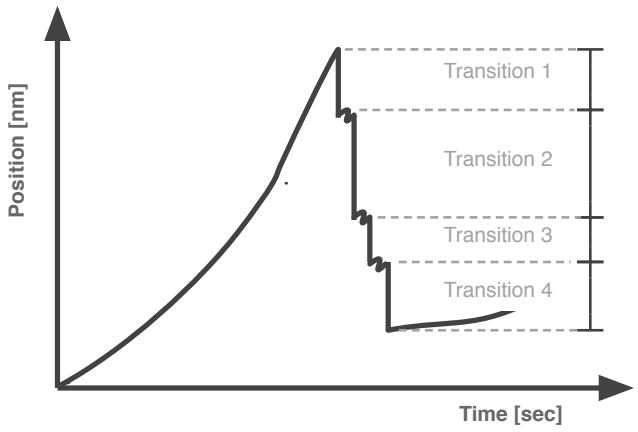

Figure 5.3: **Multistep trace.** A cartoon representative of multi-step or stair step-like transitions seen in some traces. As shown, each step or segment is analyzed as a separate transition.

(s.e.m.) pN, versus PEG-PCL nuclei, 17.6 $\pm$ 0.9 (s.e.m.) pN, when force is applied normal to the nuclei (Fig. 5.4a). This trend is reversed with a shear force, resulting in transition forces of 15.2 $\pm$ 1.6 (s.e.m.) pN for TCPS nuclei and 23.1 $\pm$ 1.7 (s.e.m.) pN for PEG-PCL nuclei (Fig. 5.4b). Additionally, the trends seen in plectin-ABD are consistent with those observed in actin. Again, we see a shift to higher transition forces for TCPS nuclei, 20.5 $\pm$ 1.3 (s.e.m.) pN, versus PEG-PCL nuclei, 13.4 $\pm$ 1.0 (s.e.m.) pN, when force is applied normal to the nuclei (Fig. 5.4a). The trend is reversed with a shear force, resulting in transition forces of 18.6 $\pm$ 2.1 (s.e.m.) pN for TCPS nuclei and 22.6 $\pm$ 1.1 (s.e.m.) pN for PEG-PCL nuclei to (Fig. 5.4b). Collectively, the above transition force results indicate that normal forces stabilize nuclear interactions for TCPS nuclei while shear forces stabilize interactions for PEG-PCL nuclei.

Small transitions were conserved across all experimental conditions, yielding a consistent median transition size (Table 5.1). A closer look at transition sizes revealed a base transition size of 5-6 nm across all conditions (Fig. 5.5), with larger transition populations up to approximately 23 nm. A distribution of transition sizes pooled from all conditions (N=276) exhibits structure fitting well to a multiple Gaussian (Fig. 5.6) with a strong peak

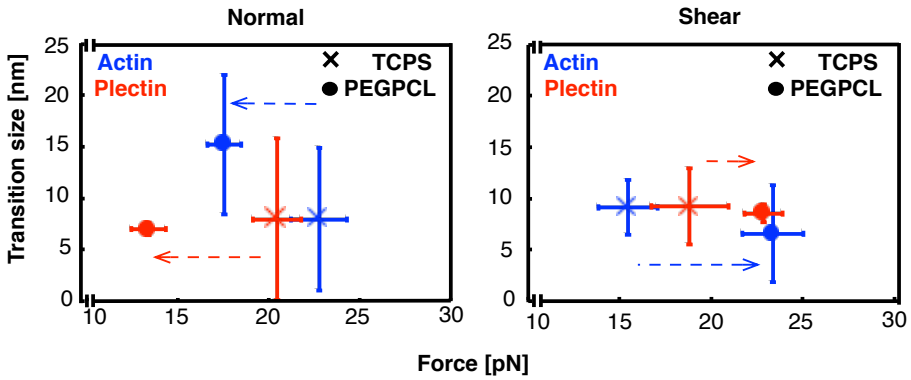

Figure 5.4: **Comparing transition force and size.** A comparison of median transition sizes and mean transition forces for actin and plectin-ABD interactions on nuclei from cells grown on both TCPS and PEG-PCL when force is applied (a) normal and (b) shear to the nuclei. The data indicates that the interactions of PEG-PCL nuclei are stronger when subjected to shear forces while TCPS nuclei are stronger when subjected to normal forces. All error bars are standard error on the mean (s.e.m.). N incorporated into each point in the normal direction are as follows: Actin/TCPS = 42, Actin/PEG-PCL = 40, Plectin-ABD/TCPS = 59, Plectin-ABD/PEG-PCL = 48. N incorporated into each point in the shear direction are as follows: Actin/TCPS = 49, Actin/PEG-PCL = 54, Plectin-ABD/TCPS = 40, Plectin-ABD/PEG-PCL = 44.

representing the base transition size at 5.6 nm, a shoulder at 10.1 nm, and a weak tail centered near 19.2 nm. Transitions larger than approximately 23 nm were less abundant and no longer followed a specific trend.

In a few cases, we observed reversible transition behavior within the trace. These transitions, occurring in quick succession, are characteristic of a structural change at equilibrium and similar reversible behavior has been reported in other systems [23, 24]. The transitions, as observed in Fig. 5.7a, have a time constant, with respect to transition lifetime, of 0.011 s (Fig. 5.8). Interestingly, reversible transitions were observed over a range of forces including at 1.5-2.5 pN, 20-25 pN, and $\sim$32 pN. Similar to the transition sizes in the non-equilibrium data, multiple transition size peaks emerged (Fig. 5.7b) including a base transition size of 5.1 nm, consistent with the 5-6 nm base transition size seen earlier, two strong peaks at 7.9 and 10.2 nm, and a small additional peak centered near 15.2 nm (N=249).

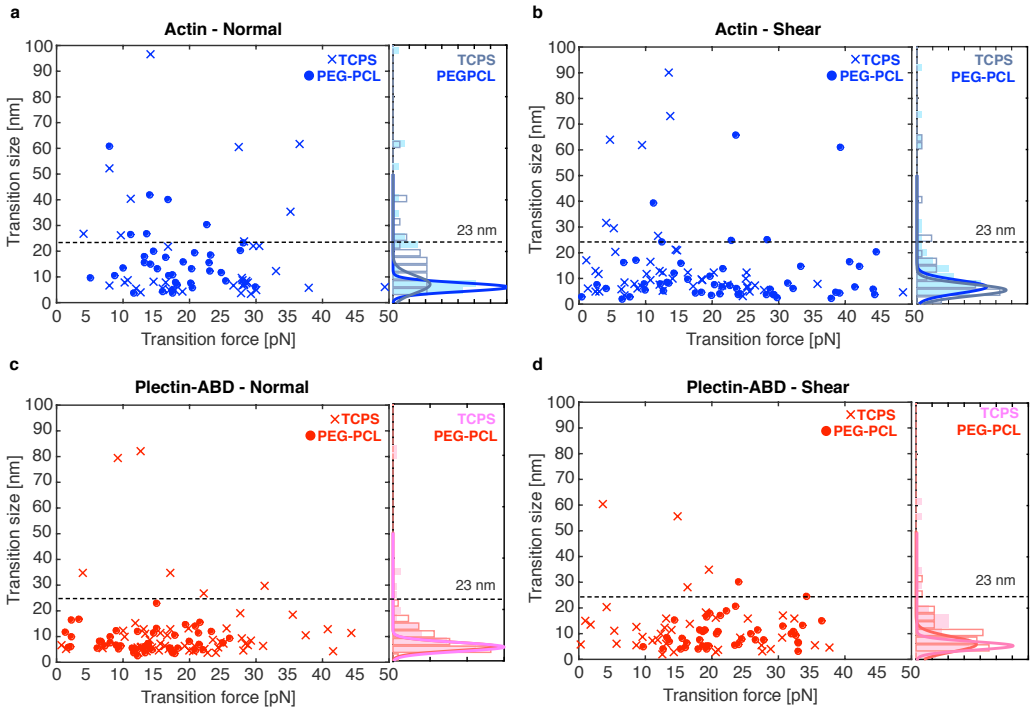

Figure 5.5: **Scatter plots of transition size versus transition force** and a histogram of transition size for (a) actin interactions with normal force, (b) actin interactions with shear force, (c) plectin-ABD interactions with normal force, and (d) plectin-ABD interactions with shear force. The fits overlaying each histogram represent the base transition size of 5-6 nm present in each condition and the dashed line at 23 nm indicates the value at which trends in the transition sizes are no longer observed.

5.4 Discussion

Using optical tweezers to actively present cytoskeletal ligands to nesprin proteins on single isolated nuclei, we observed a mechanically rich system, operating in the force range of 10s of piconewtons. The magnitude of these transition forces is highly dependent on the force application direction (normal or shear) and cell culture history, and define the forces required for cytoskeletal machinery to interact with the nuclei as the cell adapts to external physical cues. The nature of the shift in transition force between cell growth conditions suggests that hMSCs (and perhaps many other cell types) have the ability to alter their force sensing mechanism, allowing for the cells to react to physical stimuli at a nuclear level in a function-specific way. This type of phenomenon has been shown for hMSC differentiation

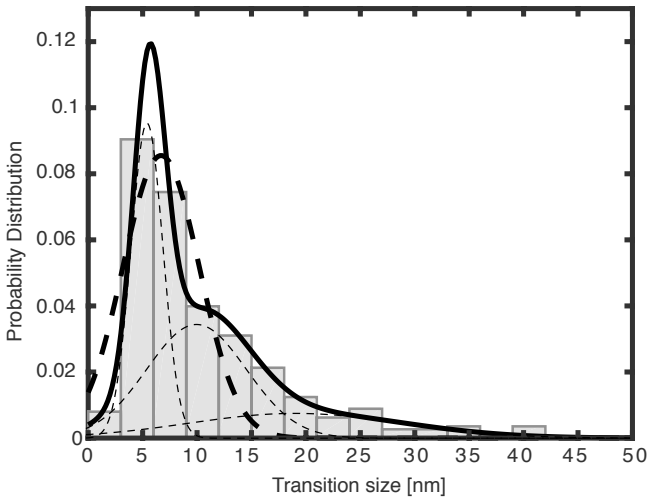

Figure 5.6: **Compiled transition sizes.** A histogram of the compiled data from all conditions (N=376) with a triple Gaussian (solid line) fit and the associated single Gaussian curves (thin dashed line) and a single Gaussian fit (thick dashed line). The triple Gaussian fit yields a base transition size of 5.6 nm with a shoulder at 10.1 and a smaller tail at 19.2 nm. The single Gaussian yields a peak at 6.7 nm.

in tunable hydrogels where the mechanics of the initial gel impart a 'mechanical memory' and influence cell differentiation lineage choice following an *in situ* gel stiffness switch [25].

To start, it is important to consider why the observed transition forces are different between culture substrates. The answer may lie in the morphology of the nuclei that results from their cell culture history. hMSCs on TCPS exhibit a flatter, polarized morphology coupled with a cell-matrix interaction bias (Fig. 5.1d). Isolated TCPS nuclei adopt this morphology with dimensions approximated to be near 15-20 μm x 7-10 μm x 3-5 μm. The PEG-PCL environment yields cells, and nuclei, with a more spherical, morphology and a cell-cell interaction bias (Fig. 5.1e) with a nucleus diameter of $\sim$7-9 μm. While the volumes between these populations of nuclei should be similar, their surface areas are vastly different with TCPS nuclei easily having a surface area 25-30% greater than that of PEG-PCL nuclei. This means that variation in morphology requires differences in the internal architecture (including chromatin-histones and lamin mesh structure) as well as

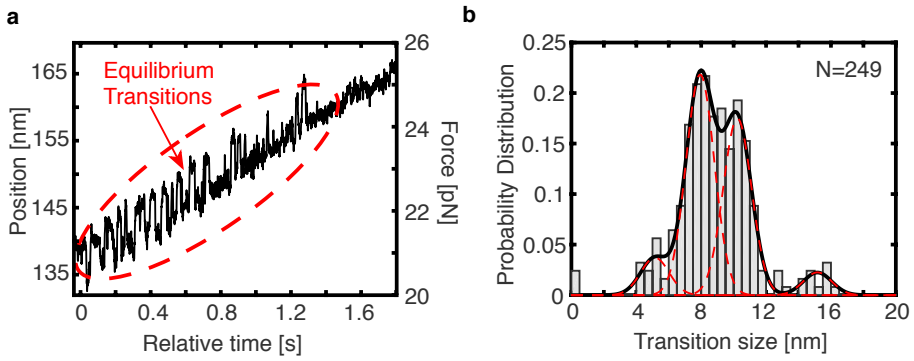

Figure 5.7: **Equilibrium transitions** are present in some traces, usually during the force ramp, as seen in (a) and result in a distribution of transition sizes (b) with Gaussian means at 5.1, 7.9, 10.2, and 15.2 nm. The sum of the Gaussians is shown in black which the single Gaussian distributions are dashed red lines.

the spacing of nesprins on the surface of the nuclei, which could result in minute changes in the presentation of these heteropolymers. These unique geometries could then lead to differences in force requirements [26].

Critical to the function of the LINC complex, the interaction of the SUN protein to the c-terminal region of a nesprin, the KASH domain, is a covalently linked disulfide bond. Previously published research employed dominant negative KASH domains in fibroblasts to demonstrate that the lack of the disulfide bond decouples the physical link between the cytoskeleton to the nucleus [27], and it is unlikely any observed transitions in our data were caused by disruption of the SUN-KASH link. Therefore, transition forces observed in our data likely originate from either within the nucleus (LINC-chromatin interactions) or between the nesprin-cytoskeletal filaments.

Like focal adhesions, LINC complexes can be rather fluid within the nuclear membrane [17], allowing us to speculate that multiple LINC complexes may aggregate and resist higher forces [28, 29]. This focal adhesion-like networking has been found on the nuclear envelope. The transmembrane actin-dependent nuclear (TAN) line phenomena, which are generated by arrays of nesprin 2 and SUN2 proteins, shape the nucleus when cells migrate or reshape to their environment [30]. In such cases the distribution of par-

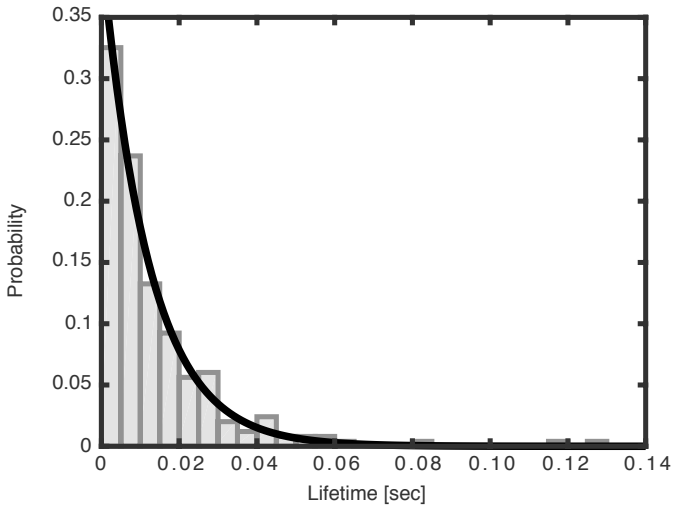

Figure 5.8: **Equilibrium transition lifetime.** A histogram of equilibrium transition lifetimes (N=249) fit with a single exponential characterized by a time constant of 0.0122s with a 95% confidence interval of (0.0114, 0.0131).

allel LINC complexes provide anchor points to sustain higher force loads that manipulate nucleus shape. Networked LINC complexes could potentially subject the nucleus to much higher forces, mirroring focal adhesion networks, transmitting mechanical inputs directly to the nucleus and its contents.

In evaluating on- and off-path transitions, we observe that off-path and larger transitions are more common in actin interactions. The rod like structure of actin permits binding with nesprins at multiple points which can lead to large and/or off-path transitions if one interaction dissociates Fig. 5.9a. Plectin is more accurately modeled as a single point (Fig. 5.9b) and is therefore expected to be on-path. Nesprins can also self-dimerize through interactions between spectrin repeats [31, 32, 33]. Thus, loss of these dimers may also be responsible for off-path transitions.

Small on-path transitions are thought to represent structural unfoldings or conformational changes somewhere along the loading pathway into the nucleus. This is supported by the observed reversible equilibrium behavior described in the results (Fig. 5.7a). While it is impossible to pinpoint the location of structural changes given the complexity of the

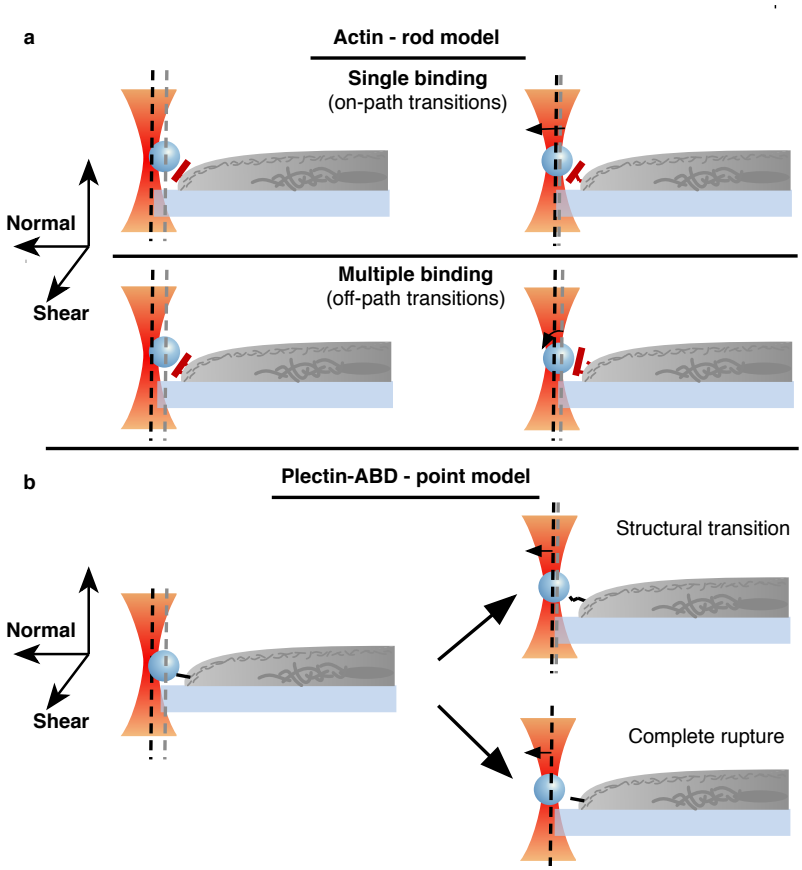

Figure 5.9: **Binding models.** (a) Graphical representations of a rod-like binding model for actin which may include single or multiple nesprin-1/2 interactions with the same actin filament, resulting in on and off-path transitions. (b) Representations of a single point binding model for plectin in which a transition may results in a structural transition or a complete rupture. Similar results may be observed for actin in the case of a single binding event.

load pathway, possibilities include changes within the spectrin repeats of their respective nesprins, linker zones between spectrin repeats, sliding or rearrangement of spectrin repeat helicies, or chromatin rearrangement within the nucleus itself.

The roughly 100-residue long spectrin repeats consist of three helices in anti-parallel arrangement [34, 35]. Unfolding spectrin repeats with an AFM revealed unfolding as an all-or-nothing event between 23 and 42 nm at forces ranging from 25-80 pN [36, 37, 38, 39]. The study by Lenne et al. using a tetramer R16 spectrin repeat, revealed a 15 nm partially unfolded state at forces of 60 pN [39]. Their experiments, while at a much higher loading rate than our own ($\sim$160 pN s^{-1} versus 1.8 $\pm$ 1.2 (s.d.) pN s^{-1}), revealed that a ten-fold decrease in loading rate can result in as much as a 20% decrease in transition force [39]. Based on this observation, the transition forces we observe are consistent. Constant force measurements by Aubin-Tam *et al.* showed in a study utilizing filamin substrate that their $\sim$98 aa extensions corresponded to 14-19 nm at forces of 7-14 pN [40]. Our observed transitions near 15 nm are consistent with full spectrin unfoldings while smaller transitions of 5-10 nm could be attributed to the unfolding of a single helix.

Unlike the short polymers of previous studies [36, 37, 38, 39], the native nesprins here contain high numbers of spectrin repeats with nesprin 1, 2, and 3 containing 74, 56, and 8 repeats, respectively [41, 15]. The greater diversity of spectrin sequence/strength in long spectrin repeats can lead to lower loading rates and partial unfolding states. Our testing conditions approached physiological values as hMSCs can crawl 3 μm hr^{-1} over a stiffness gradient [42].

The unfolding of a single helix within a spectrin repeat may also explain the reversible transitions (hopping) we observed. Grum *et al.* noted that the alpha helices between spectrin repeats can slide and undergo conformational rearrangement that shorten the end-to-end distance of the spectrin repeat and suggested this could be due to bending of the linker regions [43]. Years later, Paramore and Voth found that once a linker region was disrupted, spectrin repeats became less stable, allowing lower forces to further unfold the repeat [44].

Thus, our observed transitions may be the result of linker unfolding.

Another possible source of our transitions is chromatin-histone unbinding and reorganization. In single molecule studies, these have been shown to distort with 5-6 pN and can result in the dissociation of approximately 70 base pairs ($\sim$23 nm) [45, 46]. These forces are within the transition forces we observe and brings to light possibility that gene rearrangement could result solely from mechanical manipulation. While these transitions are larger than what we typically observe here, the histone system is anchored within the nucleus which may reduce the observed transition magnitude.

There are many mechanisms used to transfer signals including diffusion, active transport, and mechanical coupling. As seen here and in previous studies [47, 48], mechanical coupling is crucial to cellular function. The question remains: why has mechanotransduction evolved as a method of signal transfer? Diffusion can be severely limited within the cell due to the crowded intracellular environment [49] and motor-based transport is limited to velocities of approximately 1 μm s^{-1}. However, physical coupling has been reported to allow signal transmission at up to 6 μm s^{-1} [50, 51, 52]. From an energy perspective, mechanical transitions are similar to the chemical energy required for other biological processes. Using an average force of 20 pN and an unfolding distance of 5-23 nm, we estimate an energy requirement per transition per interaction of 24-112 kT at room temperature, which is equal to approximately 1-5 ATP hydrolysis events. Therefore, mechanotransduction allows for signal transduction that is not only fast and stable but also reconfigurable through efficient physical manipulation and structural variation [14, 15, 53].

In conclusion, we have provided new insights into the behavior and response of specific cytoskeletal interactions with the nucleus, including the importance of the cell culture history and the resulting nuclear response to varying force conditions. Prior to the present study, the mechanical response of nuclei had been revealed through AFM and micropipette experiments. We supplement this through direct manipulation of single nuclei at physiologically relevant forces and loading rates. Despite this, there is still much to be learned about

how the nucleus senses, receives, and translates mechanical signals. Further development of this system that includes fluorescence reporting of chromatin opening or rearrangement in real-time could directly connect mechanical input to chromatin alteration and transition states ripe for transcription or repression. Our work on single nuclei and single molecule experiments on nesprin domains and smaller spectrin homopolymers provide a bridge to live cell experiments that probe protein network function. Additionally, future technology that could produce and purify the 750-1000 kDa sized nesprin proteins may help identify specific zones of the protein that are susceptible to unfolding and further characterize the nature of nesprin conformational states. Moreover, CRISPR/Cas9 modulation of nesprin isoform expression can elucidate further mechanical and biochemical roles at the nuclear membrane.

5.5 Materials and Methods

5.5.1 Polymer substrate preparation.

5% PEG (MW = 2000 Da) - 95% PCL (PEG-PCL) was synthesized using methods previously described [54]. Spin-coated polymer films were prepared with a commercial spin-coater (Laurell Technologies, North Wales, PA, USA) on 10 cm Pyrex Petri dishes (Corning Inc., Corning, NY, USA). Specifically, 1% weight/volume (w/v) solution of PEG-PCL in tetrahydrofuran (THF, Sigma Aldrich) was spun for 2 min at 1,500 RPM on Petri dishes (1 ml solution/sample). All samples were then exposed to constant cold-trap vacuum for $\geq$ 30 min to remove excess solvent Dishes were UV sterilized for 60 min before use.

5.5.2 Cell culture.

hMSCs were purchased from Lonza (Walkersville, MD, USA). hMSCs were maintained in complete media (CM) composed of alpha-minimum essential media with nucleosides (αMEM, Life Technologies, Carlsbad, CA, USA) with 16.7% fetal bovine serum

(Life Technologies), 1% penicillin/streptomycin (Life Technologies), and 4 μg mL^{-1} plasmocin (InvivoGen, San Diego, CA, USA). Cells were kept in a humidified incubator at 37 C and 5% CO_2, and media was replaced twice each week. For all experiments, hMSCs (passage 5) were seeded at a density of 10,000 viable cells cm^{-2}, as determined by exclusion of Trypan blue, and cultured for three to four days.

5.5.3 Nucleus enrichment

After being cultured for three to four days, cells were washed with PBS-/-, trypsanized, diluted with culture media and centrifuged for 5 minutes at 400 g. The supernatant was removed and the pellet was resuspended in 15 mL of Buffer A (10 mM HEPES, 1.5 mM $MgCl_2$, 10 mM KCl, 0.5 mM DTT and 0.05% NP-40) with 1% v/v protease inhibitors. The suspension was incubated on ice for 20 minutes in a large dounce homogenizer and subsequently subjected to 15-20 dounce motions with plunger B. The dounced suspension was cold centrifuged (4 °C) for 10 minutes at 218 g. The supernatant was removed and the nucleus pellet was resuspended in 200 μL of nucleus wash buffer (0.2 M sucrose, 10 mM HEPES, and 1 mM $MgCl_2$) with 1% v/v protease inhibitors.

5.5.4 Generation of actin-functionalized beads.

Biotinylated actin was created such that actin and biotinylated actin were present in a 10:1 ratio. First, 5 μL of 10 mg mL^{-1} pure actin (Cytoskeleton-AKL99) in deionized water is mixed with 5 μL of 1 mg mL^{-1} biotinylated actin (Cytoskeleton-AB07). Then 100 μL of General Actin Buffer, GAB, (5 mM Tris-HCl, 0.2 mM $CaCl_2$, 0.5 mM DTT, 0.2 mM ATP) was added and the mixture placed on ice for 1 hour. Actin was then polymerized by adding 11 μL of Actin Polymerization Buffer, APB, (50 mM Tris-HCl, 500 mM KCl, 2 mM $MgCl_2$, 2 mM $CaCl_2$, 2 mM DTT, 5 mM ATP) and incubating on ice for 20 minutes. After polymerization, actin filaments were stabilized by adding 5 μL phalloidin (Life Technologies - A22282) and incubating on ice in the dark for 1 hour. Actin was then diluted

as needed through dilution into a 10:1 GAB/APB buffer mixture. Eight microliters of 1.09 μm streptavidin coated polystyrene beads (Spherotech - SVP-10-5) were mixed with 5 μL biotinylated actin filaments (diluted 10,000 times from stock into 10:1 GAB/APB buffer), 0.6 μL ATP (100 mM), and 45 μL of nucleus wash buffer and allowed to mix on a rotator for 30 minutes at room temperature.

5.5.5 Generation of plectin-ABD-functionalized beads.

Plectin-ABD functionalized beads were created by binding purified plectin-ABD protein to streptavidin beads via a glutathione linker. Biotinylated glutathione was first created by mixing 4 μL of 5 mg mL^{-1} biotinylated maleimide (Sigma - B1267) in DMSO with 50 μL of 10 mg mL^{-1} glutathione (ThermoScientific - 78259) in deionized water and incubating at 4 °C on a rotator overnight to generate biotinylated glutathione. Streptavidin beads were then functionalized with glutathione by mixing 10 μL of 1.09 μm streptavidin beads pre-diluted 20 times in PBS (pH 7.4), 30 μL of the overnight biotinylated glutathione solution, 2 μL of biotinylated bovine serum albumin (b-BSA, 5 mg mL^{-1}), and 58 μL PBS. The solution was then incubated on a rotator at room temperature for 1 hour. Excess and unreacted reagents were removed from the bead solution and the buffer exchanged to nucleus wash buffer by centrifuging the sample two times for 3.5 minutes at 9250 rpm and resuspending the beads in nucleus wash buffer each time. After the second centrifuge step, the beads were resuspended in 200 μL of nucleus wash buffer, 2 times that in the original solution. Upon completion, the resulting bead solution was sonicated using a cup sonicator for 2 minutes at 20%. Plectin-ABD (from Litjens *et al*. [55]) is then added to the bead solution at single molecule concentrations by mixing 50 μL glutathione bead solution, 50 μL plectin-ABD (diluted 1:1 million in nucleus wash buffer, $\sim$5 ng mL^{-1}), and 1 μL ATP (100 mM) and incubating the mixture on a rotator at room temperature for 2 hours.

5.5.6 Slide Preparation

Slides were prepared by creating a 10-15 μL flow cell using potassium hydroxide (KOH) etched coverslips coated in poly-L-lysine, standard microscope slides, and double-sided sticky tape. After etching, the coverslips were coated in poly-L-lysine (Sigma Aldrich - P8920) by applying a layer of 3% poly-L-lysine solution in ethanol to one side of a coverslip ($\sim$200 μL). The coverslip was then placed in the oven at approximately 90 °C until the ethanol was fully evaporated. The flow cell was then created using double-sided tape, ensuring the poly-L-lysine coated side of the coverslip faced the slide. Upon formation of the flow cell, a 20 μL nuclei sample was loaded onto the slide and incubated at room temperature for 30 minutes to allow the nuclei to become immobilized on the surface. Passivation of the surface was achieved by adding 20 μL of a 10 mg mL^{-1} solution of bovine serum albumin (Sigma Aldrich - A7030) in nucleus wash buffer to the flow cell and allowing the slide to incubate at room temperature for 10 minutes. Finally, 20 μL of the appropriate bead solution was added to the flow cell, which was then sealed and the slide placed on the microscope.

5.5.7 Data Acquisition

A slide is loaded onto a custom built inverted microscope with an optical trap and an isolated nucleus is found in the field of view. Then a functionalized bead is located, brought near a side of the nucleus that is oriented along an axis of the sample stage, and focused such that the edge of the nucleus is clear. The bead is calibrated and the stiffness found using the variance. Upon calibration, the bead is carefully brought into contact with the nucleus by manually moving the sample stage. This was repeated 3-4 times in an effort to initiate binding. If binding did not occur, the bead was discarded. If binding occurred, the bead was centered using a custom LabVIEW program and data acquisition initiated. After centering, the sample stage was moved in the desired direction at 20 nm s^{-1}, resulting in a

loading rate of 1.8 $\pm$ 1.2 (s.d.) pN s^{-1}, during which transitions regularly occurred. At the end of a ramp, the sample was stepped back to the center and pulled again. Each bead and each nucleus was only used once, however, it is possible to obtain several transitions from a single bead-nucleus interaction.

5.5.8 Data Analysis

All data analysis was completed using custom Matlab scripts. Data were collected at a 3 kHz sampling frequency with an anti-alias filter at 1.5 kHz and later averaged using an exponentially weighted moving average over a 10 point time period during analysis. The force of each trace is found by removing any baseline in the position and the multiplying the nanometer position measurements by the trap stiffness. Transitions were then determined to be on or off-path using a top-down view of the respective trace (Fig. 5.2). On-path transitions were kept while off-path transitions were discarded and omitted from further analysis. Distributions fit were found using the cftool Matlab tool and constraints were also set such that each Gaussian in a multiple Gaussian fit had equal variances and if more than two peaks were found, each peak was separated by the same distance. In the cases in which equilibrium-like transitions were observed, the transitions were analyzed in the same manner but kept as a separate dataset.

5.6 Acknowledgments

This research work was funded and supported by NSF DMR BMAT under 1506717 and NIH EB under 019509 (D.A.B. and H.J.S.). H.J.S. was also supported by the Faculty Research Assistance Program of Yonsei University College of Medicine for 2000 (6-2016-0031). U.H.K was supported by the National Research Foundation of Korea (NRF) under MEST-2015M3A9B3028216. This work was also supported, in part, by Singapore-MIT Alliance for Research and Technology BioSym, NSF under 1330792, and GAANN under P200A090323 (S.K.B and M.J.L).

Table 5.1: Transition characterization overview

	Normal				Shear			
	Actin TCPS	Actin PEG-PCL	Plecin-ABD TCPS	Plectin-ABD PEG-PCL	Actin TCPS	Actin PEG-PCL	Plecin-ABD TCPS	Plectin-ABD PEG-PCL
N	42	40	59	48	49	54	40	44
Force, mean ± SEM [pN]	22.76 ± 1.54	17.56 ± 0.93	20.45 ± 1.33	13.39 ± 0.96	15.21 ± 1.61	23.11 ± 1.67	18.58 ± 2.12	22.62 ± 1.05
Force, median ± SEMd [pN]	26.99 ± 1.93	17.44 ± 1.17	19.26 ± 1.67	13.63 ± 1.20	12.55 ± 2.02	22.15 ± 2.09	14.53 ± 2.66	20.79 ± 1.32
Transition size, mean ± SEM [nm]	26.63 ± 6.96	29.28 ± 6.81	27.32 ± 7.85	8.36 ± 0.62	16.06 ± 2.65	15.79 ± 4.70	16.35 ± 3.73	10.17 ± 0.88
Transition size, median ± SEMd [nm]	7.97 ± 8.72	15.22 ± 8.53	7.95 ± 9.84	7.04 ± 0.78	9.57 ± 3.32	7.03 ± 5.89	9.67 ± 4.67	8.98 ± 1.10
# full rupture	4 (9.5%)	4 (10%)	7 (12%)	0 (0%)	5 (10.2%)	1 (1.8%)	2 (5%)	0 (0%)

5.7 Bibliography

[1] J. J. Chiu and S. Chien. Effects of disturbed flow on vascular endothelium: pathophysiological basis and clinical perspectives. *Physiol Rev*, 91(1):327–87, 2011.

[2] P. F. Davies, A. Remuzzi, E. J. Gordon, Jr. Dewey, C. F., and Jr. Gimbrone, M. A. Turbulent fluid shear stress induces vascular endothelial cell turnover *in vitro*. *Proc Natl Acad Sci U S A*, 83(7):2114–7, 1986.

[3] S Q Liu, M Yen, and Y C Fung. On measuring the third dimension of cultured endothelial cells in shear flow. *Proc Natl Acad Sci U S A*, 91(19):8782–8786, Sep 1994.

[4] S Chien, S Li, and Y J Shyy. Effects of mechanical forces on signal transduction and gene expression in endothelial cells. *Hypertension*, 31(1 Pt 2):162–169, Jan 1998.

[5] P. R. Girard and R. M. Nerem. Endothelial cell signaling and cytoskeletal changes in response to shear stress. *Front Med Biol Eng*, 5(1):31–6, 1993.

[6] E. Tzima. Role of small GTPases in endothelial cytoskeletal dynamics and the shear stress response. *Circ Res*, 98(2):176–85, 2006.

[7] B. D. Hoffman, C. Grashoff, and M. A. Schwartz. Dynamic molecular processes mediate cellular mechanotransduction. *Nature*, 475(7356):316–23, 2011.

[8] G. R. Fedorchak, A. Kaminski, and J. Lammerding. Cellular mechanosensing: getting to the nucleus of it all. *Prog Biophys Mol Biol*, 115(2-3):76–92, 2014.

[9] A. J. Maniotis, C. S. Chen, and D. E. Ingber. Demonstration of mechanical connections between integrins, cytoskeletal filaments, and nucleoplasm that stabilize nuclear structure. *Proc Natl Acad Sci U S A*, 94(3):849–54, 1997.

[10] B. P. Helmke, A. B. Rosen, and P. F. Davies. Mapping mechanical strain of an endogenous cytoskeletal network in living endothelial cells. *Biophys J*, 84(4):2691–9, 2003.

[11] J. Lammerding, P. C. Schulze, T. Takahashi, S. Kozlov, T. Sullivan, R. D. Kamm, C. L. Stewart, and R. T. Lee. Lamin A/C deficiency causes defective nuclear mechanics and mechanotransduction. *J Clin Invest*, 113(3):370–8, 2004.

[12] V. C. Padmakumar, S. Abraham, S. Braune, A. A. Noegel, B. Tunggal, I. Karakesisoglou, and E. Korenbaum. Enaptin, a giant actin-binding protein, is an element of the nuclear membrane and the actin cytoskeleton. *Exp Cell Res*, 295(2):330–9, 2004.

[13] D. Rajgor and C. M. Shanahan. Nesprins: from the nuclear envelope and beyond. *Expert Rev Mol Med*, 15:e5, 2013.

[14] K. J. Roux, M. L. Crisp, Q. Liu, D. Kim, S. Kozlov, C. L. Stewart, and B. Burke. Nesprin 4 is an outer nuclear membrane protein that can induce kinesin-mediated cell polarization. *Proc Natl Acad Sci U S A*, 106(7):2194–9, 2009.

[15] K. Wilhelmsen, S. H. Litjens, I. Kuikman, N. Tshimbalanga, H. Janssen, I. van den Bout, K. Raymond, and A. Sonnenberg. Nesprin-3, a novel outer nuclear membrane protein, associates with the cytoskeletal linker protein plectin. *J Cell Biol*, 171(5):799–810, 2005.

[16] Y. Y. Zhen, T. Libotte, M. Munck, A. A. Noegel, and E. Korenbaum. NUANCE, a giant protein connecting the nucleus and actin cytoskeleton. *J Cell Sci*, 115(Pt 15):3207–22, 2002.

[17] P. J. Stewart-Hutchinson, C. M. Hale, D. Wirtz, and D. Hodzic. Structural requirements for the assembly of LINC complexes and their function in cellular mechanical stiffness. *Exp Cell Res*, 314(8):1892–905, 2008.

[18] J. Wu, I. A. Kent, N. Shekhar, T. J. Chancellor, A. Mendonca, R. B. Dickinson, and T. P. Lele. Actomyosin pulls to advance the nucleus in a migrating tissue cell. *Biophys J*, 106(1):7–15, 2014.

[19] X. Zhang, K. Lei, X. Yuan, X. Wu, Y. Zhuang, T. Xu, R. Xu, and M. Han. SUN1/2 and syne/nesprin-1/2 complexes connect centrosome to the nucleus during neurogenesis and neuronal migration in mice. *Neuron*, 64(2):173–87, 2009.

[20] A. Tajik, Y. Zhang, F. Wei, J. Sun, Q. Jia, W. Zhou, R. Singh, N. Khanna, A. S. Belmont, and N. Wang. Transcription upregulation via force-induced direct stretching of chromatin. *Nat Mater*, 2016.

[21] Spencer W. Crowder, Daniel A. Balikov, Timothy C. Boire, Devin McCormack, Jung Bok Lee, Mukesh K. Gupta, Melissa C. Skala, and Hak-Joon Sung. Copolymer-mediated cell aggregation promotes a proangiogenic stem cell phenotype in vitro and in vivo. *Advanced Healthcare Materials*, 5(22):2866–2871, 2016.

[22] S. Kutscheidt, R. Zhu, S. Antoku, G. W. Luxton, I. Stagljar, O. T. Fackler, and G. G. Gundersen. FHOD1 interaction with nesprin-2G mediates TAN line formation and nuclear movement. *Nat Cell Biol*, 16(7):708–15, 2014.

[23] F. M. Fazal and S. M. Block. Optical tweezers study life under tension. *Nat Photonics*, 5:318–321, 2011.

[24] J. Liphardt, B. Onoa, S. B. Smith, Jr. Tinoco, I., and C. Bustamante. Reversible unfolding of single RNA molecules by mechanical force. *Science*, 292(5517):733–7, 2001.

[25] C. Yang, M. W. Tibbitt, L. Basta, and K. S. Anseth. Mechanical memory and dosing influence stem cell fate. *Nat Mater*, 13(6):645–52, 2014.

[26] Ekta Makhija, D. S. Jokhun, and G. V. Shivashankar. Nuclear deformability and telomere dynamics are regulated by cell geometric constraints. *Proceedings of the National Academy of Sciences*, 113(1):E32–E40, 2016.

[27] Maria L Lombardi, Diana E Jaalouk, Catherine M Shanahan, Brian Burke, Kyle J Roux, and Jan Lammerding. The interaction between nesprins and SUN proteins at the nuclear envelope is critical for force transmission between the nucleus and cytoskeleton. *The Journal of Biological Chemistry*, 286(30):26743–26753, 07 2011.

[28] U. S. Schwarz, N. Q. Balaban, D. Riveline, A. Bershadsky, B. Geiger, and S. A. Safran. Calculation of forces at focal adhesions from elastic substrate data: the effect of localized force and the need for regularization. *Biophys J*, 83(3):1380–94, 2002.

[29] N. Q. Balaban, U. S. Schwarz, D. Riveline, P. Goichberg, G. Tzur, I. Sabanay, D. Mahalu, S. Safran, A. Bershadsky, L. Addadi, and B. Geiger. Force and focal adhesion assembly: a close relationship studied using elastic micropatterned substrates. *Nat Cell Biol*, 3(5):466–72, 2001.

[30] G. W. Luxton, E. R. Gomes, E. S. Folker, E. Vintinner, and G. G. Gundersen. Linear arrays of nuclear envelope proteins harness retrograde actin flow for nuclear movement. *Science*, 329(5994):956–9, 2010.

[31] Z. Zhong, S. A. Chang, A. Kalinowski, K. L. Wilson, and K. N. Dahl. Stabilization of the spectrin-like domains of nesprin-1α by the evolutionarily conserved "adaptive" domain. *Cell Mol Bioeng*, 3(2):139–150, 2010.

[32] J. M. Mislow, J. M. Holaska, M. S. Kim, K. K. Lee, M. Segura-Totten, K. L. Wilson, and E. M. McNally. Nesprin-1α self-associates and binds directly to emerin and lamin A *in vitro*. *FEBS Lett*, 525(1-3):135–40, 2002.

[33] M. Ketema, K. Wilhelmsen, I. Kuikman, H. Janssen, D. Hodzic, and A. Sonnenberg.

Requirements for the localization of nesprin-3 at the nuclear envelope and its interaction with plectin. *J Cell Sci*, 120(Pt 19):3384–94, 2007.

[34] D. A. Parry, T. W. Dixon, and C. Cohen. Analysis of the three-alpha-helix motif in the spectrin superfamily of proteins. *Biophys J*, 61(4):858–67, 1992.

[35] D. W. Speicher and V. T. Marchesi. Erythrocyte spectrin is comprised of many homologous triple helical segments. *Nature*, 311(5982):177–80, 1984.

[36] R. Law, P. Carl, S. Harper, P. Dalhaimer, D. W. Speicher, and D. E. Discher. Cooperativity in forced unfolding of tandem spectrin repeats. *Biophys J*, 84(1):533–44, 2003.

[37] L. G. Randles, R. W. Rounsevell, and J. Clarke. Spectrin domains lose cooperativity in forced unfolding. *Biophys J*, 92(2):571–7, 2007.

[38] M. Rief, J. Pascual, M. Saraste, and H. E. Gaub. Single molecule force spectroscopy of spectrin repeats: low unfolding forces in helix bundles. *J Mol Biol*, 286(2):553–61, 1999.

[39] P. F. Lenne, A. J. Raae, S. M. Altmann, M. Saraste, and J. K. H. Hörber. States and transitions during forced unfolding of a single spectrin repeat. *FEBS Letters*, 476(3):124–128, 2000.

[40] Marie-Eve Aubin-Tam, Adrian O Olivares, Robert T Sauer, Tania A Baker, and Matthew J Lang. Single-molecule protein unfolding and translocation by an ATP-fueled proteolytic machine. *Cell*, 145(2):257–267, 2011.

[41] F. Autore, M. Pfuhl, X. Quan, A. Williams, R. G. Roberts, C. M. Shanahan, and F. Fraternali. Large-scale modelling of the divergent spectrin repeats in nesprins: giant modular proteins. *PLoS One*, 8(5):e63633, 2013.

[42] L. G. Vincent, Y. S. Choi, B. Alonso-Latorre, J. C. del Alamo, and A. J. Engler. Mesenchymal stem cell durotaxis depends on substrate stiffness gradient strength. *Biotechnol J*, 8(4):472–84, 2013.

[43] V. L. Grum, D. Li, R. I. MacDonald, and A. Mondragon. Structures of two repeats of spectrin suggest models of flexibility. *Cell*, 98(4):523–35, 1999.

[44] S. Paramore and G. A. Voth. Examining the influence of linkers and tertiary structure in the forced unfolding of multiple-repeat spectrin molecules. *Biophys J*, 91(9):3436–45, 2006.

[45] Y. Cui and C. Bustamante. Pulling a single chromatin fiber reveals the forces that maintain its higher-order structure. *Proc Natl Acad Sci U S A*, 97(1):127–32, 2000.

[46] B. Xiao, B. S. Freedman, K. E. Miller, R. Heald, and J. F. Marko. Histone H1 compacts DNA under force and during chromatin assembly. *Mol Biol Cell*, 23(24):4864–71, 2012.

[47] S. B. Khatau, R. J. Bloom, S. Bajpai, D. Razafsky, S. Zang, A. Giri, P. H. Wu, J. Marchand, A. Celedon, C. M. Hale, S. X. Sun, D. Hodzic, and D. Wirtz. The distinct roles of the nucleus and nucleus-cytoskeleton connections in three-dimensional cell migration. *Sci Rep*, 2:488, 2012.

[48] R. J. Petrie, H. Koo, and K. M. Yamada. Generation of compartmentalized pressure by a nuclear piston governs cell motility in a 3D matrix. *Science*, 345(6200):1062–5, 2014.

[49] J. S. Wiegert, C. P. Bengtson, and H. Bading. Diffusion and not active transport underlies and limits ERK1/2 synapse-to-nucleus signaling in hippocampal neurons. *J Biol Chem*, 282(40):29621–33, 2007.

[50] N. Wang, J. D. Tytell, and D. E. Ingber. Mechanotransduction at a distance: mechanically coupling the extracellular matrix with the nucleus. *Nat Rev Mol Cell Biol*, 10(1):75–82, 2009.

[51] S. Na, O. Collin, F. Chowdhury, B. Tay, M. Ouyang, Y. Wang, and N. Wang. Rapid signal transduction in living cells is a unique feature of mechanotransduction. *Proc Natl Acad Sci U S A*, 105(18):6626–31, 2008.

[52] S. Hu and N. Wang. Control of stress propagation in the cytoplasm by prestress and loading frequency. *Mol Cell Biomech*, 3(2):49–60, 2006.

[53] P. Isermann and J. Lammerding. Nuclear mechanics and mechanotransduction in health and disease. *Curr Biol*, 23(24):R1113–21, 2013.

[54] S. W. Crowder, M. K. Gupta, L. H. Hofmeister, A. L. Zachman, and H. J. Sung. Modular polymer design to regulate phenotype and oxidative response of human coronary artery cells for potential stent coating applications. *Acta Biomaterialia*, 8(2):559–569, 2012.

[55] S. H. Litjens, J. Koster, I. Kuikman, S. van Wilpe, J. M. de Pereda, and A. Sonnenberg. Specificity of binding of the plectin actin-binding domain to $\beta 4$ integrin. *Mol Biol Cell*, 14(10):4039–50, 2003.

Chapter 6

CONCLUSIONS AND FUTURE WORK

The continuation and advancement of single molecule experiments is critical in gaining a better understanding of biological systems on a molecular scale. The impact of such studies spans a wide range of industries including alternative energy and medicine and could have an impact on any number of others. This thesis uses single molecule techniques, namely optical trapping, to explore the mechanics of three systems: cellulose degradation, cellulose synthesis, and mechanotransduction at the nuclear membrane. While we have contributed to the understanding of all these systems, there is still much to be done.

Our investigation of cellulose degradation specifically explored the behavior of cellobiohydrolase I from *Trichoderma reesei*, known as *Tr*Cel7A, and its isolated domains. We found that this enzyme degrades cellulose in single cellobiose steps, with a fundamental step size of 1.3 nm and a velocity of 0.25 nm s^{-1}. Backwards steps and double steps are also present. We also discovered that despite bulk experiments and our own DNS activity and mass spectrometry data, the catalytic domain is active and independently capable of translocation closely mimicking that of wt*Tr*Cel7A. However, commitment to productive binding and motility is greatly reduced (50-60x) in the absence of the CBM, resulting in a low apparent bulk activity. The presence of the CBM may slightly inhibit motility in wt*Tr*Cel7A, but this is a small price to pay for productive binding.

Additionally, we investigated the effect of cellulose crystal structure on *Tr*Ce7A and isolated CBM behavior. Our studies confirm that cellulose hydrolysis is slower on cellulose III than cellulose I by *Tr*Cel7A alone. This observation is a result of longer dwell times and smaller steps (possibly due to the difference in surface geometry). *Tr*Cel7A also has a lower affinity for cellulose III. This does not explain the increased hydrolysis observed in bulk when cellulase mixtures are used, but we can speculate that perhaps the lower affinity

allows non-productively bound enzymes to be more readily released from cellulose III. The more disordered surface may also allow for increased activity of other cellulases, creating more binding sites for cellobiohydrolases and helping to increase the bulk hydrolysis rate of mixtures.

Given our results, challenges in developing the next generation of cellulose degrading enzymes will include the development of constructs that improve recovery while also improving hydrolysis rates and increasing our understanding of the enzymatic interactions within cellulase systems. Future work in cellulase systems should focus on functional mutations of *Tr*Cel7A, the development of new constructs that perhaps include multiple heads or a cleavable linker allowing for easy recovery of the CD, and studies focusing on the interaction between multiple enzyme species on various forms of cellulose substrate. Functional mutations will allow for a deeper understanding of *Tr*Cel7A behavior with the potential for such studies to lead to the development of more economical enzyme constructs for use on an industrial scale. Additionally, a better understanding of cellulase relationships and their synergy on varying substrates would allow for the opportunity to develop cellulose processing procedures that can capitalize on these relationships, particularly if using in conjunction with functional mutations and substrate pretreatments.

While cellulase systems have long been of interest, a focused effort to understand cellulose synthesis has only developed recently. The interest extends to understanding cellulose synthesis in general, however the synthesis systems of bacteria are more simple and the role of bacterial cellulose in biofilms makes understanding bacterial synthesis systems a high priority. The biochemistry of cellulose synthesis by bacterial cellulose synthase (Bcs), specifically the catalytically active BcsAB complex, has been studied in detail by the Zimmer lab at the University of Virginia. Their work has revealed that synthesis occurs one glucose unit at a time, releasing a UDP molecule with each glucose addition. Further, c-di-GMP is necessary for synthesis as its binding to BcsA allows for the opening of the gating loop which allows for access to the active site. Additionally, they discov-

ered that while BcsB is necessary for catalytic activity, only the transmembrane anchor of BcsB is necessary for activity. Our work expands on this knowledge to reveal a cellulose elongation velocity of 0.32 nm s^{-1}. Elongation traces suggest structure embedded in the synthesis process on the order of 11 nm, however, the origin of these structures is still unknown. Most interestingly, we discover a highly biochemically limited system with an assisting stall force of approximately 6.3 pN. It is reasonable to project that this stall force could play an important role in the regulation of cellulose transport across the periplasm to BcsC at the outer membrane. We also presented preliminary results using a truncated S678 construct which only includes BcsA and the transmembrane anchor of BcsB.

After completion of S678 as well as UDP-glucose and c-di-GMP limited studies, the next step in understanding the Bcs system is to investigate BcsC and cellulose transport across the periplasm and outer membrane. This provides additional challenges as a functional assay requires a full membrane environment. However, development of single molecule BcsC assays could then lead to a full BcsABC assay which would inform the Bcs mechanism all the way from synthesis at the inner membrane to cellulose deposit outside the cell using a minimal model system. Ultimately this would provide insight into biofilm formation that could save millions of dollars in healthcare related costs in biofilm prevention and treatment of biofilm derived infections, and savings in maintenance and cleaning costs of production processes across an array of industries.

Finally, understanding signaling pathways in the cell is vitally important for medical advancement, stem cell research, individualized medicine, tissue repair and growth, etc. As we continue to learn more, the role of mechanotransduction in biological processes and development continues to become more apparent. A lot of work has been done with a focus on the effect of forces at the cell membrane but there is much to be learned about how those forces lead to changes in gene expression. Here, we get one step closer to understanding this mechanotransduction process by focusing on the effect of forces in a *semi situ* environment at the nuclear membrane, opening the door for more single molecule studies. We

find that nuclei have memory regarding their grown history and that this history affects the force magnitude and direction to which the nuclei are more/less sensitive. The application of force to the nuclei results in structural changes within the interaction with a base structure size of 5-6 nm. Interestingly, the specific cytoskeletal-nucleus interaction that was targeted (actin to nesprin 1/2 or plectin-ABD to nesprin 3) does not seem to have an effect on any observed trends in force beyond some slight differences in force magnitude. The source of observed structural changes is unknown but could involve unfolding behavior in spectrin repeats of nesprins or perhaps structural changes in chromatin within the nucleus, or both.

We present a picture of a mechanically rich system at the nuclear membrane, but further work it required to understand the source of observed structural transitions, how those structural changes are translated into changes in gene expression, the magnitude of the mechanical assault and number of interactions necessary to alter gene expression, and more. In addition, single molecule experiments on smaller spectrin polymers at physiologically relevant loading rates, and on isolated nesprins and functional mutations (with the development of techniques allowing for expression of MDa proteins), could be used to further characterize structural transitions and conformational states.

Appendix A

PROTOCOLS

A.1 **Buffer Recipes**

1. 10 mM TEA-HCl, pH 7.6
   To be used in *Tr*Cel7A purification (Chapter 2)

   Materials:
   TEA-HCl
   Deionized water

   (a) Prepare 50 mL of 10 mM TEA-HCl by mixing:
   92.7 mg TEA-HCl
   40 mL deionized water

   (b) Add small volumes of concentrated KOH solution to adjust the pH to 7.6.

   (c) Add deionized water to a final volume of 50 mL.

2. 20 mM TEA-HCl, pH 7.0
   To be used in *Tr*Cel7A purification (Chapter 2)

   Materials:
   TEA-HCl
   Deionized water

   (a) Prepare 80 mL of 20 mM TEA-HCl by mixing:
   297.3 mg TEA-HCl
   70 mL deionized water

   (b) Add small volumes of concentrated KOH solution to adjust the pH to 7.0.

   (c) Add deionized water to a final volume of 80 mL.

3. 0.1 M NaCl in 20 mM TEA-HCl, pH 7.0
   To be used in *Tr*Cel7A purification (Chapter 2)

   Materials:
   20 mM TEA-HCl

NaCl

(a) Prepare 15 mL by adding 87.7 mg NaCl to a total volume of 15 mL of 20 mM TEA-HCl in a 15 mL Falcon tube as prepared above.

4. 0.33 M NaCl in 20 mM TEA-HCl, pH 7.0
To be used in *Tr*Cel7A purification (Chapter 2)

Materials:
20 mM TEA-HCl
NaCl

(a) Prepare 15 mL by adding 289.1 mg NaCl to a total volume of 15 mL of 20 mM TEA-HCl in a 15 mL Falcon tube as prepared above.

5. 0.1 M MES buffer with 0.01% tween-20, pH 4.5
To be used in the preparation of anti-DIG beads using EDC chemistry.

Materials:
MES
Tween-20

(a) Prepare 100 mL of buffer by mixing the following:
1.95 mg MES
10 μL Tween-20 deionized water up to 100 mL total volume
(b) pH adjust the solution to 4.5.

6. 0.1 M borate buffer, pH 8.5
To be used in the preparation of anti-DIG beads using EDC chemistry.

Materials:
Boric Acid
Deionized water

(a) Prepare 100 mL of buffer by mixing the following:
0.618 g boric acid
deionized water up to 100 mL total volume
(b) pH adjust the solution to 8.5 using NaOH.

7. 50 mM Sodium Acetate Buffer, pH 4.9
   To be used in all cellulase assays.

   Materials:
   Acetic acid
   Sodium acetate
   Deionized water

   (a) Prepare 100 mL of 1 M sodium acetate solution by mixing the following:
   2.533 mL (2.658 g) of acetic acid
   4.572 g of sodium acetate
   deionized water up to 100 mL total volume

   (b) In a 50 mL Falcon tube, dilute 2.5 mL of 1 M sodium acetate solution to a volume of 40 mL with deionized water.

   (c) Add small volumes of concentration KOH solution to adjust the pH to 4.9.

   (d) Add deionized water to a final volume of 50 mL.

8. Dinitrosalicylic acid (DNS) solution
   This is used in the filter paper assay to determine cellulase activty

   Materials:
   Dinitrosalicylic acid (DNS)
   NaOH
   Phenol
   Na-metabisulfite
   K-Na tartrate
   Deionized water

   (a) Dissolve the following into 2% (w/v) NaOH (2 g/100 mL):
   400 mg DNS (dinitrosalicylic acid)
   80 mg Phenol
   20 mg Na-metabisulfite
   8 g K-Na tartrate

   (b) Add deionized H_2O for a final volume of 40 mL.

9. Incomplete synthesis buffer (+ - -)
   To be used in BcsAB cellulose synthesis assays.
   Buffer should be mixed fresh daily.

Materials:
2x synthesis buffer (- - -)
$MgCl_2$
Deionized water

(a) Thoroughly mix the following (for 100 μL total volume):
50 μL 2x synthesis buffer (- - -)
5 μL $MgCl_2$ (400 mM)
45 μL deionized water

Note: 2x synthesis buffer (- - -) is composed of: 50 mM sodium phosphate (pH 7.5), 10 mM cellobiose, and 20% glycerol (provided by Prof. Jochen Zimmer at the University of Virginia).

10. Complete synthesis buffer (+++) with cellotetratose and BSA
To be used in BcsAB cellulose synthesis assays.
Buffer should be mixed fresh daily.

Materials:
2x synthesis buffer (- - -)
$MgCl_2$
c-di-GMP
UDP-glucose
Cellotetraose
BSA (bovine serum albumin)
Deionized water

(a) Thoroughly mix the following (for 100 μL total volume):
50 μL 2x synthesis buffer (- - -)
5 μL $MgCl_2$ (400 mM)
10 μL c-di-GMP (300 μM)
10 μL UDP-glucose (50 mM)
5 μL cellotetratose (100 mM)
10 μL BSA (5 mg mL^{-1})
15 μL deionized water

Note: 2x synthesis buffer (- - -) is composed of: 50 mM sodium phosphate (pH 7.5), 10 mM cellobiose, and 20% glycerol (provided by Prof. Jochen Zimmer at the University of Virginia).
Note: Complete synthesis buffer does not require cellotetraose or BSA. These are added to prevent the beads from sticking to each other and the surface during experiments.

11. Solution T
Used in TC and FC buffer preparation

Materials:
Tris-HCl
$CaCl_2$
Deionized water

(a) In a 50 mL Falcon tube add:
3.940 g Tris-HCl
0.147 g $CaCl_2$

(b) Add deionized water to 50 mL total volume and mix well.
Final concentration: 500 mM Tris-HCl and 20 mM $CaCl_2$

(c) Label the tube "Solution T" and store at 4°C.

12. TC Buffer
Used in the preparation of GAB buffer

Materials:
Solution T
Deionized water

(a) Add 40 mL of deionized water and 1.5 mL of Solution T to a 50 mL Falcon tube. Mix well.

(b) Adjust the pH to 8.0 by adding small volumes of concentrated KOH.
I usually add 4-5 pellets of KOH to a 50 mL Falcon tube, fill with deionized water, and use this to adjust the pH.

(c) Add water to a final volume of 50 mL and verify the pH. Adjust pH if necessary.

(d) Filter the buffer using 0.2 μm membrane filters.

(e) Label the tube as "TC" and store at 4°C.
Final concentration: 5 mM Tris-HCl (pH 8.0) and 0.2 mM $CaCl_2$.

13. FC Buffer
Used in the preparation of APB

Materials:
Solution T
KCl
$MgCl_2$

Deionized water

(a) Mix:
85 mL of deionized water
10 mL of Solution T
3.728 g KCl
0.0406 g $MgCl_2$

(b) Adjust the pH to 7.5 by adding small volumes of concentrated KOH.
I usually add 4-5 pellets of KOH to a 50 mL Falcon tube, fill with deionized water, and use this to adjust the pH.

(c) Add water to a final volume of 100 mL and verify the pH. Adjust pH if necessary.

(d) Filter the buffer using 0.2 μm membrane filters.

(e) Label the tube as "FC" and store at 4°C.
Final concentration: 50 mM Tris-HCl (pH 7.6), 500 mM KCl, 2 mM $MgCl_2$, and 2 mM $CaCl_2$.

14. 50 mM DTT solution
Used as a reducing agent to prevent oligomerization of actin monomers due to disulfide bonds

Materials:
DTT
TC Buffer
10 mM sodium acetate

(a) Dissolve 0.0771 g of DTT in 1 mL of 10 mM sodium acetate and mix well.

(b) Mix 1 mL of 0.5 M DTT with 9 mL of TC buffer for final concentration of 50 mM DTT.

(c) Distribute into aliquots of 10 μL (for GAB) and 40 μL (for APB).

(d) Flash freeze and store at -20°*C*.

15. GAB (General Actin Buffer) - a.k.a. G-buffer

Materials: TC buffer
ATP
DTT

(a) Mix:
485 μL of TC buffer
10 μL of 10 mM ATP
5 μL of 50 mM DTT
Final concentration: 5 mM Tris-HCl, 0.2 mM $CaCl_2$, 0.5 mM DTT, 0.2 mM ATP

(b) Label as "GAB" and store at 4°*C*.

16. APB (Actin Polymerization Buffer) - a.k.a. F-buffer

Materials:
FC buffer
ATP
DTT

(a) Mix:
455 μL of FC buffer
25 μL of 100 mM ATP
20 μL of 50 mM DTT
Final concentration: 50 mM Tris-HCl, 500 mM KCl, 2 mM $MgCl_2$, 2 mM $CaCl_2$, 2 mM DTT, 5 mM ATP.

(b) Label as "APB" and store at 4°*C*.

A.2 *Tr*Cel7A purification

This purification procedure was used to purify *Tr*Cel7A from a commercial cellulase mixture. The purified enzyme was used in the studies in Chapter 2.

Materials:
Trichoderma reesei cellulase mixture (Sigma)
10 mM TEA-HCl buffer
20 mM TEA-HCl buffer
20 mM TEA-HCl buffer with 0.1 M NaCl
20 mM TEA-HCl buffer with 0.33 M NaCl
50 mM Sodium acetate buffer (pH 4.9)
P-30 MBS columns
Q-trap ion chromatography column
NanoDrop
15 mL Falcon tubes
10 mL serological pipette
Vacuum line
Thin surgical tubing
SDS-PAGE materials (using precast 4-12% Bis-Tris gels)

1. Buffer exchange 450 μL of the commercial enzyme solution to 10 mM TEA-HCl buffer, pH 7.6 using P-30 MBS columns according to the manufacturer's instructions. *This can be accomplished by splitting the sample into six columns (75 μL each). The final volume will be approximately 670 μL.*

2. Determine the total protein concentration of buffer exchanged mixture using the "Protein" function on the Nanodrop. A molecular weight and extinction coefficient for the mixture can be estimated by calculating the weighted average of the main mixture components using their mass fractions (*Tr*Cel7A - 60% , *Tr*Cel6A - 20%, and endoglucanase II - 12%). The resulting molecular weight is 59,522 g mol^{-1} and the absorption coefficient is 81,565 M^{-1}cm^{-1}.

3. Keep a sample of enzyme mixture ($\sim$50 μL) from step one for later use on an SDS-PAGE gel.

4. Prepare a Q-trap ion chromatography column (all flow rates at $\sim$1 mL min^{-1}) using the experimental set up depicted in Figure A.1.

   (a) Create a flow through and collection set-up as shown in the figure.

   (b) Wash column with 5 column volumes (5 mL) of 20 mM TEA-HCl (no salt).

   (c) Wash column with 5 mL of 0.1 M NaCl in 20 mM TEA-HCl.

   (d) Wash column again with 5 mL of 20 mM TEA-HCl (no salt) to equilibrate.

5. Load the Q-trap column with 300 μL of enzyme mixture.

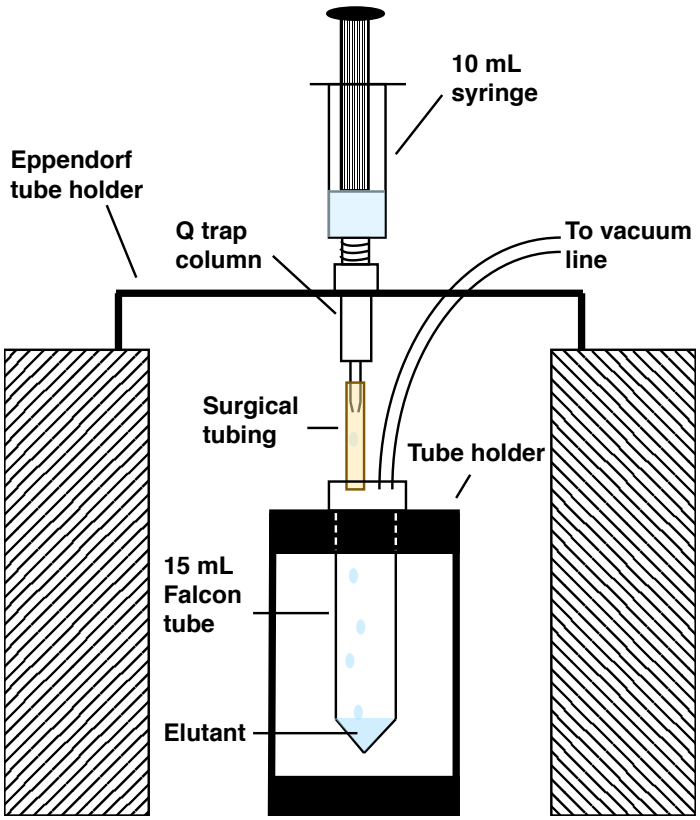

Figure A.1: **Experimental set-up for the purification of *Tr*Cel7A** from a commercial cellulase mixture using a Q-trap ion chromatography column.

6. Wash the column with 4 mL of 20 mM TEA-HCl (no salt).
7. Collect the sample (label it ”wash”) and replace the collection tube with a clean 15 mL Falcon tube.
8. Elute the unwanted enzymes with 2 mL of 0.1 M NaCl in 20 mM TEA-HCl.
9. Collect the sample (label it ”low salt elution”) and replace the collection tube with a new 15 mL Falcon tube.
10. Elute *Tr*Cel7A with 1.6 mL of 0.33 M NaCl in 20 mM TEA-HCl.
11. Collect the sample (label it ”high salt elution”).
12. Find the concentration of both the eluted protein mixture (low salt elution) and the purified *Tr*Cel7A (high salt elution) using the NanoDrop.
    Assume no *Tr*Cel7A is in the protein mixture elution and that the *Tr*Cel7A elution is pure when finding the concentration.
13. Perform SDS-PAGE on the sample from Step 3 and both elutant samples.

14. Buffer exchange the elutant samples into 50 mM sodium acetate buffer (pH 4.9) using P-30 MBS columns (Bio-Rad), according the the manufacturer instructions.

15. Aliquot and flash freeze the enzyme samples. Samples can be stored at -80°C for future use.

A.3 *Tr*Cel7A beads

Materials:
Sulfo-SMCC
P-30 MBS columns
PBS (pH 7.4)
Purified *Tr*Cel7A
dsDNA tether (biotin - 1010 bp - SH)
Streptavidin polystyrene beads (1.26 μm)
50 mM sodium acetate buffer (pH 4.9)
Polystyrene beads (0.75 μm)
BSA
Cup sonicator
Rotator
Microcentrifuge

1. Dissolve a 2mg no-weigh pack of sulfo-SMCC in 200 μL of deionized water. This will take a while.

2. Buffer exchange an aliquot of *Tr*Cel7A (20 μL) into PBS using a P-30 MBS column according to manufacturer's instructions. The resulting protein concentration, as measured by the NanoDrop, should be $\sim$0.45 mg mL^{-1}.

3. Mix 0.9 μL sulfo-SMCC solution with 35 μL of the buffer exchanged protein.

4. Incubate on a rotator at room temperature for 30 minutes.

5. Remove excess sulfo-SMCC by running the sample through another P-30 column (PBS) according to manufacturer's instructions.

6. Link the SMCC-protein complex to a 1010 bp DNA tether, functionalized with a biotin on one end and a thiol group at the other (biotin-1010 bp-SH), by mixing equal volumes of SMCC-protein and DNA. DNA should have an initial concentration of $\sim$115 ng μL^{-1}.

7. Incubate on a rotator at room temperature for 30 minutes.

8. During the incubation, dilute a sample of 1.26 μm streptavidin beads 1:20 in 50 mM sodium acetate buffer (pH 4.9). Sonicate the sample for 2 minutes in a cup sonicator at 40%.

9. Also during the incubation, dilute a sample of 0.75 μm non-functionalized polystyrene beads 1:100 in 50 mM sodium acetate buffer (pH 4.9). Sonicate the sample for 2 minutes in a cup sonicator at 40%. These will act as fiducial markers for drift correction during the experiment.

10. Mix the following:
    10 μL *Tr*Cel7a-DNA linker complex
    1 μL biotinylated BSA (5 mg mL^{-1} in 50 mM sodium acetate buffer)
    2 μL streptavidin beads (1.26 μm, 1:20 dilution)
    2 μL polystyrene beads (0.75 μm, 1:100 dilution)
    85 μL sodium acetate buffer (50 mM, pH 4.9)

11. Incubate the bead solution on a rotator for 45 minutes at 4°C.

12. Spin down the bead solution on a microcentrifuge at 10,000 rpm for 2 minutes. Remove half the buffer and replace with 50 μL of sodium acetate buffer (50 mM, pH 4.9) to remove unreacted components. Repeat this two times.

13. Sonicate the beads in a cup sonicator for 2 minutes at 20%.

A.4 **anti-DIG functionalized beads**

This protocol is slightly adapted from a protocol developed by Marie Eve Aubin-Tam, a former post-doctoral researcher in the lab.

Materials:
MES buffer
Borate buffer
PBS (pH 7.4)
Carboxy polystyrene beads (1.09 μm)
anti-Dig antibody
BSA
Ethanolamine
Cup sonicator
Rotator
Microcentrifuge

1. Make MES (0.1 M with 0.01% tween-20, pH 4.5), borate (0.1 M, pH 8.5), and PBS (pH 7.4) buffers according to the recipes in section A.1.
2. Mix 100 μL of 1 μm carboxy polystyrene beads with 100 μL of MES buffer.
3. Spin down (9000 rpm for 4 minutes) and resuspend in 200 μL MES buffer (repeat 5x).
4. Sonicate using a cup sonicator for 2 minutes at 40%.
5. Add 200 μL of freshly made EDC solution 2% w/v (corresponds to 10 mg EDC in 500 μL MES buffer).
6. Incubate the bead mixture for 3 hours at room temperature on a rotator.
7. Spin down (9000 rpm for 4 minutes) and resuspend the bead mixture in 1 mL of borate buffer.
8. Spin down (9000 rpm for 4 minutes) and resuspend the bead mixture in 400 μL of borate buffer.
9. Sonicate using a cup sonicator for 2 minutes at 40%.
10. Add 80 μL of 200 μg mL^{-1} anti-DIG and 24 μL of 5 mg mL^{-1} BSA in borate buffer (filtered).
11. Incubate the bead mixture on a rotator for 1 hour at room temperature and then overnight at 4°C.
12. Stop the reaction by adding 10 μL of 0.25 M ethanolamine (0.25 M solution of ethanolamine corresponds to 10 μL ethanolamine + 650 μL borate buffer).

13. Incubate and mix the bead mixture on at rotator for 30 minutes at 4°C.

14. Spin down the beads (9000 rpm for 4 minutes) and resuspend in 200 μL of 10 mg mL^{-1} BSA in PBS (filtered).
    Note: PBS is used here, NOT PBST as in Marie's protocol. The CBM assay does not work when PBST is used.

15. Sonicate the bead mixture in a cup sonicator for 1 minute at 25% with ice.

16. Store the beads at 4°C and rotating gently.

A.5 **Isolated CD beads**

Isolated CD was expressed in *E. coli* with a BCCP biotin tag and purified by Dr. Sreelatha Sarangapani.

Materials:
anti-Dig beads (1.09 μm)
dsDNA tether (Dig - 1010 bp - 1/2 anti-biotin)
PBS
50 mM sodium acetate buffer (pH 4.9)
Isolated CD - Provided by Dr. Sreelatha Sarangapani (SMART-MIT)
BSA
P-30 MBS column
Cup sonicator
Microcentrifuge
Rotator

1. Dilute 3 μL anti-Dig beads (1.09 μm) in 57 μL PBS.

2. Dilute a samples of 1010 bp DNA, functionalized with Dig at one end and 1/2 anti-biotin at the other ($\sim$30 ng μL^{-1}). Serially dilute 3 μL into 100 μL PBS three times. After the third dilution, dilute the sample one more time at a 1:100 dilution.
   Note: 1/2 anti-biotin was prepared by Yinnian Feng as described in Das *et al.* PNAS, **112**(5), 2014.

3. Buffer exchange a CD sample into PBS using a P-30 MBS column according to manufacturer's instructions.
   Note that isolated CD aliquots are 10 μL at a concentration of ***CHECK THIS...0.5 mg/mL****. To buffer exchange, this aliquot must first be diluted 1:2 in sodium acetate buffer (50 mM, pH 4.9) in order to reach the minimum volume requirement of 15 μL for the column.*

4. Mix the bead solution:
   2 μL diluted Dig-1010 bp-1/2 anti-biotin
   7 μL isolated CD in PBS
   10 μL diluted anti-Dig beads (1μm)
   1 μL BSA in PBS (10 mg mL^{-1})
   60 μL PBS buffer

5. Incubate the beads on a rotator for at least 45 minutes on the rotator at 4°C.

6. Pellet the beads by spinning down in the bench top centrifuge for 4 minutes at 8000 rpm and resuspend the pellet in acetate buffer (50 mM, pH 4.9). Repeat this three times.

7. Sonicate the buffer exchanged bead solution in a cup sonicator for 2 minutes at 20%.

A.6 **CBM beads - Chapter 2**

Materials:
anti-Dig beads (1.09 μm)
dsDNA tether (Dig - 1010 bp - anti-His)
Isolated CBM - Provided by Dr. Sreelatha Sarangapani (SMART-MIT)
PBS (pH 7.4)
50 mM acetate buffer
BSA
P-6 MBS columns
Cup sonicator
Microcentrifuge
Rotator

1. Dilute 3 μL anti-Dig beads (1.09 μm) in 57 μL PBS.

2. Dilute a samples of 1010 bp DNA, functionalized with Dig at one end and anti-HIS at the other ($\sim$30 ng μL^{-1}). Serially dilute 3 μL into 100 μL PBS three times. After the third dilution, dilute the sample one more time at a 1:100 dilution.

3. Buffer exchange a CBM sample into PBS using a P-6 MBS column according to manufacturer's instructions.
   Note that CBM aliquots are 10 μL at a concentration of 0.6 mg mL^{-1}. To buffer exchange, this aliquot must first be diluted 1:2 in sodium acetate buffer (50 mM, pH 4.9) in order to reach the minimum volume requirement for the column.

4. Mix the bead solution (80 μL total):
   0.5 μL diluted DIG-1010 DNA-antiHIS
   5 μL CBM in PBS
   10 μL diluted anti-Dig beads (1μm)
   1 μL BSA in PBS (10 mg mL^{-1})
   63.5 μL PBS buffer

5. Incubate the beads on a rotator for at least 45 minutes on the rotator at 4°C.

6. Pellet the beads by spinning down in the bench top centrifuge for 4 minutes at 8000 rpm and resuspend the pellet in acetate buffer (50 mM, pH 4.9). Repeat this three times.

7. Sonicate the buffer exchanged bead solution in a cup sonicator for 2 minutes at 20%.

A.7 **CBM beads - Chapter 3**

Materials:
Streptavidin beads (1.09 μm)
dsDNA (biotin - 1010 bp - anti-His)
BSA
PBS (pH 7.4)
Isolated CBM1 - Provided by Prof. Shishir Chundawat (Rutgers)
50 mM acetate buffer
P-6 MBS column
Rotator
Microcentrifuge
Cup sonicator

1. Mix bead solution below (total = 80 μL)
   0.5 μL DNA (biotin - 1010 bp - antiHIS)
   10 μL Streptavidin bead (1 μm, diluted 1:50 in PBS)
   4 μL CBM1 (diluted 1:100 in PBS, $\sim$200 nM)
   0.5 μL BSA in PBS (10 mg mL^{-1})
   65 μL PBS (pH 7.4)

   *Notes:

   (a) DNA stock is at $\sim$30 ng μL^{-1} and is serially diluted 3:60, followed by 3 x 3:100 in PBS prior to this step.

   (b) CBM1 must be buffer exchanged into PBS from stock using P-6 MBS columns (Biorad). To do this, dilute the stock to 20 μL (1:2 dilution) with acetate buffer (50 mM, pH 4.9), then run the sample through the column according to manufacturer instructions.

2. Incubate solution for at least 45 minutes on the rotator at 4°C.

3. Pellet the beads by spinning down in the bench top centrifuge for 3.5 minutes at 9250 rpm and resuspend the pellet in acetate buffer (50 mM, pH 4.9). Repeat this two times.

4. Sonicate the buffer exchanged bead solution in a cup sonicator for 2 minutes at 20%.

A.8 **Filter paper cellulose solution**

Materials:
Whatman grade 1 filter paper
Deionized water
50 mM acetate buffer (pH 4.9)
Tissue homogenizer
1 mL micropipette
Cup sonicator
Vortex
16 gauge syringe

1. Cut approximately 20-25 mg of Whatman Grade 1 filter paper (99% cellulose) into small pieces.
2. Place pieces into a tissue homogenizer, add a few drops of deionized water and use the homogenizers to mechanically break apart the filter paper for 5 minutes.
3. Scoop the resulting mixture into a 15 mL Falcon tube and add 10 mL of 50 mM sodium acetate buffer (pH 4.9).
4. Pull apart and mix the cellulose by pulling the filter paper in and out of a 10 mL serological pipette or a 1 mL micropipette with the very end cut off of the pipette tip.
5. Sonicate the mixture in a cup sonicator for 2.5 minutes at 40%.
6. Vortex the solution for 10-20 seconds on high.
7. Mix again as in Step 4.
8. Repeat steps 5-7 three times (or more as necessary).
9. Pull a 1 mL sample from the larger stock and place in an Eppendorf tube. Mix the solution thoroughly by pulling the solution in and out of a 16 gauge needle.
10. Dilute a portion of this sample 50 times in 50 mM sodium acetate buffer in a new Eppendorf tube.
11. Sonicate the diluted sample for 2.5 minutes at 40%.
12. Store the samples at 4°C.
13. Steps 5-7 will need to be repeated each day before loading a slide.

A.9 *Cladophora* cellulose solution

Materials:
Cellulose samples (*Cladophora* I or III) - Provided by Prof. Shishir Chundawat (Rutgers)
Deionized water
Cup sonicator
Vortex
16 gauge syringe

1. Weight out a 1 mg sample of the desired cellulose sample and add it to 1 mL of deionized water.
2. Sonicate the mixture for 2 minutes at 50% in a cup sonicator.
3. Vortex the solution for 15 seconds on high.
4. Pull the solution up and down using a 16-gauge syringe for 1-2 minutes.
5. Vortex the solution again for 15 seconds.
6. Repeat steps 2-5 three times.
7. Dilute the mixture 1:2 by mixing 500 μL of the prepared mixture with 500 μL deionized water.
8. Store this solution at 4°C.

   When preparing to load a slide, a small sample ($\sim$100 μL) of the stored cellulose solution is separated from the stock and the cellulose is pulled apart by sonicating for 2 minutes at 50% in a cup sonicator and vortexed for 15 seconds. This solution is then loaded onto the slide.

A.10 **Cellulose slides**

Materials:
Standard microscope slide
KOH etched coverslip
Double sided tape
BSA
50 mM acetate buffer

1. Create a flow cell using and KOH etched coverslip and double sided tape.
2. Add 20 μL of the appropriate cellulose solution to the flow cell.
3. Allow the cellulose to become non-specifically immobilized on the surface by drying out the slide in the oven for approximately 1 hour (or until the full length of the flow cell is dry) at $\sim$95°C.
4. Once dry, block the surface from non-specific binding by adding 20 μL of 10 mg mL^{-1} BSA in acetate buffer (50 mM, pH 4.9). Incubate for 10 minutes.
5. Flow in 20 μL of the appropriate enzyme functionalized bead solution.

A.11 **DNS activity assay**

The following assay is designed for a 7.5 μL reaction volume.

Materials:
1 mg mL^{-1} enzyme sample
50 mM sodium acetate buffer (pH 4.9)
Cellobiose
DNS solution
Whatman grade 1 filter paper
Standard hole punch
Scissors
200 μL PCR tubes
Oven ($\sim$100°C)
NanoDrop

1. Create a filter paper (Whatman Grade 1) disk using an office hole punch.
2. Cut the disk into 16ths.
3. Place one piece of filter paper disk into a 200 μL PCR tube and add 7.5 μL of the desired enzymes ($\sim$1 mg mL^{-1} concentration). The enzyme should be in 50 mM sodium acetate buffer, pH 4.8. (Alternatively, add 7.5 μL of cellobiose control solution for use in generating a calibration curve.
4. Incubate the celluose/enzyme mixture at room temperature for 50 hours.
5. Add 15 μL DNS (dinitrosalicylic acid) solution (see recipe in the buffer section).
6. Incubate the sample for 25 minutes in the oven at $\sim 100°C$.
7. Remove the sample(s) from the oven and allow them to cool to room temperature. Note: This step is important as the color of the solution will continue to change until it has cooled.
8. Measure the reducing sugar concentration using the NanoDrop (UV-VIS) at 540 nm. Repeat for all samples and cellobiose controls.

Standards and controls:

- Use 0 - 4 mg mL^{-1} cellobiose standards in acetate buffer without filter paper to generate a calibration curve with samples at 0, 1.0, 2.0, 3.0, and 4.0 mg mL^{-1}.
- Include another standard that only contains the filter paper sample and acetate buffer (no cellobiose or enzyme).

A.12 **BcsAB slide preparation**

This protocol can be used for any of the BcsAB constructs. Any differences between constructs are indicated in the appropriate steps.

Materials:
KOH etched coverslip
Cy3 labelled streptavidin
Polystyrene beads (0.75 μm)
PBS (pH 7.4)
Biotinylated anti-His
BSA
Blotting-grade blocker (casein)
20 mM Tris-HCl (pH 7)
BcsAB enzyme sample (nanodisk or amphipol)
Cellulose DNA aptamer
Streptavidin beads (1.09 μm)
Incomplete synthesis buffer (+ - -)
Complete synthesis buffer (+++) with BSA and cellotetraose

1. Create a flow cell using a KOH etched slide and double sided sticky tape.
2. Load the slide with 20 μL of a Cy3-streptavidin and polystyrene bead (0.75 μm) solution in which both components have a final dilution of 1:2000 in PBS (pH 7.4). Incubate the slide in a humidity chamber at room temperature for 15 minutes.
   Cy3-streptavidin was only used over unlabeled streptavidin as it was used during assay development to get a visual sense of surface coverage.
3. Wash the slide with 100 μL of 1 mg mL^{-1} casein (blotting-grade blocker) in PBS. Incubate the slide in a humidity chamber at room temperature for 15 minutes.
4. Add 20 μL biotinylated anti-HIS diluted 1:100 from stock in PBS. Incubate the slide in a humidity chamber at room temperature for 15 minutes.
5. Wash the slide with 100 μL of 5 mg mL^{-1} BSA in Tris-HCl (20 mM, pH 7).
6. Add 20 μL of the appropriate BcsAB construct* (diluted into Tri-HCl) to the slide. Incubate the slide in a humidity chamber at room temperature for 20 minutes.
   **The BcsAB-nanodisc construct is diluted 1:50,000 in Tris-HCl from 3 μM stock, while the BcsAB-amphipol construct is diluted 1:2000 in Tris-HCl from 8 μM stock and the S678-amphipol construct is diluted 1:1500 in Tris-HCl from 6 μM stock.*
7. Wash the slide with 100 μL of 5 mg mL^{-1} BSA in Tris-HCl (20 mM, pH 7).
8. Add 20 μL of DNA cellulose aptamer beads (1.09 μm) in incomplete (+ - -) synthesis buffer with 0.1 mg mL^{-1} BSA to the flow cell. Incubate the slide in a humidity chamber at room temperature for 20 minutes.

(a) *DNA cellulose aptamer beads*

i. Mix the following:
50 μL biotinylated cellulose specific DNA aptamer (3.1 nmol μL^{-1}) in deionized water
50 μL Streptavidin beads (1.09 μm), diluted 1:50 in 20 mM Tris-HCl (pH 7)

ii. Incubate the bead solution on a rotator at room temperatures for 45 minutes.

iii. Pellet the beads to remove unreacted cellulose aptamer by spinning down the sample using a bench top centrifuge for 3.5 minutes at 9250 rpm and resuspend the pellet in incomplete synthesis buffer (+ - -). Repeat this two times. Add BSA to the solution during the final resuspension such that the final BSA concentration is 0.1 mg mL^{-1}.

iv. Sonicate the buffer exchanged bead solution in a cup sonicator for 2 minutes at 20% before use.

9. Wash out untethered beads and initiate synthesis by adding 50 μL of complete synthesis buffer (+++) with 0.5 mg mL^{-1} BSA and 5 mM cellotetraose (Note: BSA and cellotetraose are already included in the buffer recipe for "complete synthesis buffer with BSA and cellotetraose").

A.13 **Plectin-ABD beads**

Materials:
Biotin-maleimide
Glutathione
DMSO
Deionized water
1.09 μm streptavidin beads
Biotinylated BSA
PBS (pH 7.4)
Nucleus wash buffer - Provided by Daniel Balikov
Plectin-ABD - Provided by Prof. Arnoud Sonneberg via Daniel Balikov
Rotator
Microcentrifuge
Cup sonicator

1. Mix biotinylated maleimide and glutathione. Incubate overnight on a rotator at 4°C.
   4 μL b-maleimide (5 mg mL^{-1} in DMSO)
   50 μL glutathione (10 mg mL^{-1} in DI H_2O)

2. Mix and incubate the following bead solution for one hour on a rotator at room temperature to create glutathione coated beads.
   10 μL streptavidin beads (1.09 μm, diluted 1:20 in PBS, pH 7.4)
   30 μL biotin-maleimide/glutathione mixture (from step 1)
   2 μL biotinylated BSA (b-BSA, 5 mg mL^{-1})
   58 μL PBS (pH 7.4)

3. Spin down bead solution for 3.5 minutes at 9250 rpm on the microcentrifuge and resuspend the beads in nucleus wash buffer. Repeat this two times.
   Note: Nucleus wash buffer is composed of 0.2 M sucrose, 10 mM HEPES, 1 mM $MgCl_2$.

4. Sonicate the bead solution for 2 minutes at 20% in a cup sonicator.

5. Mix the bead solution with plectin-ABD in a 1:1 ratio as indicated below
   50 μL plectin (1:1 million dilution in nucleus wash buffer)
   50 μL glutathione bead solution
   1 μL ATP (100mM)

6. Incubate the plectin-ABD bead solution on a rotator for 2 hours at room temperature.

Note: Glutathione beads can be stored for up to a month at 4°C, however, plectin-ABD beads do not keep well and should be used the same day.

A.14 **Biotinylated actin filaments**

This protocol is modified from that found in the dissertation of Hyungsuk Lee titled "Mehcanical Properties of F-actin Network" (MIT, 2009).

Materials:
Actin
Biotinylated actin
GAB buffer
APB buffer
Phalloidin
Deionized water
Ice

1. Reconstitute actin by adding 100 μL of dionized water to 1 mg vial of lyophilized actin. Mix well by pipetting up and down. Aliquot into 5 μL vials. Keep the vials to be used and snap freeze the rest.
   The solution will have a concentration of actin of 10 mg mL^{-1} (232 μM), 5 mM Tris-HCl (pH 8.0), 0.2 mM NaATP, 0.2 mM $CaCl_2$, 5% sucrose, and 1% dextran.

2. Reconstitute biotinylated actin by adding 20 μL of dionized water. Aliquot into 5 μL vials. Keep the vials to be used and flash freeze the rest.
   The final concentration is 1 mg mL^{-1} of biotinylated actin.

3. Thaw one vial of 10 mg mL^{-1} pure actin and 1 vial of 1.0 mg mL^{-1} biotinylated actin.

4. Prepare fresh GAP buffer (Appendix B.1)

5. Mix the two vials and label the mixture "A+BA."
   The ratio is 10:1 (actin:biotin-actin) with a total actin concentration of 5.5 mg mL^{-1} (127.6 μM).

6. Add 100 μL GAB and mix well by gently pipetting up and down. Place on ice for 1 hour.
   The solution is 110 μL with a concentration of actin of 0.5 mg mL^{-1} (11.6 μM).

7. Prepare fresh APB. (Appendix B.1)

8. Polymerize actin by adding 11 μL of APB to the actin solution. Mix well by pipetting up and down in a gentle fashion. Place on ice for 20 minutes.
   The actin concentration is now 0.435 mg mL^{-1} (10 μM).

9. Add 5 μL phalloidin (stabilizes the actin filaments). Leave on ice in the dark for 1 hour. F-actin is stable in the dark for at least one week at 4°C.

Note: If further dilution of actin is required, mix 5 μL of polymerized actin (10 μM) with 495 μL of GAB/APB solution (10GAB:1APB). The final actin concentration will then be 4.35 μg mL^{-1} (0.1 μM).

A.15 **Actin functionalized beads**

This protocol utilizes the biotinylated F-actin from the previous protocol.

Materials:
ATP
Nucleus wash buffer - Provided by Daniel Balikov
Streptavidin beads (1.09 μm)
biontinylated F actin
GAB buffer
APB buffer
Microcentrifuge
Cup sonicator
Rotator

1. Dilute 5 μL of stock 1.09 μm streptavidin beads into 95 μL nucleus wash buffer. Then spin down the sample in a microcentrifuge (3.5 min at 9250 rpm), remove the supernatant and resuspend the beads in 100 μL of nucleus wash buffer. Repeat this three times.

2. Sonicate the diluted bead solution for 2 minutes at 40%

3. Create the F-actin functionalized beads by mixing the following (total volume: 60 μL):
   8 μL diluted streptavidin beads (1.09 μm, 1:20 dilution)
   5 μL biotinylated F-actin (previously diluted 1:10,000 in GAB/APB (10:1) buffer
   0.6 μL 100 mM ATP in TC buffer
   45 μL nucleus wash buffer

   Note: Nucleus wash buffer is composed of 0.2 M sucrose, 10 mM HEPES, 1 mM $MgCl_2$.

4. Incubate the beads on a rotator at 4°C for 30 minutes in the dark.

Note: For best results, beads should be freshly functionalized each day.

A.16 **Nucleus slide preparation**

Materials:
KOH etched coverslip
Standard microscope slide
Poly-L-lysine
Ethanol (200 proof)
Double sided tape
Isolated nuclei - Prepared and provided by Daniel Balikov
BSA
Nucleus wash buffer - Provided by Daniel Balikov
Actin or Plectin-ABD beads
Nail polish

1. Create a 10-15 μL flow cell using a KOH etched coverslips coated in poly-L-lysine, standard microscope slides, and double-sided sticky tape.
   Coverslips are coated with poly-L-lysine by covering the coverslip with $\sim$200 μL of 3% poly-L-lysine in ethanol and then evaporating the ethanol by placing the slide in the oven at $\sim$95°C for approximately 10 minutes. The coated side must face the slide when assembling the flow cell.

2. Add 20 μL of nuclei sample to the flow cell and incubate the slide in a humidity chamber for 30 minutes at room temperature to allow for the nuclei to become immobilized on the coverslip surface.

3. Block the surface by adding 20 μL of 10 mg mL^{-1} BSA in nucleus wash buffer. Incubate in a humidity chamber for 10 minutes at room temperature.
   Nucleus wash buffer is composed of 0.2 M sucrose, 10 mM HEPES, and 1 mM $MgCl_2$.

4. Apply 20 μL of the appropriate bead solution (actin or plectin-ABD) to the flow cell.

5. Seal the slide with nail polish and load the slide on the microscope.